Experimental study on dynamic divergence instability and chaos of clamped-clamped circular cylindrical shells conveying airflow

Iman Gholami

Master of Engineering

Department of Mechanical Engineering

McGill University

Montreal, Québec, Canada

October 2021

A thesis submitted to McGill University in partial fulfillment of the requirements of the degree of Master of Engineering

Abstract

Experiments have shown that soft circular cylindrical shells supported at both ends and conveying airflow lose stability by so-called *dynamic divergence*. Dynamic divergence is an instability phenomenon starting as a divergence, with amplitude comparable to the shell radius, that largely constrains the flow. This results in pressure building up and reopening the shell, triggering a dynamic instability. The characteristics of dynamic divergence instability are studied in-depth for the first time to elucidate the nature and characteristics of this phenomenon. Experiments have been conducted on elastomer (silicone rubber) thin circular cylindrical shells clamped at both ends and subjected to internal airflow. Bifurcation diagrams have been obtained by varying the flow velocity as the control parameter, exhibiting strong subcritical behaviour and large hysteresis in the flow velocity for the onset and cessation of dynamic instability. The effect of flow velocity and geometric parameters of the shell, namely length-to-radius (*L/R*) and thickness-to-radius (*h/R*) ratios, is investigated experimentally on the onset of instability and post-critical behavior; (i) thinner and longer shells lose stability at lower flow velocities, (ii) thinner shells have higher rms vibration velocity, (iii) by decreasing *L/R*, the subcritical behaviour is weakened for thin shells, while it is strengthened for thick shells. The possible existence of a chaotic component in the dynamic response following the initial divergence was firstly discerned by looking at high-resolution photos taken with a high-speed camera. Several qualitative and quantitative measures and criteria for chaos, such as phase plane plots, Poincaré maps, power spectra (PSD), the largest Lyapunov exponent, autocorrelation, and probability density function (PDF), have been used to confirm the existence of chaos in the oscillations, and to examine the effect of *L/R* and *h/R* ratios on chaotic behaviour of the system; (i) thinner and shorter (with some exceptions) shells generally exhibit more pronounced chaotic behavior, (ii) thin shells generally display more complex nonlinear dynamics at the upper half of the flow velocity range, while thick shells do the opposite. Finally, the effect of confinement (by a coaxial rigid outer tube) on the onset and post-critical behaviour of the system is explored; the unconfined configuration is shown to have (i) considerably higher critical and restabilization flow velocities, (ii) higher rms velocity of motion, and (iii) slightly stronger subcritical behaviour.

Résumé

Des expériences ont montré que les coques cylindriques circulaires souples supportées aux deux extrémités et parcourues d'air perdent leur stabilité par ce que l'on appelle la divergence dynamique. La divergence dynamique est un phénomène d'instabilité commençant par une divergence, d'amplitude comparable au rayon de la coque, qui contraint fortement l'écoulement. Il en résulte une accumulation de pression et une réouverture de la coque, déclenchant une instabilité dynamique. Les caractéristiques de l'instabilité de divergence dynamique sont étudiées en profondeur pour la première fois pour élucider la nature et les caractéristiques de ce phénomène. Des expériences ont été menées sur des coques cylindriques circulaires minces en élastomère (caoutchouc de silicone) encastrées aux deux extrémités et soumises à un flux d'air interne. Les diagrammes de bifurcation ont été obtenus en faisant varier la vitesse d'écoulement comme paramètre de contrôle, présentant un fort comportement sous-critique et une grande hystérésis dans la vitesse d'écoulement au déclenchement et à la cessation de l'instabilité dynamique. L'influence de la vitesse d'écoulement et des paramètres géométriques de la coque, à savoir les ratios longueur/rayon (L/R) et épaisseur/rayon (h/R), sur l'apparition de l'instabilité et le comportement post-critique est étudiée expérimentalement; (i) les coques plus minces et plus longues perdent leur stabilité à des vitesses d'écoulement plus faibles, (ii) les coques plus minces ont de vitesses de vibration plus élevées, (iii) en diminuant L/R, le comportement sous-critique est affaibli pour les coques minces, alors qu'il est renforcé pour les coques épaisses. L'existence possible d'une composante chaotique dans la réponse dynamique suite à la divergence initiale a d'abord été discernée en examinant de photos d'haute résolution prises avec une caméra à grande vitesse. Plusieurs mesures et critères qualitatifs et quantitatifs du chaos, tels que les portraits de phase, les sections de Poincaré, les spectres de puissance (DSP), le plus grand exposant de Lyapunov, l'autocorrélation et la densité de probabilité, ont été utilisés pour confirmer l'existence du chaos dans les oscillations et pour examiner l'effet des ratios L/R et h/R sur le comportement chaotique du système ; (i) les coques plus minces et plus courtes (à quelques exceptions près) présentent généralement un comportement chaotique plus prononcé, (ii) les coques minces affichent généralement une dynamique non linéaire plus complexe dans la moitié supérieure de la plage de vitesse d'écoulement, tandis que les coques épaisses montrent le contraire. Enfin, l'effet du confinement (dû au tube externe coaxial rigide) sur l'apparition et le comportement post-critique du système a été exploré ; il est démontré que la configuration non confinée a (i) des vitesses d'écoulement critiques et de stabilisation considérablement plus élevées, (ii) de vitesses de vibration plus élevées et (iii) un comportement sous-critique légèrement plus marqué.

Acknowledgments

First and foremost, I would like to express my sincere gratitude and appreciation to Professor Michael P. Païdoussis and Professor Marco Amabili for supervising this research work. I am very grateful to Prof. Païdoussis for accepting me as an M.Eng student in the first place. It is a great honour for me to learn Fluid-Structure Interactions from such a distinguished scientist and professional teacher. I thank him for his tremendous kindness, assiduous help, and continuous support. I am also thankful to Prof. Marco Amabili for his helpful discussions, insightful comments, and invaluable feedbacks. I want to thank Mary Fiorilli for her kind assistance with all administrative matters. Also, I would like to acknowledge the financial support from the Natural Sciences and Engineering Research Council of Canada (NSERC) for Discovery and NSERC RTI grants and Pipeline Research Council International, Canada (PRCI). I was extremely lucky to be surrounded by wonderful friends and lab-mates during my study; I must thank Giovanni Ferrari for all the time we spent, conclusions we drew, and future plans we made together. Also, I must thank Giulio Franchini, Francesco Giovanniello and Stanislas Le Guisquet for all the interesting discussions and brilliant thoughts. I am grateful to Professor Evgeny Timofeev for his insights into the fluid dynamics aspect of the problem at hand, and Professor Farhang Daneshmand for sharing useful comments regarding computational analysis of flow-induced vibrations. 1 would like to extend my appreciation to Professor Jovan Nedić for lending us the high-speed camera. I am deeply indebted to Mahdi Chehreghani, my groupmate in the fluid-structure interaction research group, whose scientific intuition has always been a source of inspiration for me. I am also thankful to all my friends and colleagues in the office and the department, especially Alireza Mirmohammadi, Aram Bahmani, Ali Shafie, Mohammad Faisal Butt and Ahmed Saleh Dalaq.

I would like to extend my deepest gratitude to my family in Iran, for their support and encouragement. I am grateful to my beloved mother, father and sister for their faith in me. Words cannot describe my gratitude to my wonderful wife, Sahar, for her loving support. I would like to express my heartfelt thanks to her for standing beside me in all ups and downs. Sahar, I owe you everything.

List of publications by the author

- Gholami, I., Amabili, M., Païdoussis, M.P.: Dynamic divergence of circular cylindrical shells conveying airflow. Mech. Syst. Signal Process. Accepted (September 2021).
- Gholami, I., Amabili, M., Païdoussis, M.P.: Experimental parametric study on dynamic divergence instability and chaos of circular cylindrical shells conveying airflow. Mech. Syst. Signal Process. Submitted (September 2021).

Table of contents

List of tables

List of figures

Nomenclature

A^*	Chocked throat area of the shell
A_t	Throat area of the shell at the buckled cross-section
A_u	Internal area of the shell at the lower clamp
c	Speed of sound in air
D_h	Diameter of the shell
d	Delay
E	Young's modulus
F_b	Buoyancy force
g	Gravitational constant
h	Thickness of the shell
L	Length of the shell
m	Longitudinal wave number
$\dot{m}$	Mass flow rate
M_t	Mach number at the throat of the shell
M_u	Mach number at the lower clamp
n	Circumferential wave number
P_0	Tank pressure
P_1	Line pressure before the valves
P_2	Line pressure after the valves
P_{ann}	Pressure in the annulus
P_u	Air pressure at the lower clamp
ρ_s	Mass density of silastic
ρ_u	Mass density of air
ρ_w	Mass density of water
R	Internal radius of the shell
Re	Reynolds number
SG	Specific gravity with respect to water
t	Time
T	Air temperature
V	Flow velocity
V_{cr}	Critical flow velocity
V_{rest}	Restabilization flow velocity
V_s	Volume of displaced water
ν	Poisson's ratio
W_s	Weight of silastic specimen
γ	Heat capacity ratio of dry air
λ_1	The largest Lyapunov exponent

1 Introduction

1.1 General remarks

Flow-induced vibration (FIV) problems are classified in several ways. Some classifications are phenomenological such as the one proposed by Blevins [1], according to which, vibrations induced by steady flows and unsteady flows are distinguished from each other. The former are then subdivided into 'self-excited vibrations' (referred to as *instabilities*) and 'vortex-induced vibrations', while the latter are subdivided into random (e.g. turbulence-related), sinusoidal (e.g. wave-related), and transient oscillations (e.g. water-hammer problems).

Weaver [2] classified flow-induced vibrations based on the nature of the vibration in each case, as follows: (a) forced vibrations induced by turbulence; (b) self-controlled vibrations, in which flow has some periodicity, independent of structure motion; (c) self-excited vibrations.

A very systematic classification, however, was introduced by Naudascher and Rockwell [3,4], in which the source of excitation is considered in the categorization; (i) extraneously-induced excitation (EIE), (ii) instability-induced excitation (IIE), and (iii) movement-induced excitation (MIE), also known as self-excited oscillations. Self-excited oscillations are oscillatory motions due to the movement of the structure, i.e., no external excitation exists in the absence of motion; the problem at hand belongs to this class of FIV. Self-excited oscillations often involve large deformations; hence, strong nonlinearities can come into play [5,6].

Many biological and engineering systems involve thin-walled cylindrical shells in contact with fluid; the shells may have various geometries (e.g., cylindrical or conical, open or closed), boundary conditions (e.g., clamped-clamped, simply-supported, cantilevered, mismatched (asymmetric)) and materials (aluminium, elastomer (silicone rubber), Polyethylene Terephthalate (PET) or living tissue), while the fluid may be compressible or incompressible, stagnant or flowing, internal or external. Urinary tracts, pulmonary passages and veins and are examples of shells in contact with flowing fluid in physiological systems; heat exchangers, jet pumps, thermal shields in nuclear reactors and heat shields in aircraft engines are examples of engineering applications of such systems (see Figure 1-1).

Thin shells conveying fluid are subject to three types of instabilities, namely, buckling (static divergence), flutter and dynamic divergence (oscillatory instabilities); although all three types are undesirable, oscillatory instabilities can result in catastrophic structural failure due to fatigue. Dynamic divergence should not be misinterpreted as flutter, which typically displays a specific oscillation frequency at its onset.

Most of the studies on the stability of cylindrical shells deal with external compressible and particularly supersonic flows, in which the structure loses stability by flutter. This indicates the enormous interest on the effects of high-speed flow on the outer-skin panels of aerospace vehicles such as aircraft and missiles [7,8].

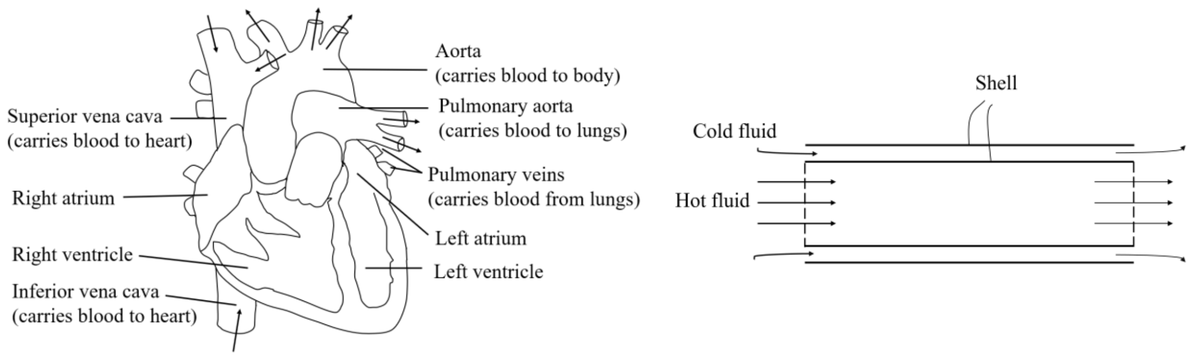

(a) (b)

Figure 1-1. Cylindrical shells in contact with flowing fluid; (a) blood vessels of a human heart as physiological systems; (b) heat shield as an engineering application.

1.2 Literature review

The loss of stability of circular cylindrical shells and pipes supported at both ends is theoretically predicted to be via static divergence, while cantilever shells and pipes generally become unstable by flutter. For a long time, the dynamics of shells subjected to incompressible (subsonic) axial flow seemed uninteresting since they were thought to become unstable only by mild (small-amplitude) divergence. However, some experiments presented in [9,10] breathed new life to the subject by showing that, not only thin cantilevered, but also clamped-clamped shells containing subsonic axial flow *do flutter*. The first linear analytical model for clamped-clamped and cantilevered circular cylindrical shells containing inviscid incompressible flow was presented in [10]. Flügge's shell theory was used for the equation of motion of the shell and the flow field was described by potential flow theory. Travelling wave solutions were assumed for the shell displacement components. The theory predicted that the system loses stability by single-mode flutter for the cantilevered shell, while by divergence and subsequently Païdoussis-type [11] coupled-mode flutter for the clamped-clamped shell. In the experiments, however, flutter was observed directly for clamped-clamped shells; this was at first presumed to be flutter entrained by divergence, but dynamic divergence was another hypothesis suggested later in [12]. In the experiments with clamped-clamped elastomer shells [10], a shell-type flutter in the second circumferential mode (n=2, where n is the circumferential wave number) was observed. In experiments with short cantilevered shells, only shell-mode oscillations with n=2 or 3 were observed, while being stable in beam-mode flexure. Weaver and Unny [13] presented a linear theoretical model for simply-supported circular cylindrical shells and obtained similar results as for clamped-clamped shells. The shell was predicted to lose stability by static divergence at first, and then by flutter at higher flow velocities.

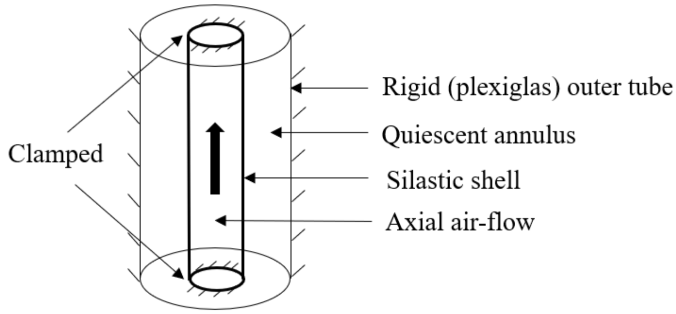

Figure 1-2. Schematic of the clamped-clamped shell subjected to internal airflow.

The theoretical study of the dynamics and stability of clamped-clamped coaxial circular cylindrical shells subjected to internal and/or annular incompressible or compressible flow was extended by Païdoussis et al. [14]. It was found that a shell in annular flow loses stability at a lower flow velocity in comparison with a shell containing internal flow. They also concluded that the critical flow velocity is lower when both shells are flexible. In addition, according to linear theory, the compressibility of the fluid was shown to have little effect on the stability of the system. El Chebair et al. [15] conducted some experiments on clamped-clamped and cantilevered shells subjected to annular flow. They observed that the system loses stability by flutter for a cantilevered shell and by divergence (not followed by flutter) in the case of a clamped-clamped shell.

All of the aforementioned theoretical studies were based on linear models, which are only capable of predicting the first instability encountered by the system with increasing flow velocity, but not the post-instability static or dynamic behaviour. The reason is that geometrical nonlinearities associated with deformation amplitudes of the order of shell thickness start playing an important role in the dynamical behaviour of the system, thus necessitating the use of nonlinear theories. Most of the nonlinear work has been motivated by aerospace applications and hence is associated with supersonic external flow. For an excellent review of nonlinear vibrations of circular cylindrical shells, refer to the work of Amabili and associates [16,17,18,19,20,21,22]. Nonlinear dynamics and stability of simply-supported circular cylindrical shells containing inviscid incompressible fluid flow was revisited in [23] by means of Donnell's nonlinear shallow-shell theory and linearized potential flow theory. A seven degree-of-freedom solution allowing for travelling wave response of the shell and shell axisymmetric contraction (responsible for the softening nonlinear behaviour of the shell) was utilized. The results demonstrated that the system loses stability by strongly subcritical divergence.

A refined model for the subcritical static divergence of circular cylindrical shells conveying incompressible fluid, taking into account also geometric imperfections, was introduced by Amabili et al. [24]. Numerical results for thin aluminium shells conveying water were found to be in particularly good agreement with experiments. Karagiozis et al. [25] extended the theoretical study of nonlinear stability of clamped-clamped shells conveying annular or internal flow, utilizing the same approach as in [23], with the difference that clamped-clamped beam eigenfunctions were used as admissible functions to describe the shell longitudinal displacement. They also experimentally examined the stability of plastic or aluminium shells with internal water flow. The theoretical and experimental results were in good qualitative and satisfactory quantitative agreement, both showing loss of stability by divergence with a subcritical pitchfork bifurcation which was not followed by flutter, in contrast to linear theory predictions. This raised the question of why experiments with clamped-clamped plastic or aluminium shells subjected to internal water flow show a different type of instability from that of silicone rubber shells conveying airflow; system parameters should not alter the qualitative dynamics of the system from the theoretical point of view. To sum up, although the oscillatory instability observed in experiments with internal airflow was primarily reasoned to be flutter induced by divergence (based on linear theory), nonlinear theory predicted a static instability, i.e., divergence.

Nonlinear vibrations of a fluid-filled, internally-pressurized, soft circular cylindrical shell made of Polyethylene terephthalate fabric were studied in [26]. Experiments on forced, large-amplitude (geometrically nonlinear) vibrations of the shell established the nonlinear stiffness and nonlinear damping characteristics of the system. A reduced-order model was then introduced using a piecewise linear stiffness and viscous damping. The experimental and simulated results of the reduced-order model were in excellent agreement.

Experiments and simulations on chaotic vibrations of a water-filled simply-supported aluminium circular cylindrical shell subjected to radial harmonic excitation in the spectral neighborhood of the lowest resonances were performed by Amabili et al. [27]. They used the maximum Lyapunov exponent to classify the chaotic response of the system. Non-stationary vibrations in addition to a travelling wave response were observed in the experiments and they were numerically reproduced using a reduced-order model based on the Novozhilov nonlinear shell theory. Agreement between experimental and numerical results was particularly satisfactory.

Although there have been some attempts to explain dynamic divergence by means of a ‘sloshing mechanism’ [28], the connection between the two instabilities is rather tenuous; dynamic divergence operates in a completely different regime, having large wall mass, as opposed to the sloshing mechanism in which fluid inertia dominates wall inertia. Besides, the sloshing mechanism requires an upstream boundary condition that allows dynamic variations of the inflow flux, while it is constant in the experiments on dynamic divergence.

To sum up, dynamic divergence is an instability phenomenon starting as a divergence, with amplitude comparable to the shell radius, that largely constrains the flow. This results in pressure building up and reopening the shell, triggering a dynamic instability. Dynamic divergence is only observed in experiments with very flexible shells conveying airflow, whereas shells containing internal water flow or annular airflow lose stability by static divergence. The interested reader is referred to [12] for a more detailed discussion on this paradoxical phenomenon.

1.3 Thesis scope and objectives

This research work is concerned with a soft elastomer (silastic) shell clamped at both ends and subjected to internal airflow, i.e., the system shown in Figure 1-2. Investigating the stability and post-critical behaviour of this system as the flow velocity is varied is the main objective of this study. New experimental observations are presented, aimed at conceptualizing the dynamic divergence phenomenon (i.e., why it basically occurs) and exploring its fundamental characteristics, that is the underlying mechanism. Moreover, the influence of geometric parameters of the shell on the stability and post-critical behaviour of the system is investigated.

1.4 Thesis structure

This is a manuscript-based thesis composed of four chapters. In this chapter (Chapter 1: Introduction), a brief introduction is presented on the background of the stability of thin shells conveying internal and/or annular flow.

The apparatus and testing procedure are described in detail in Chapter 2. The photographs of oscillations, as well as relevant discussion about the mechanism of dynamic divergence are presented in this chapter. Then, the experimental results for a specific shell with given L/R and h/R ratios are analyzed, investigating the effect of flow velocity on the oscillations; some detailed data analysis, including Power Spectral Densities (PSDs), Poincaré maps, phase portrait plots, Probability Density Functions (PDFs) are presented. Additionally, experimental results for a shell pressurized externally are presented in this chapter.

Chapter 3 presents a parametric study on the effects of varying the length and thickness of the shell on the dynamic divergence. The chaotic behaviour of shells with different lengths and thicknesses is explored in this section; the same detailed data analysis tools as in Chapter 3 are employed in this chapter. The effect of confinement, as a result of the presence of a coaxial rigid outer tube, on the dynamic divergence is also discussed in this chapter.

Finally, the conclusions and suggestions for future work are presented in Chapter 4.

1.5 References

1. Blevins, R.D.: Flow-Induced Vibrations. Van Nostrand Reinhold, New York (1990).
2. Weaver, D.S.: On flow induced vibrations in hydraulic structures and their alleviation. Can. J. Civ. Eng. 3, 126–137 (1976).
3. Naudascher, E., Rockwell, D.: Oscillator-model approach to the identification and assessment of flow-induced vibrations in a system. J. Hydraul. Res. 18, 59–82 (1980).
4. Naudascher, E., Rockwell, D.: Flow-Induced Vibrations: An Engineering Guide. AA Balkema, Rotterdam (1994).
5. Païdoussis, M.P.: Fluid-Structure Interactions: Slender Structures and Axial Flow: Vol. 1, Second Edition. Academic Press, Oxford (2014).

6. Païdoussis, M.P.: Fluid-Structure Interactions: Slender Structures and Axial Flow: Vol. 2, Second Edition. Academic Press, Oxford (2016).

7. Dowell, E.H.: Aeroelasticity of Plates and Shells. Noordhoff International Publishing, Leyden (1975).

8. Dowell, E.H.: A Modern Course in Aeroelasticity, Fifth Revised and Enlarged Edition. Springer, Dordrecht (2015).

9. Païdoussis, M.P., Denise, J.-P.: Flutter of cylindrical shells conveying fluid. J. Sound Vib. 16, 459–461 (1971).

10. Païdoussis, M.P., Denise, J.-P.: Flutter of thin cylindrical shells conveying fluid. J. Sound Vib. 20, 9–26 (1972).

11. Done, G.T.S., Simpson, A.: Dynamic instability of certain conservative and non-conservative systems. J Mech Eng Sci. 19, 251–263 (1977).

12. Païdoussis, M.P.: Some unresolved issues in fluid-structure interactions. J. Fluids Struct. 20, 871–890 (2005).

13. Weaver, D.S., Unny, T.E.: On the dynamic stability of fluid-conveying pipes. J. Appl. Mech. 40, 48–52 (1973).

14. Païdoussis, M.P., Chan, S.P., Misra, A.K.: Dynamics and stability of coaxial cylindrical shells containing flowing fluid. J. Sound Vib. 97, 201–235 (1984).

15. El Chebair, A., Païdoussis, M.P., Misra, A.K.: Experimental study of annular-flow-induced instabilities of cylindrical shells. J. Fluids Struct. 3, 349–364 (1989).

16. Amabili, M., Païdoussis, M.P.: Review of studies on geometrically nonlinear vibrations and dynamics of circular cylindrical shells and panels, with and without fluid-structure interaction. Appl. Mech. Rev. 56, 349–356 (2003).

17. Amabili, M.: Nonlinear Vibrations and Stability of Shells and Plates. Cambridge University Press (2008).

18. Alijani, F., Amabili, M.: Non-linear vibrations of shells: A literature review from 2003 to 2013. Int. J. Non. Linear. Mech. 58, 233–257 (2014).

19. Amabili, M., Pellicano, F., Païdoussis, M.P.: Nonlinear stability of circular cylindrical shells in annular and unbounded axial flow. J. Appl. Mech. 68, 827–834 (2001).

20. Amabili, M., Pellicano, F., Païdoussis, M.P.: Non-linear dynamics and stability of circular cylindrical shells containing flowing fluid. Part IV: Large-amplitude vibrations with flow. J. Sound Vib. 237, 641–666 (2000).

21. Amabili, M., Garziera, R.: Vibrations of circular cylindrical shells with nonuniform constraints, elastic bed and added mass. Part II: Shells containing or immersed in axial flow. J. Fluids Struct. 16, 31–51 (2002).

22. Amabili, M., Garziera, R.: Vibrations of circular cylindrical shells with nonuniform constraints, elastic bed and added mass. Part III: Steady viscous effects on shells conveying

fluid. J. Fluids Struct. 16, 795–809 (2002).

23. Amabili, M., Pellicano, F., Païdoussis, M.P.: Non-linear dynamics and stability of circular cylindrical shells containing flowing fluid. Part I: Stability. J. Sound Vib. 225, 655–699 (1999).

24. Amabili, M., Karagiozis, K., Païdoussis, M.P.: Effect of geometric imperfections on non-linear stability of circular cylindrical shells conveying fluid. Int. J. Non. Linear. Mech. 44, 276–289 (2009).

25. Karagiozis, K.N., Païdoussis, M.P., Amabili, M., Misra, A.K.: Nonlinear stability of cylindrical shells subjected to axial flow: Theory and experiments. J. Sound Vib. 309, 637–676 (2008).

26. Balasubramanian, P., Ferrari, G., Amabili, M.: Nonlinear vibrations of a fluid-filled, soft circular shell: experiments and system identification. Nonlinear Dyn. 102, 1409–1418 (2020).

27. Amabili, M., Balasubramanian, P., Ferrari, G.: Travelling wave and non-stationary response in nonlinear vibrations of water-filled circular cylindrical shells: Experiments and simulations. J. Sound Vib. 381, 220–245 (2016).

28. Karazis, K., Païdoussis, M.P.: Dynamic divergence mechanism in shells with internal axial flow, IMECE. 2015-52104 (2015).

2 Characterization of dynamic divergence

Dynamic divergence of circular cylindrical shells conveying airflow

Iman Gholami, Marco Amabili, Michael P. Païdoussis*

Department of Mechanical Engineering, McGill University, 817 Sherbrooke Street West, Montréal Québec, Canada, H3A 0C3

* Corresponding author: Michael.paidoussis@mcgill.ca (M.P. Païdoussis)

2.1 Abstract

Experimental studies have shown that circular cylindrical shells, supported at both ends, conveying internal fluid flow can lose stability by *dynamic divergence* when the shell is highly pliable. This is an instability phenomenon starting as a divergence, with amplitude comparable to the shell radius, that largely constrains the flow. This results in pressure building up and reopening the shell, triggering a dynamic instability. The characteristics of dynamic divergence instability are studied in-depth in this paper for the first time to elucidate the nature and characteristics of this phenomenon. Experiments have been conducted on an elastomer (silicone rubber) thin circular cylindrical shell clamped at both ends and subjected to internal airflow. Bifurcation diagrams have been obtained by varying the flow velocity as the control parameter, exhibiting strong subcritical behaviour and large hysteresis in the flow velocity for the onset and cessation of dynamic instability. The possible existence of a chaotic component in the oscillations was firstly discerned by looking at high-resolution photos taken with a high-speed camera. The existence of chaos in the dynamic response following the initial divergence was then confirmed by means of several qualitative and quantitative measures and criteria for chaos, such as phase plane plots, Poincaré maps, power spectra, the largest Lyapunov exponent, autocorrelation, and probability density function. All these measures have shown that the chaotic nature of dynamic divergence may be intensified or weakened depending on the flow velocity. The results demonstrate that generally at higher flow velocities the oscillations display more complex nonlinear dynamics.

2.2 Introduction

Self-excited oscillations are oscillatory motions due to movement-induced excitation (MIE), meaning that there is no external excitation to the system; in the absence of motion, no oscillatory excitation exists [1,2]. Examples of self-excited oscillations are the flutter of aircraft wings [3,4] and of a cantilevered pipe conveying fluid [5]. They are an important type of flow-induced vibrations in which strong nonlinearities can come into play.

The loss of stability of circular cylindrical shells and pipes supported at both ends is theoretically predicted to be via static divergence, while cantilever shells and pipes generally become unstable by flutter. For a long time, the dynamics of shells subjected to incompressible (subsonic) axial flow seemed uninteresting since they were thought to become unstable only by mild (small-amplitude) divergence. However, some experiments presented in [6,7] breathed new life to the subject by showing that, not only thin cantilevered, but also clamped-clamped shells containing subsonic axial flow *do flutter*. The first linear analytical model for clamped-clamped and cantilevered circular cylindrical shells containing inviscid incompressible flow was presented in [6]. Flügge's shell theory was used for the equation of motion of the shell and the flow field was described by potential flow theory. Travelling wave solutions were assumed for the shell displacement components. The theory predicted that the system loses stability by single-mode flutter for the cantilevered shell, while by divergence and subsequently Païdoussis-type [8] coupled-mode flutter for the clamped-clamped shell. In the experiments, however, flutter was observed directly for clamped-clamped shells; this was at first presumed to be flutter entrained by divergence, but dynamic divergence was another hypothesis suggested later in [9]. In the experiments with clamped-clamped elastomer shells [6], a shell-type flutter in the second circumferential mode (n=2, where n is the number of circumferential waves) was observed. In experiments with short cantilevered shells, only shell-mode oscillations with n=2 or 3 were observed, while being stable in beam-mode flexure. Weaver and Unny [10] presented a linear theoretical model for simply-supported circular cylindrical shells and obtained similar results as for clamped-clamped shells. The shell was predicted to lose stability by static divergence at first, and then by flutter at higher flow velocities.

The theoretical study of the dynamics and stability of clamped-clamped coaxial circular cylindrical shells subjected to internal and/or annular incompressible or compressible flow was extended by Païdoussis et al. [11]. It was found that a shell in annular flow loses stability at a lower flow velocity in comparison with the shell containing internal flow. They also concluded that the critical flow velocity is lower when both shells are flexible. In addition, according to linear theory, the compressibility of the fluid was shown to have little effect on the stability of the system. El Chebair et al. [12] conducted some experiments on clamped-clamped and cantilevered shells subjected to annular flow. They observed that the system loses stability by flutter for a cantilevered shell and by divergence (not followed by flutter) in the case of a clamped-clamped shell.

All of the aforementioned theoretical studies were based on linear models, which are only capable of predicting the first instability encountered by the system with increasing flow velocity, but not the post-instability static or dynamic behaviour. The reason is that geometrical nonlinearities associated with deformation amplitudes of the order of shell thickness start playing an important role in the dynamical behaviour of the system, thus necessitating the use of nonlinear theories. Most of the nonlinear work has been motivated by aerospace applications and hence is associated with supersonic external flow. For an excellent review of nonlinear vibrations of circular cylindrical shells, refer to the work of Amabili and associates [13,14,15,16,17,18 and 19]. Nonlinear dynamics and stability of simply-supported circular cylindrical shells containing inviscid incompressible fluid flow was revisited in [20] by means of Donnell's nonlinear shallow-shell theory and linearized potential flow theory. A seven degree-of-freedom solution allowing for travelling wave response of the shell and shell axisymmetric contraction (responsible for the softening nonlinear behaviour of the shell) was utilized. The results demonstrated that the system loses stability by strongly subcritical divergence.

A refined model for the subcritical static divergence of circular cylindrical shells conveying incompressible fluid, taking into account also geometric imperfections, was introduced by Amabili et al. [21]. Numerical results for thin aluminium shells conveying water were found to be in particularly good agreement with experiments. Karagiozis et al. [22] extended the theoretical study of nonlinear stability of clamped-clamped shells conveying annular or internal flow utilizing the same approach as in [20], with the difference that clamped-clamped beam eigenfunctions were used as admissible functions to describe the shell longitudinal displacement. They also experimentally examined the stability of plastic or aluminium shells with internal water flow. The theoretical and experimental results were in good qualitative and satisfactory quantitative agreement, both showing loss of stability by divergence with a subcritical pitchfork bifurcation which was not followed by flutter, in contrast to linear theory predictions. This raised the question of why experiments with clamped-clamped plastic or aluminium shells subjected to internal water flow show a different type of instability from that of silicone rubber shells conveying airflow; system parameters should not alter the qualitative dynamics of the system from the theoretical point of view. To sum up, although the oscillatory instability observed in experiments with internal airflow was primarily reasoned to be flutter induced by divergence (based on linear theory), nonlinear theory predicted a static instability, i.e., divergence.

Nonlinear vibrations of a fluid-filled, internally-pressurized, soft circular cylindrical shell made of Polyethylene terephthalate fabric were examined in [23]. Experiments on forced, large-amplitude (geometrically nonlinear) vibrations of the shell established the nonlinear stiffness and nonlinear damping characteristics of the system. A reduced-order model was then introduced using a piecewise linear stiffness and viscous damping. The experimental and simulated results of the reduced-order model were in excellent agreement.

To sum up, dynamic divergence is an instability phenomenon starting as a divergence, with amplitude comparable to the shell radius, that largely constrains the flow. This results in pressure building up and reopening the shell, triggering a dynamic instability. Dynamic divergence is only observed in experiments with very flexible shells conveying airflow, whereas shells containing internal water flow or annular airflow lose stability by static divergence. The interested reader is referred to [9] for a more detailed discussion on this paradoxical phenomenon.

In the present paper, the apparatus and testing procedure are described in Sections 2.3 and 2.4. The photographs of oscillations, as well as relevant discussion about the mechanism of dynamic divergence are presented in Section 2.5. Section 2.6 analyzes the experimental results considering the effect of flow velocity on the oscillations; some detailed data analysis including Power Spectral Densities (PSDs), Poincaré maps, phase portrait plots, Probability Density Functions (PDFs) are presented in this section. Experimental results for a shell pressurized from outside are given in Section 2.7. Finally, the conclusions are presented in Section 2.8.

2.3 Apparatus and measuring devices

A schematic of the experimental set-up is shown in Figure 2-1 while a photograph is displayed in Figure 2-2. Air is compressed by a bank of interconnected compressors to about 95 psi (655 kPa), then stored in the tank. A ball valve is used to open or shut off the airflow from the tank towards the apparatus. A pressure control valve (pressure regulator) is utilized to regulate the pressure upstream of the test apparatus, also serving to diminish pressure perturbations from the supply. The flow rate is controlled using a diaphragm valve and a needle valve in parallel, the latter for fine-control. Two piezo-resistive pressure transducers (P_1 and P_2 in Figure 2-1(a)) are used to measure the line pressure, one placed upstream of the control valve and the other before the wooden chamber. A bimetallic thermometer is utilized to read the fluid temperature, T_2. A thermal flowmeter measures the mass flow rate, $\dot{m}$. A Polytec OFV-505 Helium Neon (HeNe) sensor head with a wavelength of 633 nm combined with a digital Polytec OFV-5000 vibrometer controller are used to measure the shell velocity at a target point on the shell.

Under the horizontal surface named ‘Table’, there is a wooden chamber with contracting ends, inside which three screens and a honeycomb are mounted to break up large turbulent eddies and enhance mixing of the high-pressure air coming from the tank; this helps to obtain a uniform flow. On the top, the wooden chamber is connected to a convergent duct Figure 2-1(b)) whose inner diameter decreases gradually to that of the silicone rubber shell. This duct is quite long to make sure that flow is fully developed prior to entering the shell.

The shell velocity is measured at a point at $\frac{1}{3}L$ from the bottom of the shell (marked as ‘higher measurement point’ in Figure 2-3), where L is the length of the shell. All experimental results are obtained from measurements at this point. The velocity of another point at $\frac{1}{5}L$ (called ‘lower measurement point’ in Figure 2-3) is also measured to be able to obtain displacement-triggered Poincaré maps. The signal from the vibrometer laser is fed into a data acquisition system (DAQ) and digitized before being stored in a computer. The DAQ has eight single-ended channels, each having a sampling rate of 5000 samples per second. In addition to the aforementioned instruments, a B&K stroboscope (Figure 2-2) is utilized to slow down or freeze high-frequency motions of the shell for visual inspection. A Photron FASTCAM MiniWX100 high-speed camera is used to take the photos of Section 2.5 with 2000 fps.

The experiments were conducted with a circular cylindrical shell made of silicone rubber (silastic E-RTV), which was cast in a special mould designed for this purpose. To cast the shell, liquid silicone rubber is mixed with a catalyst and then injected into the mould using a syringe; after 72 hours, the injected mixture hardens into an elastic solid and attains its full physical properties. Young's modulus, *E,* of the shell was determined experimentally by means of a tensile test as described in Appendix A. The material density was obtained by measuring the buoyancy force exerted on a cube of silastic (of known weight) when submerged in water, as explained in Appendix 1. The material properties and geometry of the test shells are reported in Table 2-4.

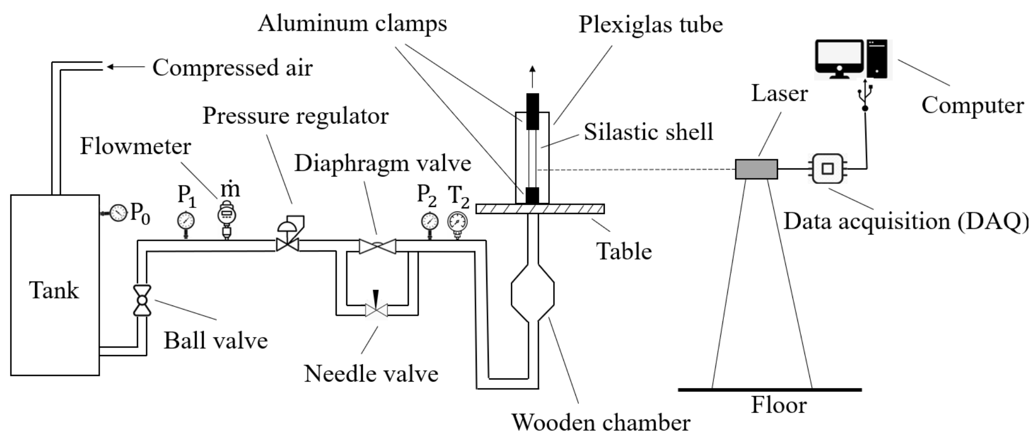

(a)

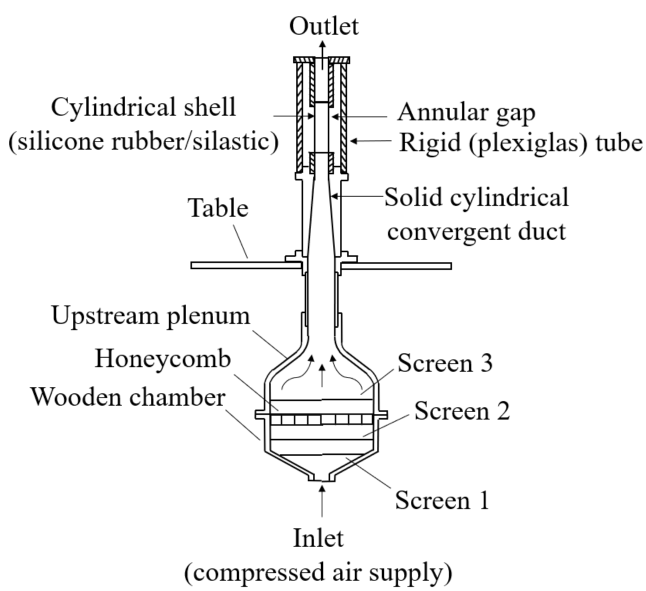

(b)

Figure 2-1. (a) Experimental set-up. Pressure and temperature gauges are indicated by P_0, T_2, etc. (b) Schematic of the wooden chamber and duct supplying air flow to the test section where the shell is installed.

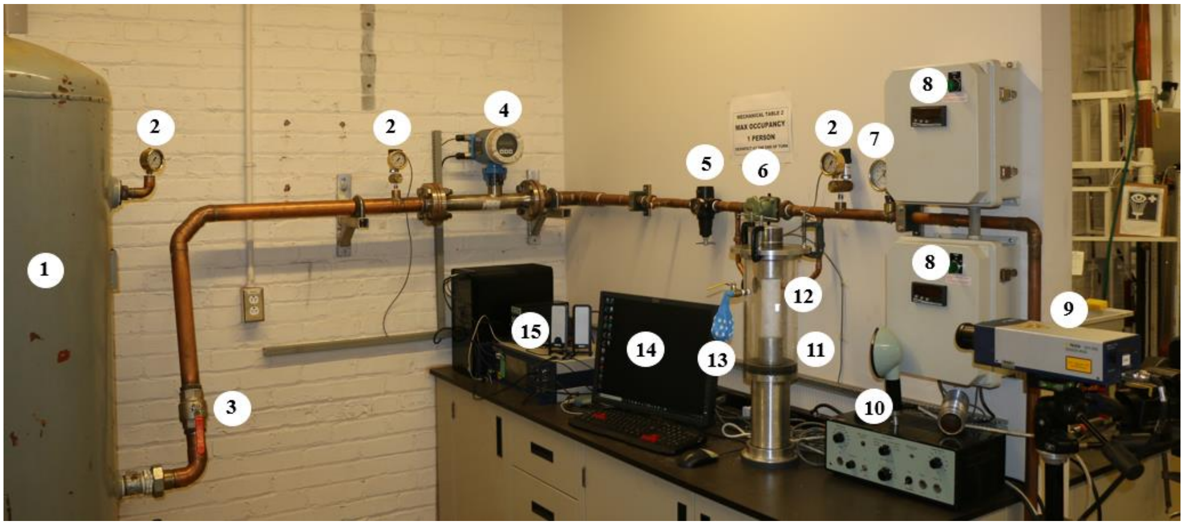

Figure 2-2. Photograph of the experimental setup. 1- Tank, 2- Pressure gauges, 3- Ball valve, 4- Flowmeter, 5- Pressure regulator, 6- Flow control valve, 7- Thermometer, 8- Pressure gauge indicator, 9- Laser head, 10- Stroboscope, 11- Plexiglas annulus, 12- Silastic shell, 13- Balloon, 14- Computer, 15- Laser controller.

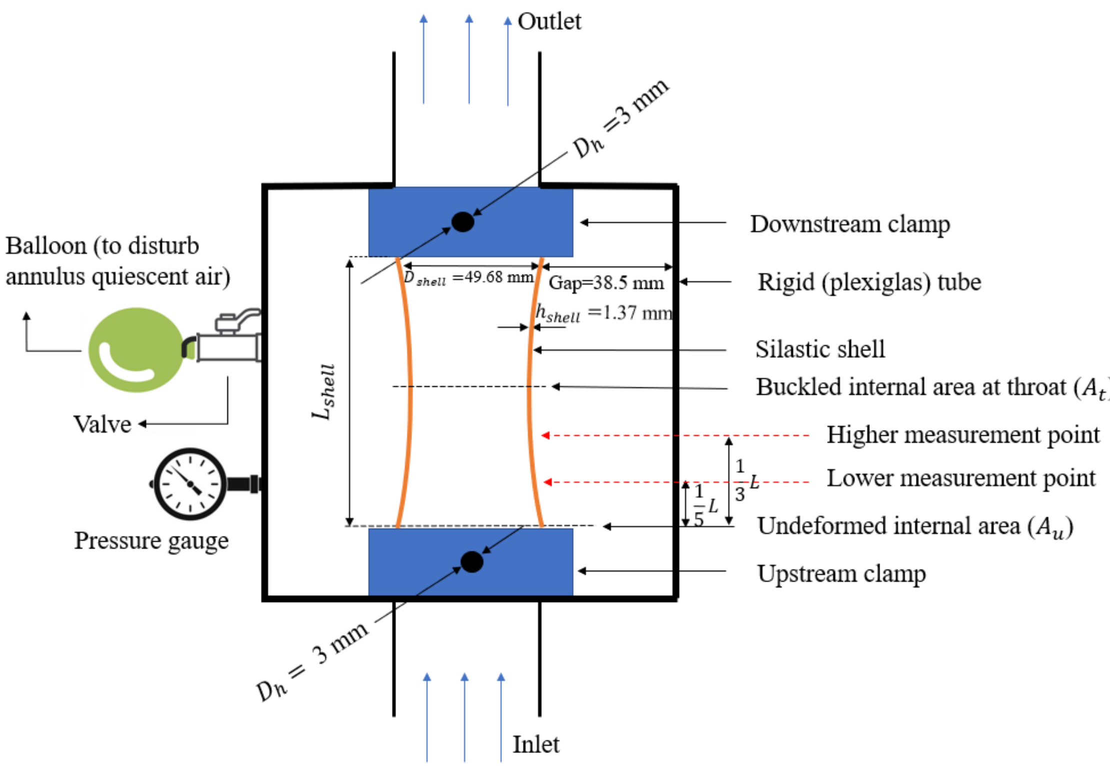

Figure 2-3. Schematic of the test section with the shell.

As seen in Figure 2-3, there are two 3 mm holes in the upper and lower clamps to make sure that the pressure in the annulus equals the average internal pressure, thus ensuring that dynamic divergence is not induced by the difference between internal and external pressure. The detailed results presented in the following sections are based on experiments with this configuration. These two holes are relatively small to minimize any airflow in the annulus.

2.4 Testing procedure

In all tests the following procedure was utilized.

1. The tank was allowed to fill up the set-up with compressed air by gradually opening the ball valve. At this point, the airflow control valves were fully closed. Then, airflow was turned on and incremented in small steps by opening the airflow control valves. The desired flow rate was achieved by tweaking the diaphragm valve and, when necessary, the needle valve. At each flow, the quiescent air in the annulus was disturbed by deflating a balloon mounted on the plexiglas tube, making the shell unstable at a lower flow velocity than that occurring spontaneously; the reason why this was done is discussed in detail in Section 2.5.

2. After the onset of instability, the shell velocity was recorded for 20 s, during which the flow velocity was kept constant. Then, the flow velocity was incremented to a slightly higher value without stopping the shell from oscillating. After a transient period of about 20 s and making sure that flow velocity remained constant, the shell velocity was again recorded for 20 s at the next flow velocity. This procedure was repeated for a few flow velocity increments, and then repeated for decreasing flow velocities up to the flow velocity when the shell stopped oscillating.

2.5 Visualization of the dynamic divergence instability

As mentioned in Section 2.4, fairly strong disturbances were given to the quiescent air in the annulus when incrementing the flow velocity from zero towards the critical one, $V_{cr} = 24.9$ m/s, where the shell becomes unstable. Without these disturbances, the shell remained stable for the maximum flow velocity achieved by the experimental setup. Besides, reaching instability at a lower flow velocity has the advantage that the shell oscillations were less violent, thus, allowing data recording without destroying the shell; the oscillations at high flow velocities are generally so violent that they can easily destroy the shell.

As discussed in Section 2.4, by decreasing the flow velocity after the onset of instability, the shell stops oscillating at a flow velocity referred to as the ‘restabilization flow velocity’, $V_{rest} = 15.6$ m/s. The fact that V_{cr} and V_{rest} are quite different shows that the shell displays a strong softening nonlinear behaviour.

The photographs in Figures 2-4 and 2-5 are taken with the high-speed camera from above and front of the shell, respectively, at the disturbance-induced critical flow velocity, $V = V_{cr} = 24.9$ m/s. At the onset of instability, a divergence with the shape of n=2 circumferential waves and one longitudinal half-wave (m=1) is observed. This static instability restricts the flow passage, resulting in an increase of pressure that reopens the shell walls and triggers a dynamic instability (dynamic divergence). Based on the photographs, the following oscillations evolve in 3 phases through time. In phases 1 and 2, which totally last about 100 ms, the oscillations are regular and well-ordered, starting with circumferential mode n=2 (phase 1, Figures 2-4(a) and 2-5(a)), changing to n=3 (phase 2, Figures 2-4(b) and 2-5(b)). Phase 1 consists of low-frequency, low-amplitude oscillations about the buckled position. In the first 3-4 cycles of oscillation in phase 1, the shell does not collapse completely and the airflow is only partially obstructed. In the last cycle of Phase 1, however, the shell closes completely and the opposing walls touch each other very gently. This full closure drives the shell into phase 2.

In phase 2, the amplitude and frequency of oscillations increase compared to phase 1. The shell fully closes and then reopens completely in each cycle. Although the shell fully obstructs the airflow in each cycle in phase 2, the walls touch each other gently similar to the last cycle of phase 1.

In phase 3, as seen in Figures 2-4(c) and 2-5(c), the oscillations are regular and well-ordered at the beginning with moderate impact of the opposing walls. However, more irregular cross-sectional shapes, involving more wrinkles and rotations (twisting), appear in later times in phase 3, as seen in Figures 2-4(d) and 2-5(d), and the oscillations appear to be chaotic with mode shapes changing intermittently from n=2 to higher, not well-defined, mode shapes. The opposing walls start to impact on each other violently and the impact becomes more severe with the passage of time. Furthermore, several wrinkles emerge when the mode shape changes to higher than n=2, with more irregular mode shapes, as seen in the photograph corresponding to t=1790.5 ms in Figure 2-4(d).

The evolution of putative chaos in the system with time is of particular interest, because routes to chaos are usually associated with changing a control parameter of the system (e.g., the flow velocity), not with the passage of time. This is one of the most interesting characteristics of the dynamic divergence phenomenon observed in the present experiments.

The lack of violent impact between opposing shell walls may be the reason why oscillations are much more regular in the first two phases, compared to phase 3. It is interesting to note that anti-phase mode shapes occur in consecutive cycles in phases 2 and 3, meaning that nodes of the oscillation are displaced (rotated) π/n radians in each cycle, compared to the previous one; for example, the photographs corresponding to t = 131 and 140.5 ms in Figure 2-4, display a 90 degrees phase difference. It is noteworthy that the maximum radial displacement (collapse) occurs at the upper half of the shell, as observed in Figure 2-5, which shows the axial pattern of the motions.

Phase 3 which consists of irregular and chaotic-looking oscillations is dominant in the results presented in Section 2.6, since the first two phases vanish very quickly, after nearly 100 ms from the start of oscillations, while 20 s of oscillations have been recorded at each flow velocity step analyzed. In conclusion, oscillations seem to be of a chaotic nature and, depending on the flow velocity, this chaotic behaviour can be strong or weak. The duration of the first two (primary) phases becomes shorter at higher flow velocities.

The dynamics, as illustrated in the photographs of Figures 2-4 and 2-5, is qualitativly similar to the behaviour of shells with other length-to-radius ratios, *L/R*, and thickness-to-radius ratios, *h/R*, elastomer shells, not presented in this paper.

Based on calculations presented in Appendix 2, in the first cycle of oscillations when obstruction of airflow is minimum compared to other cycles (the photograph corresponding to t=38.5 ms in Figure 2-4), the flow is indeed compressible and chocked at the throat. The high flexibility of the shell obstructs the airflow by 89% in the first cycle of oscillations, as discussed in Appendix B. The airflow is fully blocked in each cycle of oscillations in phases 2 and 3 of oscillations; hence, compressible. Thus, the incompressibility assumption in the theoretical studies of the stability of such a pliable shell would not be accurate and the compressibility of the flow and its effect on the fluid-related forces should be taken into account to determine the post-buckling dynamics. This may shed light on the question why oscillatory response is only possible for flexible clamped-clamped shells subjected to internal airflow, but not for plastic or aluminium shells conveying water flow [22].

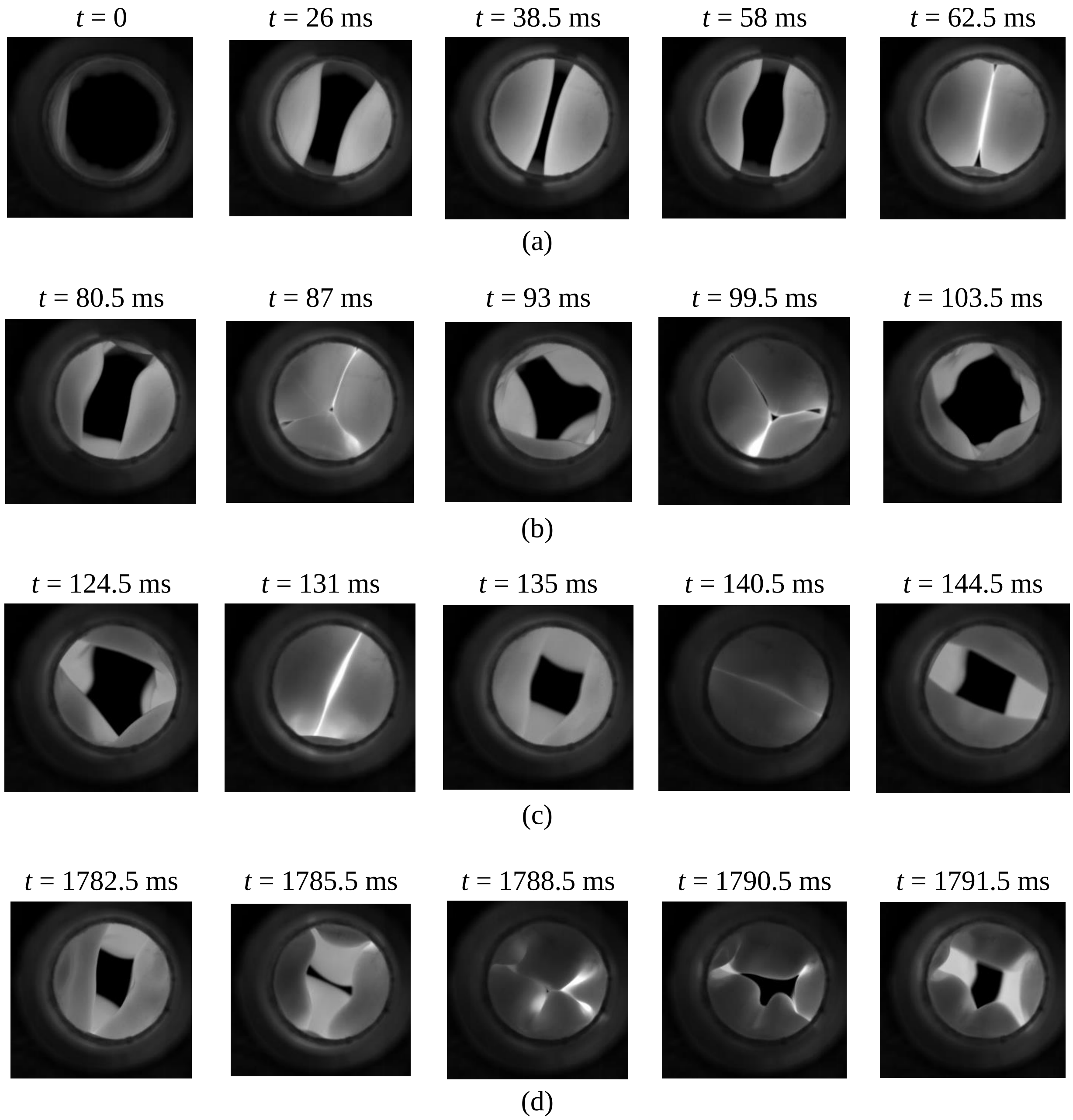

Figure 2-4. Cross-sectional patterns of motion, viewed from above the shell at $V = V_{cr} = 24.9$ m/s. (a) Phase 1 of the oscillations with $n = 2$ (regular oscillations); (b) phase 2 of the oscillations with $n = 3$ (regular oscillations); (c) phase 3 of the oscillations with $n = 2$; (d) continuation of phase 3 with more irregular and distorted (chaotic-looking) oscillations.

t = 0 *t* = 27.5 ms *t* = 39 ms *t* = 45 ms *t* = 49.5 ms *t* = 54 ms

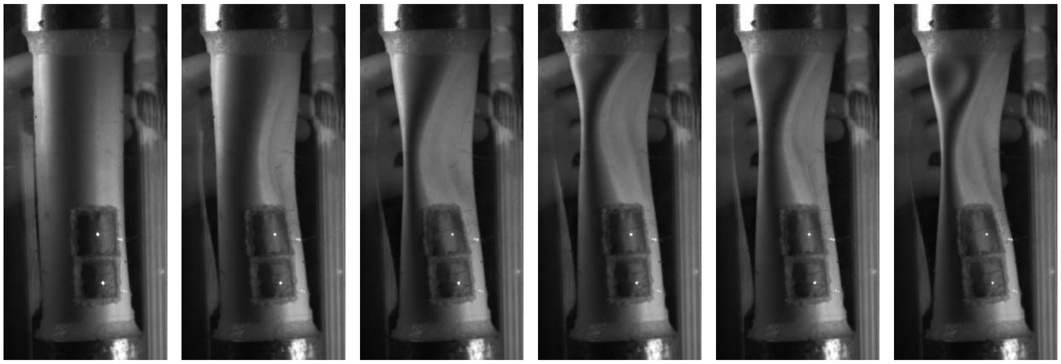

(a)

t = 96 ms *t* = 99.5 ms *t* = 103.5 ms *t* = 105.5 ms *t* = 112 ms *t* = 115.5 ms

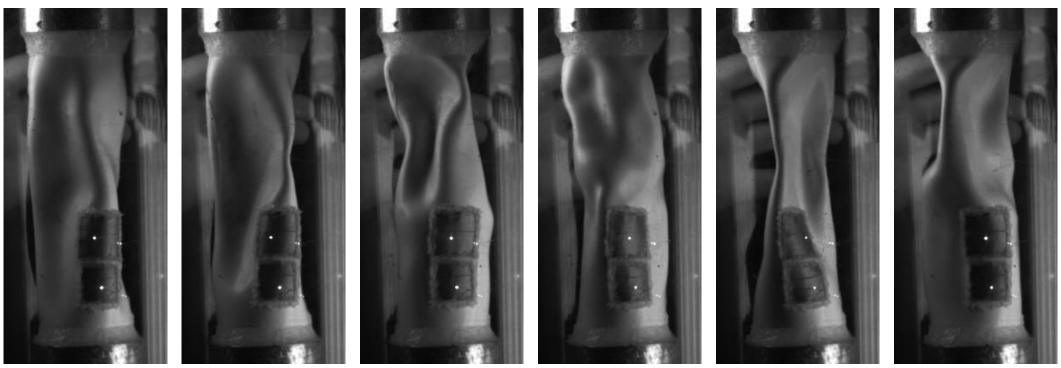

(b)

t = 174.5 ms *t* = 177 ms *t* = 182 ms *t* = 184 ms *t* = 186.5 ms *t* = 189 ms *t* = 192.5 ms

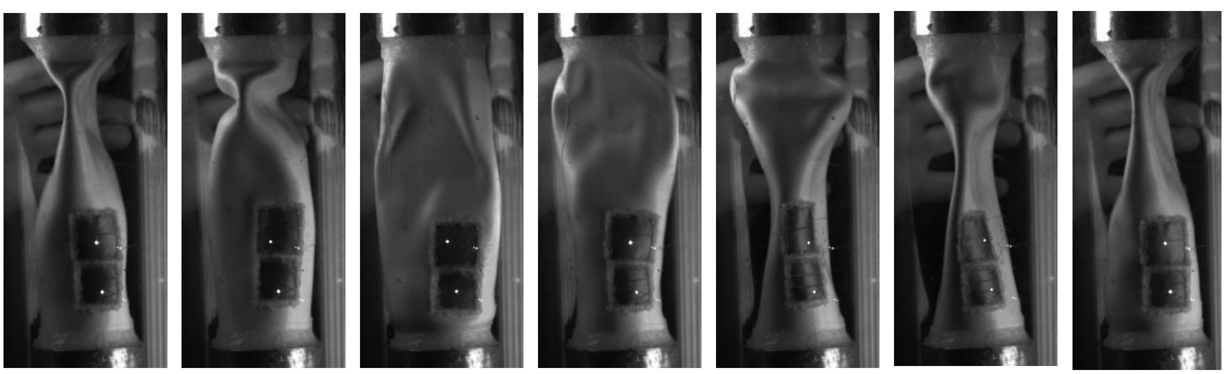

(c)

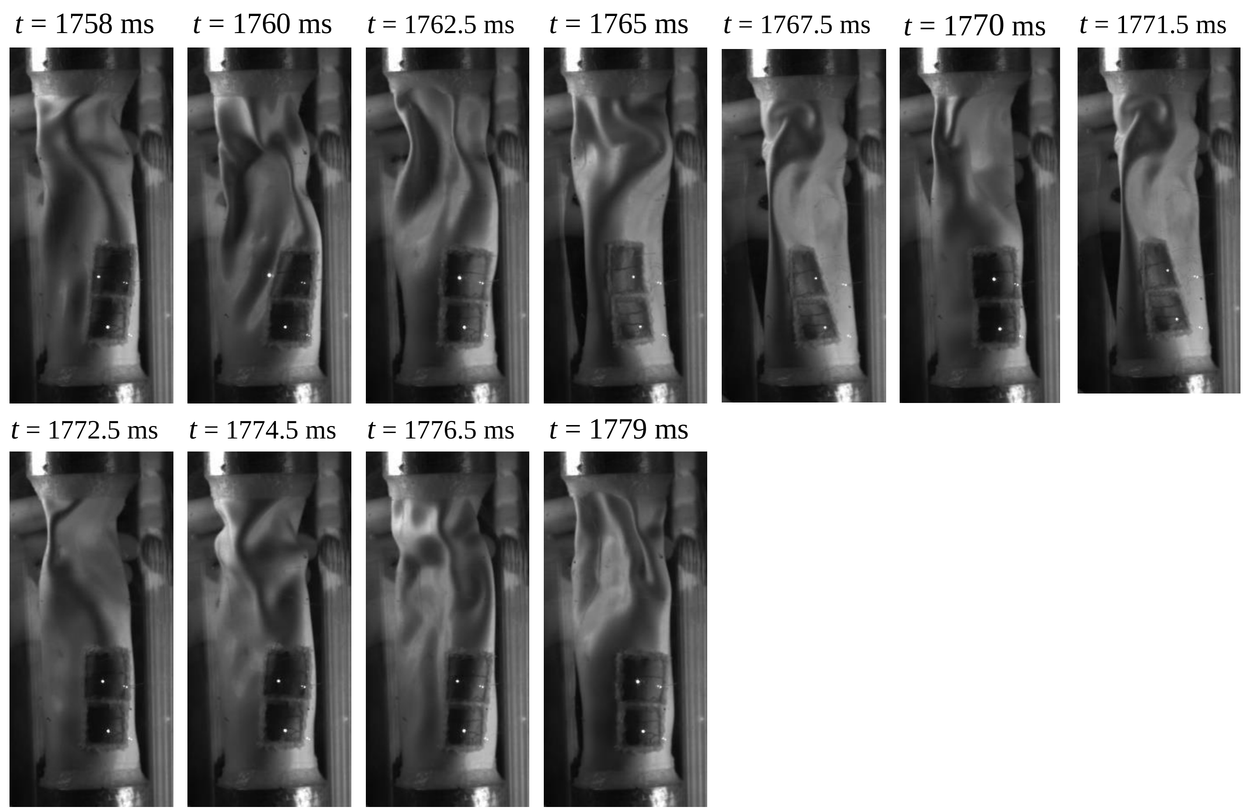

(d)

Figure 2-5. Axial patterns of motion, viewed from the front of the shell at $V = V_{cr} = 24.9$ m/s. (a) Phase 1 of the oscillations with $n = 2$ (regular oscillations); (b) phase 2 of the oscillations with $n = 3$ (regular oscillations); (c) phase 3 of the oscillations with $n = 2$; (d) continuation of phase 3 with more irregular and distorted (chaotic-looking) oscillations.

After the primary period of regular oscillations (phases 1 and 2), the shell closes completely for about 4 ms in each cycle in phase 3, thus fully blocking the airflow. This closure of the shell forms a ‘bubble’ at the bottom of the shell. Note that the duration of one oscillation is about 8 ms, meaning that, for half of the period of each cycle, the shell is completely closed. As a result, the flow pressure upstream of the buckled cross-section increases, and this build-up in pressure tends to reopen the shell. Thus, the bubble at the bottom of the shell is pushed upward (see Figure 2-6). When this bubble has travelled through the lower half of the shell and is in the upper half, because of the forces leading to divergence and inertia, the reopened lower half of the shell does not regain its circular cross-sectional shape, but it buckles in an antiphase shape in the middle of the shell. This means that a new cycle begins to form while the previous one is still evolving and has not finished yet. When the bubble has completely travelled through the length of the shell, the wall collapse in the anti-phase mode reaches its maximum (full closure) and a new bubble reappears at the bottom of the shell, and the new cycle of oscillation starts. The dynamic repetition of this sequence of buckled antiphase shapes gives rise to the *dynamic divergence* phenomenon which is indistinguishable from flutter. Dynamic divergence, however, should not be misinterpreted as flutter, which typically presents a specific oscillation frequency at its onset.

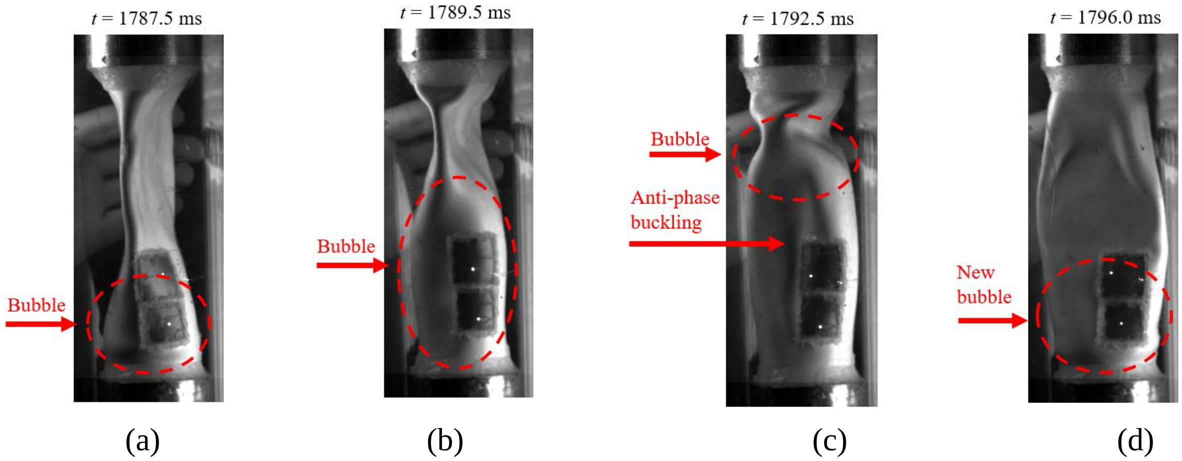

Figure 2-6. Bubble traveling mechanism at $V = V_{cr} = 24.9$ m/s. (a) Formation of a bubble at the bottom of the shell. (b) Movement of the bubble upwards. (c) Anti-phase buckling at the middle of the shell when the bubble is at the upper half of the shell. (d) Formation of a new bubble at the bottom of the shell as a new cycle starts.

The Fourier transform may not be the best tool to analyze nonstationary signals whose frequency content changes over time. Here, wavelets come into play as a powerful tool which is localized in both time and frequency. A wavelet is a rapidly decaying wavelike oscillation that has zero mean and a finite duration. Wavelets come in different sizes and shapes [24]. Figure 2-7 shows the magnitude of the continuous wavelet transform (CWT) of the shell velocity signal in the frequency-time domain, using Morse wavelets. This is commonly called a wavelet scalogram [24]. Phases 2 and 3 of the oscillations are recognized in Figure 2-7. Phase 1 consists of only 4 cycles with low amplitude and frequency; so, it does not appear in the wavelet scalogram. Phase 2, however, extends from ~50 ms up to ~110 ms, corresponding to photographs in Figures 2-4(b) and 2-5(b). The frequency of oscillations increases as phase 2 evolves to phase 3. The increase of the frequency of oscillation from phase 2 to phase 3, is in agreement with the observations in Figures 2-4 and 2-5. As discussed already, the shell behaviour in phase 3 becomes irregular with more wrinkles and rotations (twisting) at intermittent periods of time. A cone of influence (COI) is defined in Figure 2-7, outside which the results are affected by edge-effect artifacts and are not reliable; edge effects are associated with the stretched wavelets extending beyond edges of the observation interval. Thus, outside the shaded region, one can make sure that the time-frequency representation of the signal is accurate.

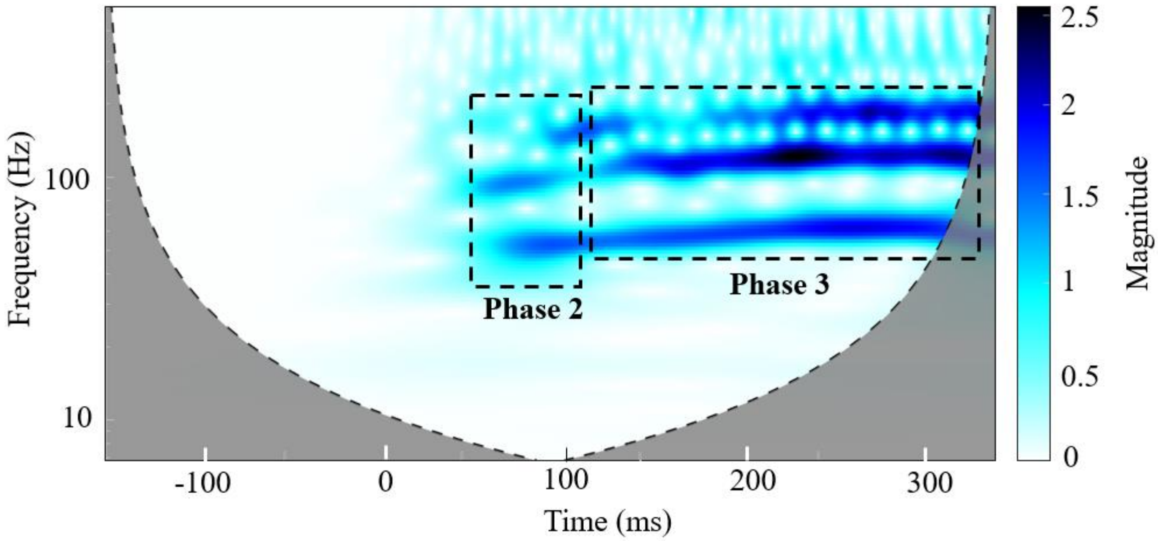

Figure 2-7. Morse wavelet scalogram of shell velocity signal at $V = V_{cr} = 24.9$ m/s, showing the increase of the frequency of oscillations from phase 2 to 3.

The photographs of phase 3 of the oscillations at $V = V_{rest} = 15.6$ m/s are seen in Figure 2-8. Note that Figures 2-4 and 2-5 correspond to the oscillation at the disturbance-induced critical flow velocity $V = V_{cr} = 24.9$ m/s. The aim is to have a qualitative visual comparision between the oscillations at the critical (high) and restabilization (low) flow velocities. It is seen that the oscillations at the restabilization flow velocity, in Figure 2-8, are more regular and less chaotic-looking than those in Figures 2-4 and 2-5. Fewer wrinkles and less irregular mode shapes are observed and the walls impact on each other less violently, compared to the oscillations at the critical flow velocity. The frequency of the oscillations is ~100 Hz which is lower than the frequency at the critical flow velocity, ~120 Hz.

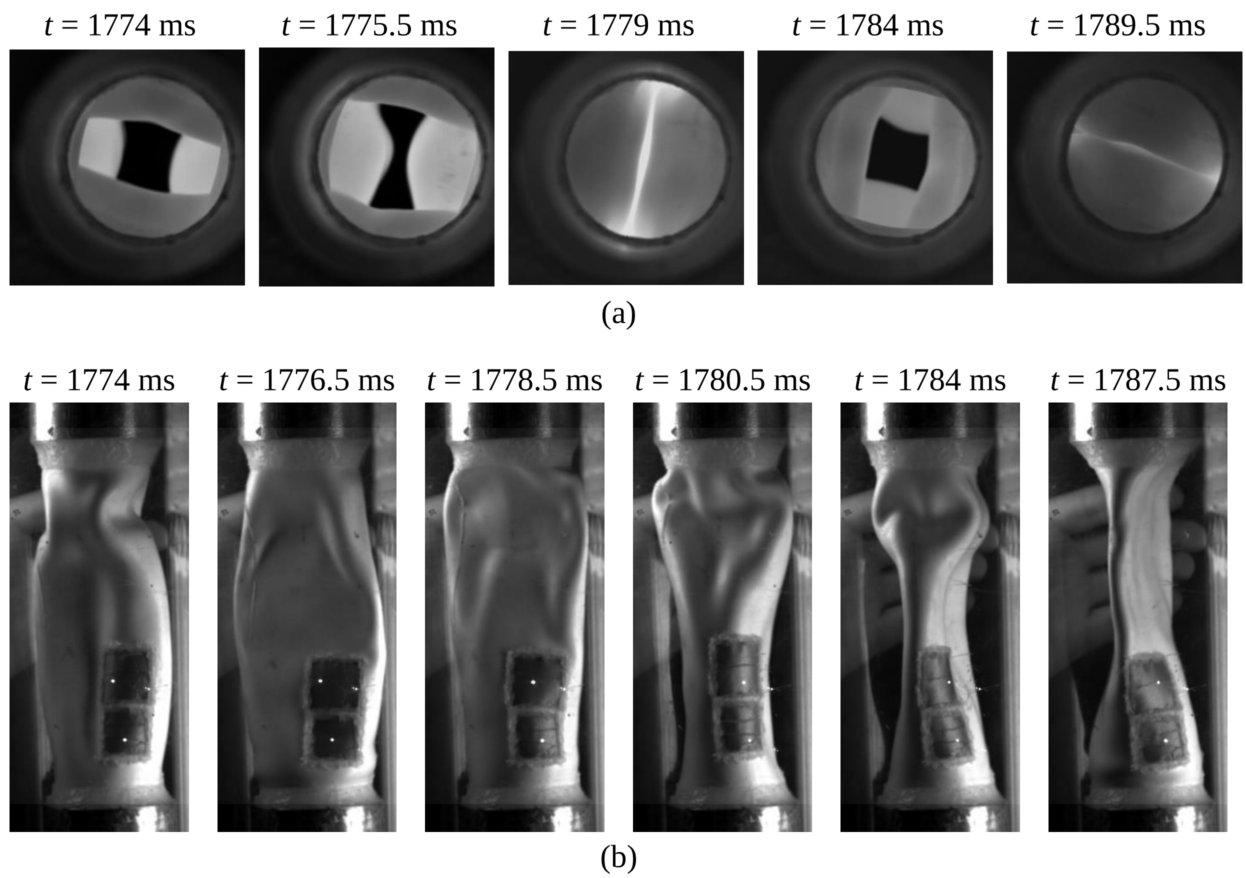

Figure 2-8. Photographs of the oscillations at $V = V_{rest} = 15.6$ m/s. (a) Cross-sectional patterns of motion, viewed from above the shell. (b) Axial patterns of motion, viewed from the front of the shell.

2.6 Detailed experimental results and their analysis

In this section, a detailed description of the dynamics of the shell is given, as the flow velocity is increased, up to the critical point of onset of oscillations, $V_{cr} = 24.9$ m/s, and then as the flow velocity is decreased to the point of cessation of oscillations, $V_{rest} = 15.6$ m/s [1]. The results presented in this section prove that a weak or strong chaotic component exists in the motion, depending on the flow velocity. The existence of chaos in the system was first suggested by the photographs of the oscillations presented in Section 2.5, and it is confirmed by other measures of chaos in this section. Chaotic motions are unpredictable, nonperiodic, random-like motions which are very sensitive to the initial conditions, and correlation of present with past is lost rapidly with time. Chaotic vibrations occur when there are some strong sources of nonlinearity in the system. Possible sources of nonlinearity include material nonlinearity associated with a nonlinear stress-strain relation (nonlinear elastic behaviour as seen in Figure 2-19), geometric nonlinearity due to large deformations, nonlinear damping, flow-induced forces, nonlinear boundary conditions (such

[1] The experimental results for shells with different length-to-radius (*L/R*) and thickness-to-radius (*h/R*) ratios are deferred to a future paper.

as deformation-dependent constraints) and many others [25]. Chaotic phenomena have been observed in many physical systems. Examples of chaotic motions in mechanical systems include vibrations of buckled elastic structures [26], aeroelastic problems [27] and, large-amplitude vibrations of structures such as beams, plates and shells [28, 29].

It is always recommended not to count on only one indicator of chaos in dynamics experiments, but to use several techniques before pronouncing a system as chaotic. As an example, a broad spectrum of frequencies, particularly low frequencies, is often considered as an indication of chaos in the system. However, for systems with a large number of degrees of freedom, the power spectrum may not be a sufficient decider. Subharmonics in the frequency spectrum are usually thought to be a forerunner to chaotic vibrations. However, other routes to chaos are possible, such as through quasiperiodicity and intermittency [25].

2.6.1 Dynamic behaviour with varying flow velocity

The bifurcation diagram of the system is presented first. Then, two qualitative measures, namely the largest Lyapunov exponent and wavelet analysis, have been employed to investigate the chaotic behaviour of the system with varying flow velocity. These results are then confirmed by other measures presented in Section 2.6.2.

The variation of the rms of the shell velocity is investigated as the flow velocity changes to obtain the bifurcation diagram of Figure 2-9. In this figure, a linear regression has been performed on the rms of shell velocity versus flow velocity. It demonstrates that by reducing the flow velocity below the critical value, the rms of shell velocity generally decreases. Nevertheless, at some specific ranges of low flow velocity, the rms increases, rather than decreases, with decreasing flow velocity (e.g., points C and E).

One should be careful not to conclude from the bifurcation diagram that oscillations with smaller rms are necessarily less violent or chaotic than those with higher rms. Indeed, the largest Lyapunov exponent, Figure 2-10, along with other qualitative and quantitative measures presented in Section 2.6.2 should be considered to decide on the system behaviour at different flow velocities.

As seen in the bifurcation diagram, Figure 2-9, the restabilization flow velocity, V_{rest}, is much smaller than the critical flow velocity, V_{cr}, indicating a strong softening nonlinear behaviour. A softening nonlinear behaviour is associated with a subcritical bifurcation at the critical value of the control parameter, in this case the flow velocity.

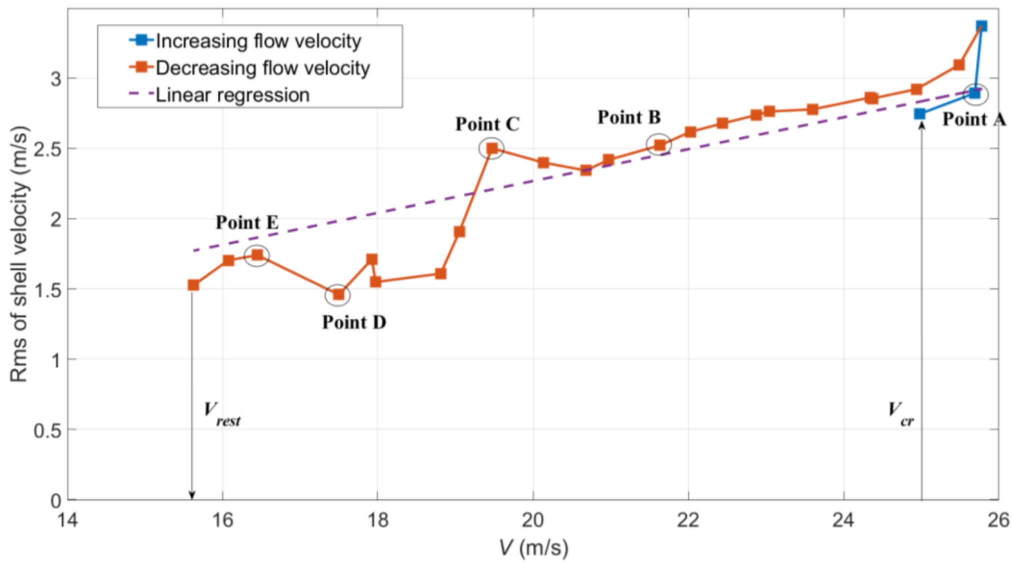

Figure 2-9. Bifurcation diagram of the rms velocity of the shell. The critical and restabilization flow velocities are denoted by V_{cr} and V_{rest}, respectively.

In this study, the Wolf algorithm was employed to determine the largest Lyapunov exponent from the time series [30]. The largest Lyapunov exponent indicates the dependency of the system on initial conditions. For bounded physical systems, the divergence of chaotic orbits can only be locally exponential and the distance between two trajectories cannot go to infinity. Therefore, the exponential growth along the reference trajectory, called a 'fiduciary', is averaged at many points. When the distance between the two trajectories exceeds a limit called 'maximum separation parameter', the reference trajectory is kept and the other one is replaced by a new nearby trajectory. This replacement is done because Lyapunov exponents quantify the divergence of orbits, which, although they move away from each other rapidly, they always remain infinitesimally close to each other. More details on how to select delay, embedding dimension, maximum separation at replacement, and other parameters can be found in [30]. It is obvious that oscillations with a stronger chaotic component (points A, B, and D in Figure 2-10) have larger λ_1 in comparison to motions with a weaker chaotic component (points C and E).

The Wolf algorithm estimates the dominant Lyapunov exponent (λ_1) based on the average divergence of close-by orbits in the reconstructed (pseudo) phase space. It always calculates positive values for λ_1; however, if the estimated exponent is near zero (small), the system is exhibiting some sort of orbital stability, or periodicity, while when it is large, the system is showing a chaotic behaviour. Now, the question arises "when is an estimated exponent considered small or large?" To answer this question, one should consider the estimated exponent when the system is exhibiting periodicity according to other measures such as PSD, Poincaré map, phase portrait, PDF, autocorrelation, etc. To pronounce that the system undergoes a transition from periodicity to chaos, the estimated exponent should grow by orders of magnitude; for example, in Figure 2-10, the estimated exponent at point A is about 20 times its value at point E, where the system shows periodicity according to several measures, as displayed in Figure 2-16. Thus, it can be concluded that the system undergoes a transition from periodicity to chaos by decreasing flow velocity from point A to point E in Figure 2-10.

According to Figure 2-10, the largest Lyapunov exponent generally takes greater values at higher flow velocities (points A and B). By decreasing the flow velocity from point B, the largest Lyapunov exponent sharply drops, indicating that motions are more predictable and less sensitive to uncertainties in initial conditions. However, by further decreasing flow velocity towards point D, oscillations restart to show increasing irregularity and λ_1 increases abruptly. Finally, λ_1 decreases again by reducing the flow velocity from point D to E. The very small λ_1 associated with points C and E suggests that there is but a very weak chaotic component in the motion. The trend observed in the Lyapunov diagram, Figure 2-10, is in agreement with other qualitative and quantitative results in Figures 2-12 - 2-16.

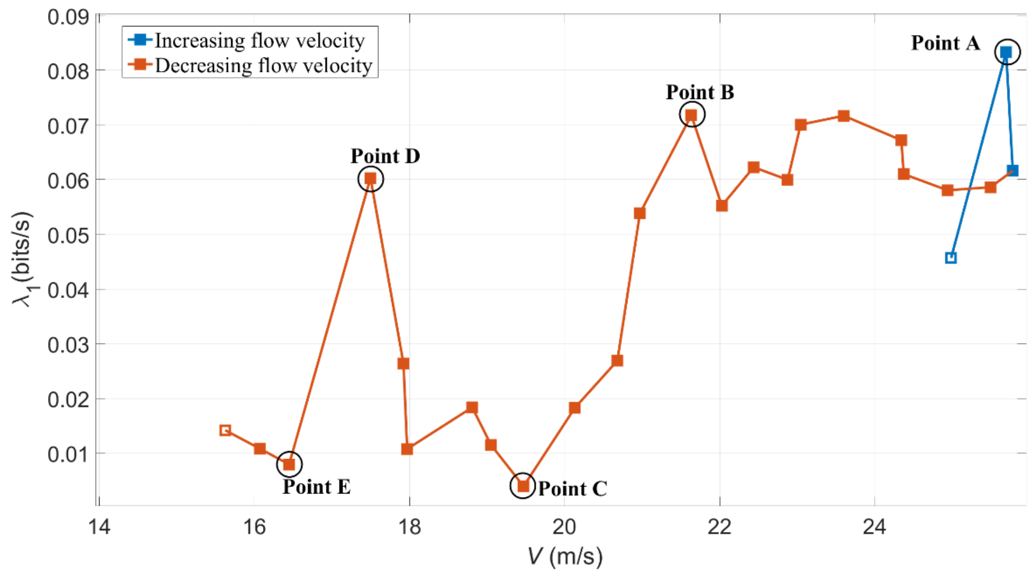

Figure 2-10. Largest Lyapunov exponents, λ_1, at different flow velocities. Hollow markers indicate the critical and restabilization flow velocities.

The wavelet analysis of signals at various flow velocities using Morse wavelets is seen in Figure 2-11. A detailed discussion of the concept and usage of wavelets has been given in Section 2.5. Figure 2-11 has the same range of flow velocities as the bifurcation diagram, meaning that the first vertical strip in Figure 2-11 (denoted by 1 at the bottom of the strip) corresponds to the critical flow velocity (V_{cr}=24.9 m/s), and the last strip corresponds to the restabilization flow velocity (V_{rest} = 15.6 m/s), where the shell stops oscillating. It is obvious that the frequency ranges (bands) containing high-energy content (in dark blue) tend to be lower with decreasing flow velocity, with the exception of a jump upwards at V=19.0 m/s. In addition, at flow velocities above 19.0 m/s, the smallest frequency range is dominant.

At most flow velocities, there are three frequency ranges. They are not distinct from each other at some flow velocities, making wide and broad frequency ranges (e.g., points A, B, and D). A broad-band spectrum can be an indication of chaos in the system; because it shows a broad-band frequency content, rather than a number of specific frequency peaks. On the other hand, at some flow velocities (e.g., points C and E), the frequency bands are narrower and more well-defined; hence, one may expect the system to be less chaotic and have a dominant periodic component at these flow velocities. The prediction of chaos at different flow velocities discussed here, completely agrees with the results presented in Section 2.6.2.

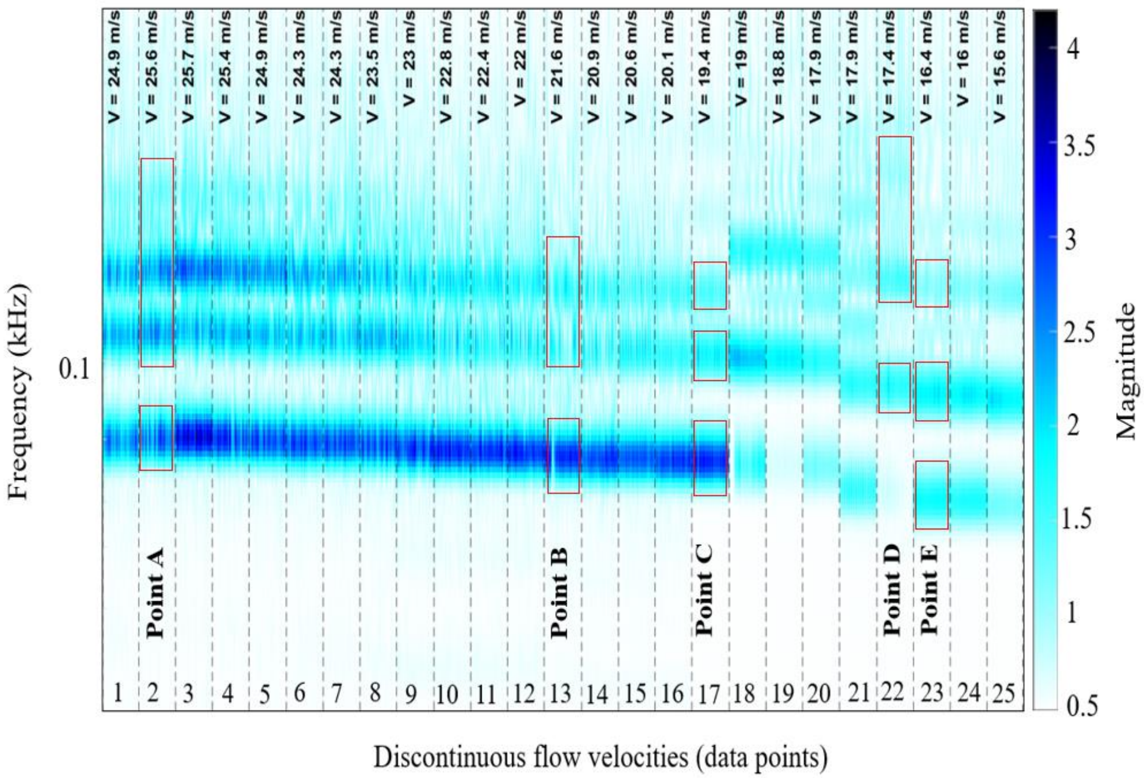

Figure 2-11. Morse wavelet scalogram at discontinuous flow velocities indicated by numbers at the bottom of the diagram (1-25); 20 s of oscillations at each flow velocity have been recorded and analyzed. The red boxes show the frequency bands at selected flow velocities. The larger the total area of the boxes at a point (flow velocity) are the more chaotic behaviour that point shows.

2.6.2 Analysis of the results

In this section, detailed results for selected points, defined in Table 2-1, will be presented. Qualitative measures such as Poincaré maps, phase portraits, the pseudo-phase space, as well as quantitative ones, including the power spectra, probability density function (PDF) and autocorrelation, have been employed to assess the chaotic component of the motion.

These results are based on the configuration with 2 holes, hence the average internal and the annulus pressure are the same. The signal is obtained from the higher measurement point on the shell (see Figure 2-3). Phase 3 of oscillations shown in Figures 2-4 and 2-5 is the dominant phase in the results to be shown, since the first two phases consisting of regular oscillations last 0.5 s, while 20 s of oscillations have been recorded at each flow velocity step.

Table 2-1. Selected points for presenting detailed results and corresponding flow velocities, *V*.

Point	A	B	C	D	E
V (m/s)	25.6	21.6	19.4	17.4	16.4

2.6.2.1 Power spectra

Points C and E, as expected from their largest Lyapunov exponent in Figure 2-10, are associated with oscillations with a dominant periodic component. Thus, their PSDs, Figures 2-14(b) and 2-16(b), display a finite number of well-pronounced commensurable peaks which are superharmonics of the fundamental frequency. A chaotic signal, however, has a wide frequency bandwidth with a nearly continuous distribution of frequencies as opposed to discrete sharp spikes in a PSD associated with a periodic motion. Therefore, the PSDs of points A and B, Figures 2-12(b) and 2-13(b), respectively, clearly signify a strong chaotic behaviour since they are not only broad-band, but also have cone-like peaks instead of sharp spikes. One should note that the frequency range of the PSDs plotted is quite wide (0-500 Hz); hence, the cone-like peaks imply a frequency band, not a specific frequency value. The PSD associated with Point D, Figure 2-15(b), shows a wide range of conspicuous sharp peaks, which are not necessarily superharmonics of the fundamental frequency. This suggests that the corresponding motion has a chaotic component stronger than for points C and E, but weaker than for points A and B.

2.6.2.2 Phase portrait plots

As seen in Figures 2-12(c), 2-13(c) and 2-15(c), trajectories tend to fill a certain subspace of the phase planes of points A, B and D, respectively. This suggests a chaotic component to the oscillation, whereas the phase portrait of points C and E (Figures 2-14(c) and 2-16(c), respectively), show cleaner orbits, which suggest a strong periodic component.

2.6.2.3 Poincaré maps

Here, we have employed displacement-triggered Poincaré maps which are obtained by sampling the data when another variable of the system reaches a peak value. This method is often used when a natural time clock such as the external periodic force does not exist. In this study, when the velocity of the lower measurement point crosses from negative to positive meaning that its displacement has a local maximum value, time is stored. Then, the velocity and displacement of the upper measurement point at the sampled instances are used to plot the Poincaré map. The Poincaré map of periodic motions has a finite number of points, whereas chaotic oscillations have a fractal-looking collection of points.

In agreement with the largest Lyapunov exponent results of Figure 2-10, Poincaré maps of points A, B and D, in Figures 2-12(d), 2-13(d) and 2-15(d), respectively, display scattered clouds of points, indicating a relatively strong chaotic behaviour. On the other hand, points C and E in Figures 2-14(d) and 2-16(d), respectively, have Poincaré maps consisting of a finite number of points with smooth basin boundaries.

The oscillations at point E are clearly period-2 since (i) the PSD, Figure 2-16(b), shows a subharmonic, $\frac{1}{2}f_1$=40 Hz, (ii) the Poincaré map, Figure 2-16(d), consists of two clean basin boundaries, and (iii) the phase portrait, Figure 2-16(c), consists of two intertwined sets of orbits. The oscillations at point C seem to be period-4, according to the Poincaré map, Figure 2-14(d), having 4 basins of attraction; however, taking into account the corresponding PSD and phase portrait, Figures 2-14(b) and 2-14(c), respectively, it can be concluded that the four basins are really two diffuse basins, thus suggesting period-2 oscillations with small, but not negligible, frequency content between $\frac{1}{2}f_1$ and f_1, compared to the PSD of point E, Figure 2-16(b).

In periodic motions, the basin boundaries are a smooth, continuous line or surface, indicating that small uncertainties in the input parameters do not influence the response of the system when away from the basin boundaries. However, many nonlinear systems have fractal basin boundaries, meaning that the boundary is nonsmooth. The existence of fractal basin boundaries has a strong bond with the dynamics of the system [25]. In the present experimental results, it is obviously seen that basin boundaries are nonsmooth and fractal, meaning that a small change in the control parameter, i.e., flow velocity, changes the system behaviour. Thus, predictability in such a system is not always possible. For example, pay attention to the Poincaré maps of points C, D and E, Figures 2-14(d) - 2-16(d). For point C, two diffuse basins exist. However, with a small decrease of flow velocity, the four basins merge into one fuzzy basin, as seen in the Poincaré map of point D (Figure 2-15(d)). With further decrease of the flow velocity, two clean basins appear in the Poincaré map associated with point E in Figure 2-16(d).

2.6.2.4 Pseudo-phase spaces

Pseudo-phase space, sometimes called delay-reconstructed phase space, has been constructed to (i) have an impression of the behaviour of orbits in phase space, (ii) calculate the largest Lyapunov exponent of chaotic time series. The maximum Lyapunov exponent was used in [31] to classify chaos near resonance for water-filled circular cylindrical shells. A periodic motion will have a closed orbit in both delay-reconstructed phase space and in the phase space constructed with more than one system variable. Chaotic time series, on the other hand, form fractal orbits with orbital segments, showing sensitive dependence on the initial conditions, in both delay-reconstructed phase space and in the phase space constructed with more than one system variable.

Here, the embedding dimension is chosen by the method of 'educated guesses' to ensure that the orbit is topologically reasonable in m dimensions and unnecessary self-intersection does not occur. The choice of delay is made by selecting values for d that expand the pseudo-orbit as much as possible with respect to the noise amplitude in the system, while maintaining a deterministic orbit structure [32]. Then, the consistency of results is examined by selected nearby values for the delay. The results, however, show a weak dependence on the choice of delay. A detailed discussion about the selection of delay and embedding dimension is presented in [30].

Pseudo-phase spaces associated with selected data points are presented in 2-12(d)- 2-16(d). It is clearly seen that the pseudo-phase spaces corresponding to points C and E are closed orbits indicating that the motion has a dominant periodic component. However, the pseudo-phase spaces of points A, B and D look like a cloud of points which shows the oscillations corresponding to these points are erratic, thus, suggesting a strong chaotic component.

2.6.2.5 PDF

It is impossible to predict the time history of a chaotic motion because a small change in the initial conditions will alter the response of the system. Thus, one may take advantage of the probability density function, PDF, to have a statistical measure of the dynamics of the system. The PDF of a periodic signal consists of two dominant peaks at the extremes of the displacement, where the probability of finding the oscillating system is high, because motion is slow. For example, look at the PDFs of points C and E in Figures 2-14(f) and 2-16(f), respectively, which signify that the oscillations at these two flow velocities have a strong periodic component. Deviation from this double-masted shape towards normal (Gaussian) distribution demonstrates irregularity of oscillation. According to Figures 2-12(f), 2-13(f) and 2-15(f), which represent the PDFs of points A, B and D, respectively, the oscillations at these flow velocities are erratic and chaotic since their PDFs show a departure from the double-masted shape and the space in between the two peaks is filled to some extent.

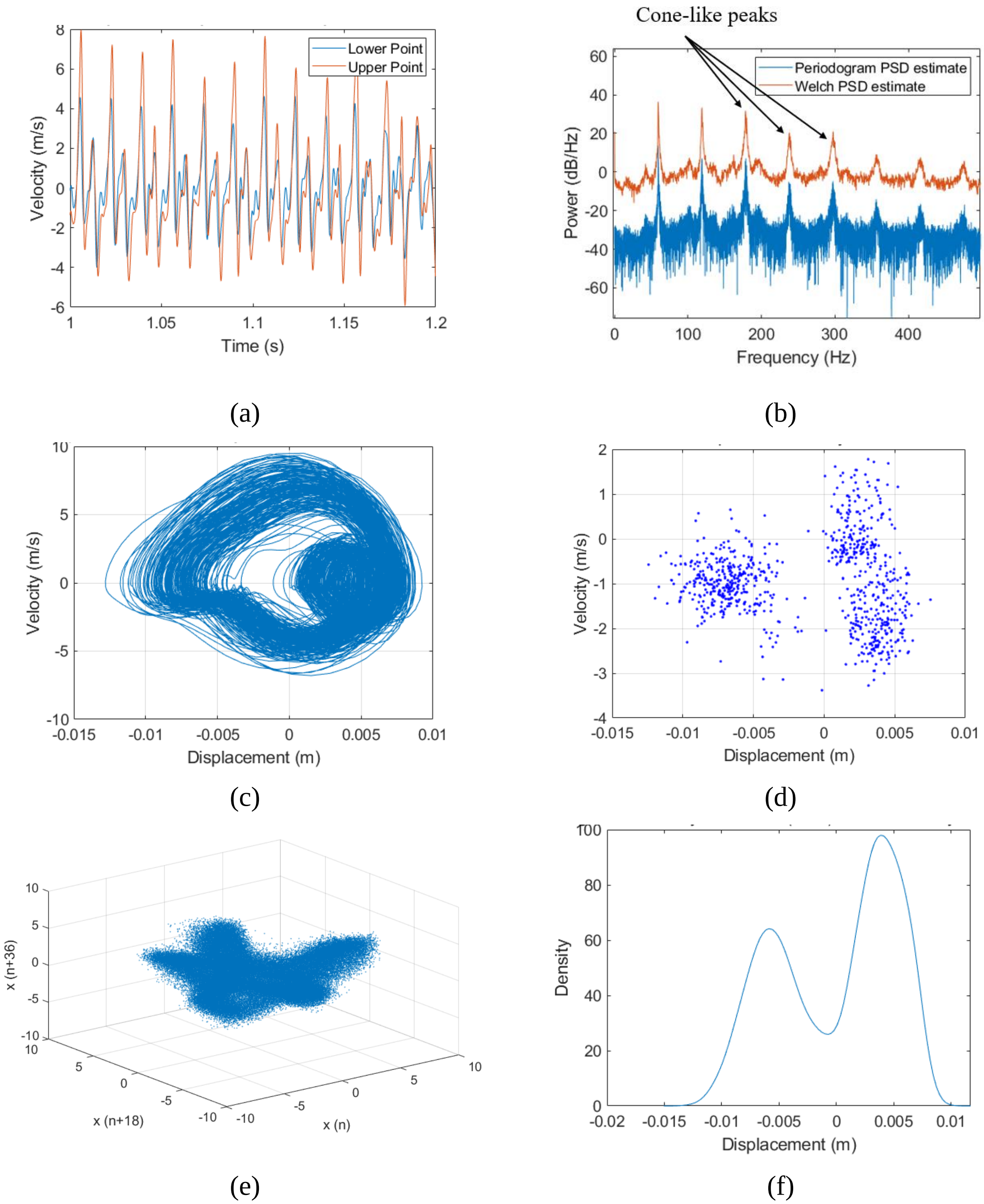

Figure 2-12. Detailed results for point A with V = 25.6 m/s: (a) time history of the velocity signal; (b) power spectral density (PSD); (c) phase portrait; (d) displacement-triggered Poincaré map; (e) reconstructed phase space; (f) probability density function (PDF).

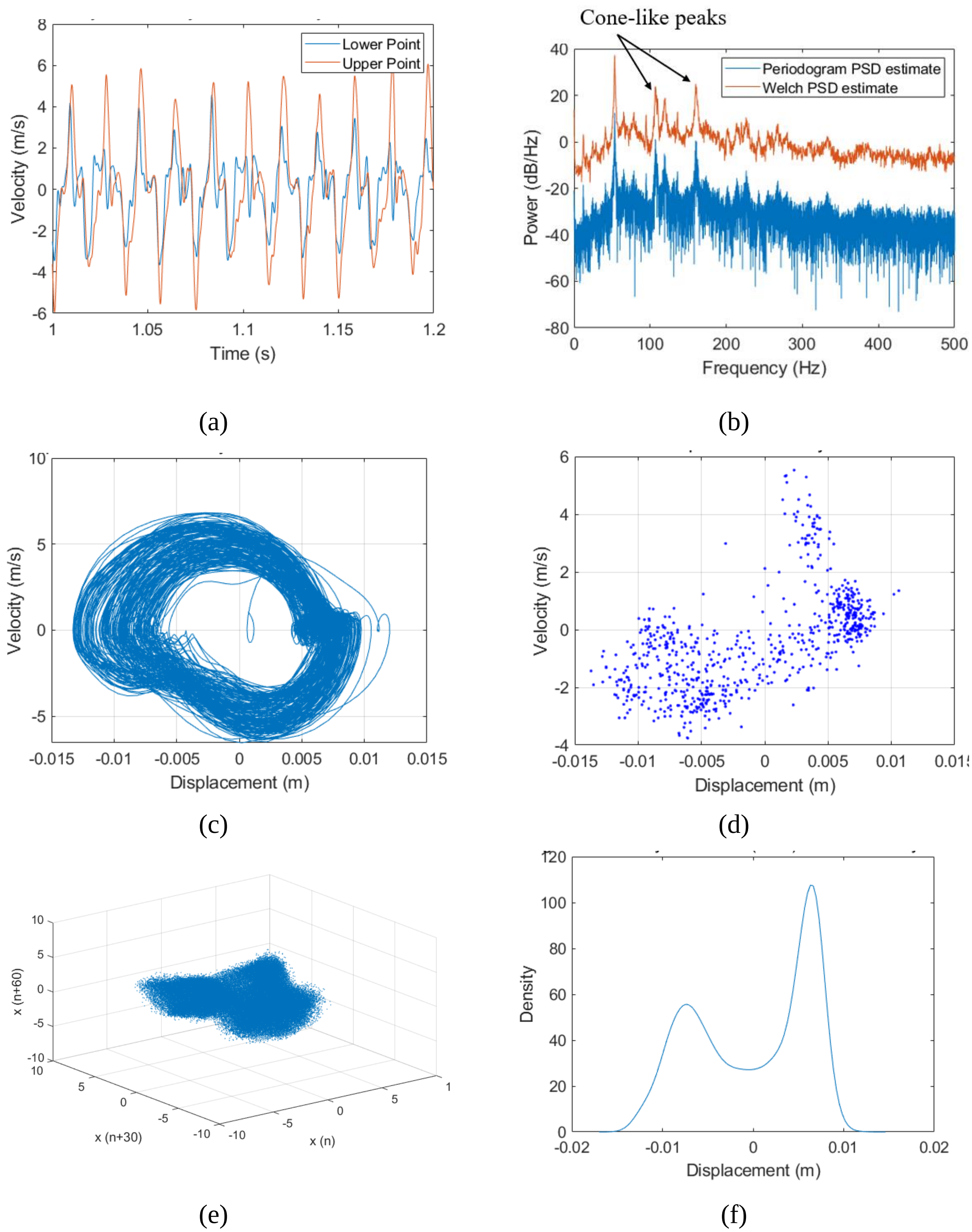

Figure 2-13. Detailed results for point B with V = 21.6 m/s: (a) time history of the velocity signal; (b) power spectral density (PSD); (c) phase portrait; (d) displacement-triggered Poincaré map; (e) reconstructed phase space; (f) probability density function (PDF).

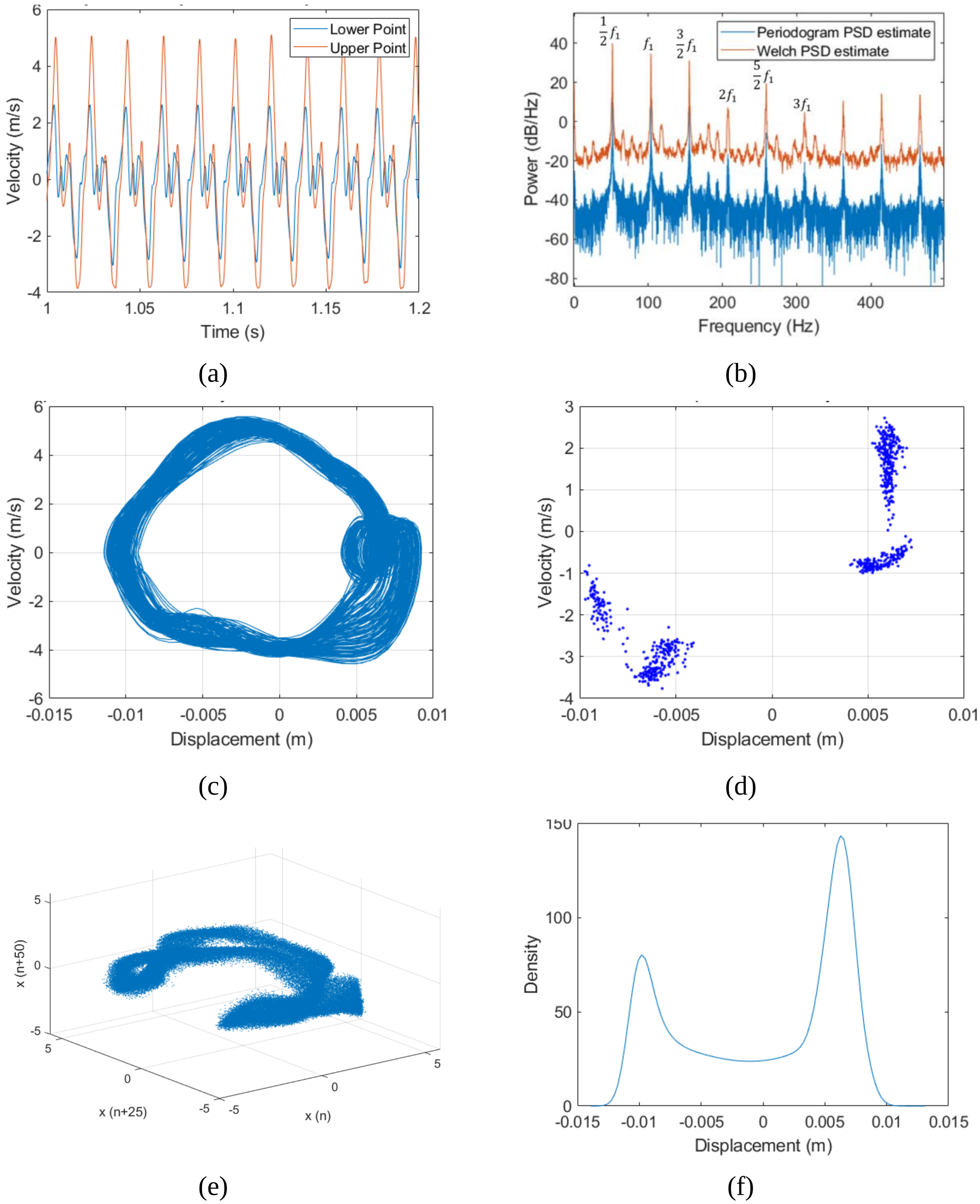

Figure 2-14. Detailed results for point C with V = 19.4 m/s: (a) time history of the velocity signal; (b) power spectral density (PSD); (c) phase portrait; (d) displacement-triggered Poincaré map; (e) reconstructed phase space; (f) probability density function (PDF).

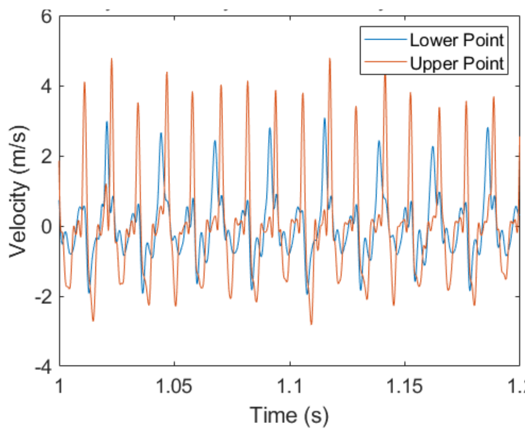

(a)

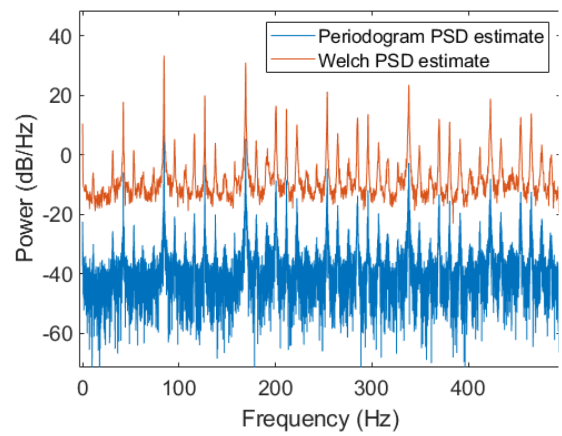

(b)

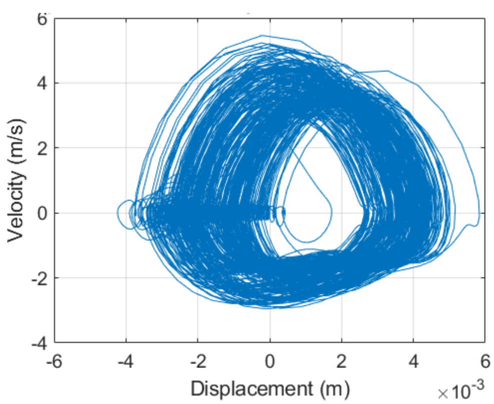

(c)

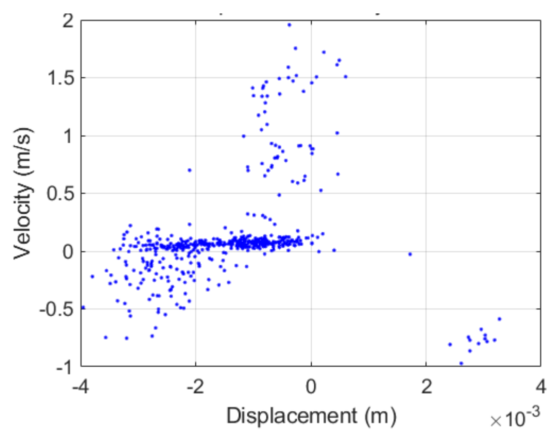

(d)

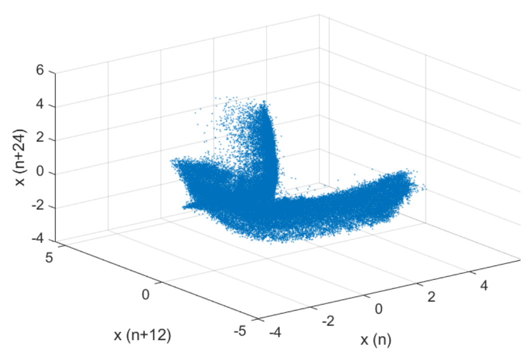

(e)

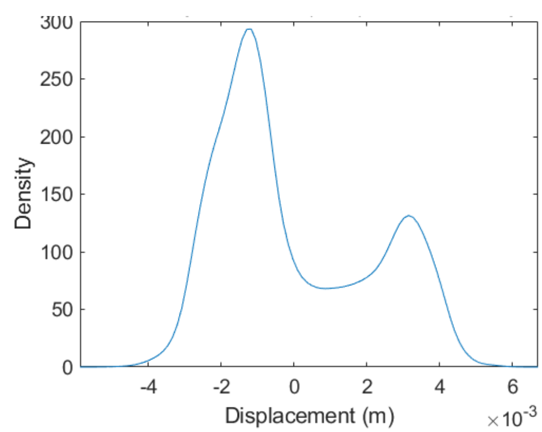

(f)

Figure 2-15. Detailed results for point D with V = 17.4 m/s: (a) time history of the velocity signal; (b) power spectral density (PSD); (c) phase portrait; (d) displacement-triggered Poincaré map; (e) reconstructed phase space; (f) probability density function (PDF).

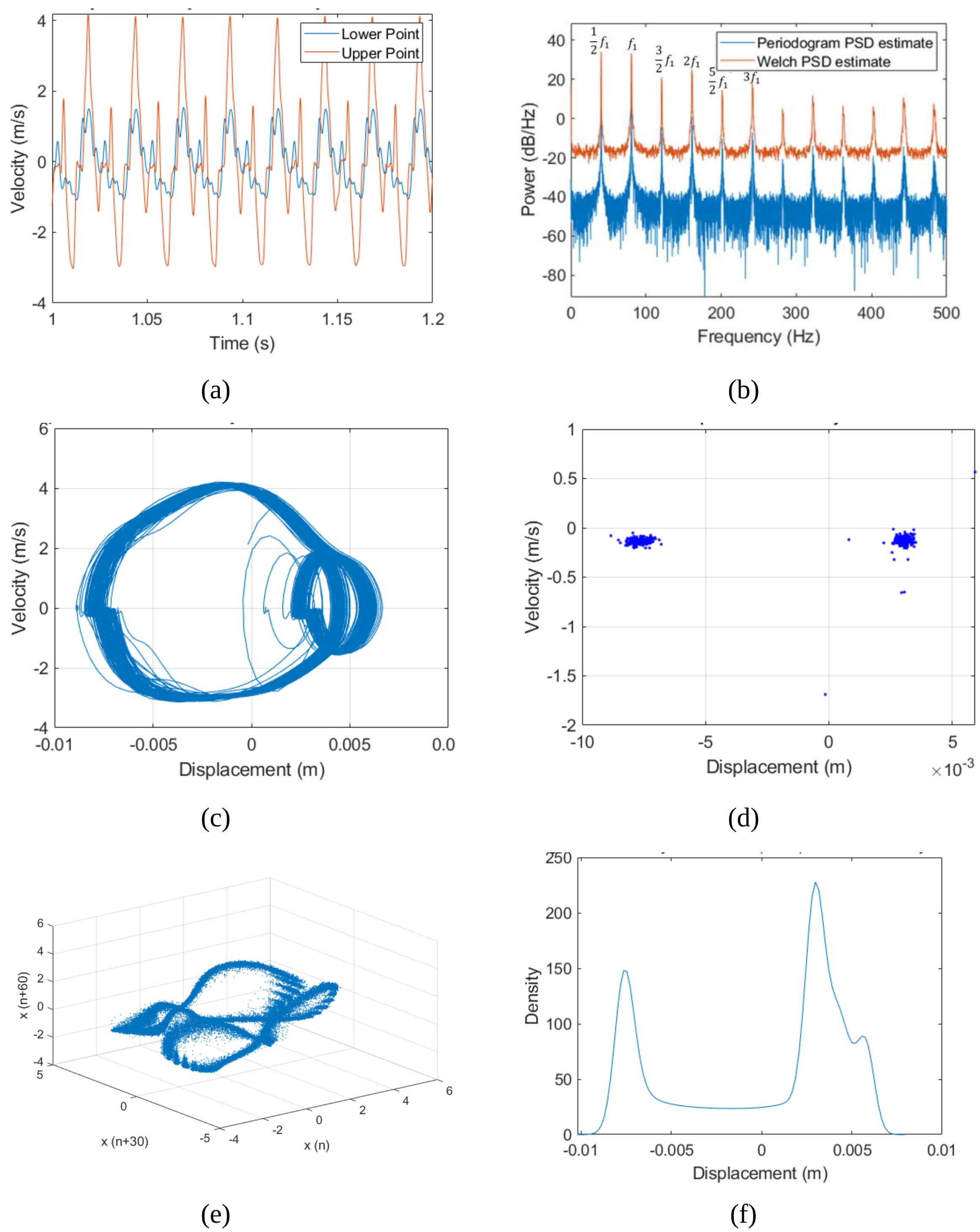

Figure 2-16. Detailed results for point E with V = 16.4 m/s: (a) time history of the velocity signal; (b) power spectral density (PSD); (c) phase portrait; (d) displacement-triggered Poincaré map; (e) reconstructed phase space; (f) probability density function (PDF).

2.6.2.6 Autocorrelation of points A and C

The autocorrelation, by definition, is the correlation of a signal with a delayed copy of itself as a function of delay. The autocorrelation of a periodic signal is periodic with time, while a chaotic (aperiodic) signal has a damped response with time. In this section, the autocorrelation of oscillations corresponding to only points A and C are presented for the sake of brevity. In agreement with results presented in Figures 2-12 (point A) and 2-14 (point C), the autocorrelation associated with point A dies out very quickly, showing loss of memory after a few cycles of motion, while that of point C demonstrates a statistical similarity between delayed versions of oscillations (Figure 2-17).

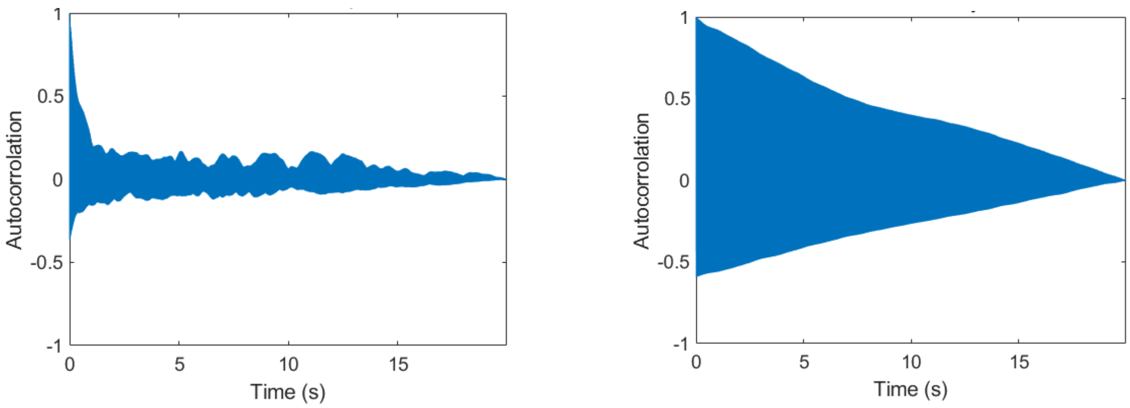

(a) (b)

Figure 2-17. Autocorrelation of the signal corresponding to (a) point A; (b) point C. Flow velocities corresponding to points A and C are presented in Table 2-1.

2.6.3 Summary

To sum up, points C and E, as shown in Figures 2-14 and 2-16, respectively, display a weak chaotic behaviour, yet with a strong periodic component. This behaviour is referred to as 'limited' or 'narrow-band' chaos in the literature [28]. Narrow-band chaotic vibration has similar orbits in the phase space as those of periodic motion (closed curves). Besides, the power spectra demonstrate a set of narrow spikes (not a fully continuous spectrum) which are commensurable (subharmonics or superharmonics of the fundamental frequency). Nevertheless, points A , B and D, as shown in Figures 2-12, 2-13 and 2-15, respectively, exhibit a stronger chaotic behaviour having broad-band spectra, scattered pseudo-phase spaces and Poincaré maps with nonsmooth fractal basin boundaries, and PDFs which do not look perfectly double-masted. This dynamical behaviour is often referred to as 'large-scale' or 'broad-band' chaos. The time traces corresponding to points C and E, Figures 2-14(a) and 2-16(a), respectively, show a clean repetitive pattern which looks like the superposition of sinusoids. However, the time histories of points A, B and D (Figures 2-12(a), 2-13(a) and 2-15(a), respectively) exhibit irregularity with complex patterns which do not seem similar in different cycles.

The quantitative and qualitative measures associated with each of the data points, Figures 2-12 - 2-16, are in agreement with the prediction of the largest Lyapunov exponent and wavelet analysis, Figures 2-10 and 2-11. A summary of the strength of the chaotic component at different flow velocities is presented in Table 2-2.

Table 2-2. The strength of the chaotic component at different flow velocities, ***: strong chaotic component; **: moderate chaotic component, *: weak chaotic component.

Point	PSD	Phase portrait	Poincaré map	Pseudo-phase space	PDF
A	***	***	***	***	***
B	***	***	***	***	**
C	*	*	*	*	*
D	**	***	**	**	**
E	*	*	*	*	*

2.7 Experiments on a shell pressurized from outside

As mentioned earlier, the pressure in the annulus is equalized to the mean internal pressure by two small holes (D_h= 3 mm), one at upstream and the other downstream of the tested shell (see Figure 2-3). The results presented in Sections 2.5 and 2.6 are based on these two holes being open. However, it was thought interesting to see what happens when the upper hole is blocked and thus having only one hole open at the bottom clamp. Interestingly, it was observed that oscillations ended in static buckling after about 5 s of oscillatory motions. The reason is that, in this case, there is an increase of the pressure in the annulus, which forces the shell to stop oscillating and to become subject to buckling by external pressure (combined to internal flow, which reduces the shell stiffness). As shown in Table 2-3, by increasing the flow velocity, the final annular pressure, P_{ann}, increases. In addition, the photographs taken from the top of the shell show that the internal area at the buckled cross-section decreases with increasing flow velocity, as seen in Figure 2-18. It should be clarified that for the configuration with only 1 hole open, the critical flow velocity associated with disturbance-induced instability equals 15.6 m/s, which is much lower than that of configuration with the two holes open, namely 24.9 m/s. This is because the static pressure at the upstream (lower) clamp is higher than that at the downstream (upper) clamp. Thus, the annular pressure is also higher in this configuration, precipitating instability at lower flow velocities.

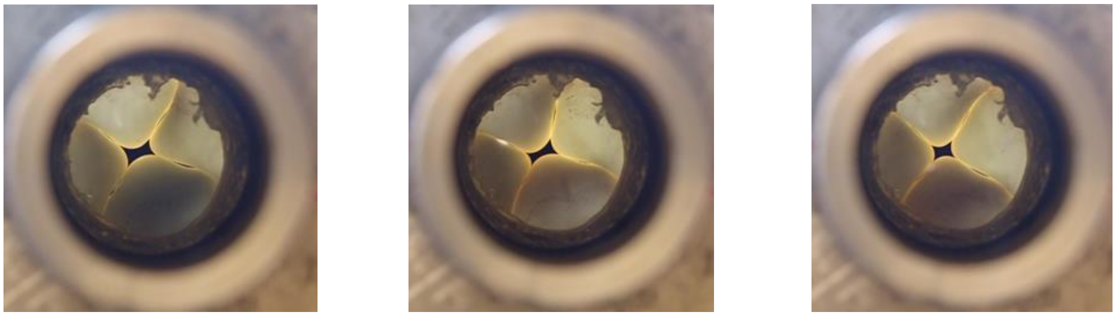

(a) (b) (c)

Figure 2-18. Photos taken from the top of the shell for configuration with only 1 hole at the lower clamp when the shell has ended in static buckling after a transient period of oscillatory motions. The corresponding flow velocities are presented in Table 2-3.

Table 2-3. Effect of flow velocity on internal area and annulus pressure for the configuration with only one hole open at the lower clamp. Internal areas are obtained by binarizing the photograph; then, calculating the ratio of black cells over the total number of cells.

Corresponding photo in Figure 2-18	(a)	(b)	(c)
V (m/s)	15.6	17.9	20.2
P_{ann}(kPa)	17.9	20.6	22.0
Flow area at the throat (mm^2)	27.5	21.4	19.4

2.8 Conclusions

This study is an attempt to gain a more in-depth understanding of the dynamic divergence phenomenon in shells with supported ends conveying air flow. The mechanism of dynamic divergence was explored first by taking high-resolution photos using a high-speed camera. These photos showed that the dynamic divergence evolves in three phases through time. The first two phases, which last about 100 ms in total, are regular oscillations with well-defined mode shapes. With the passage of time, oscillations become complex in what has been named phase 3. In this phase, opposing walls start to impact on each other violently and close the shell for half of the period of each cycle, thus fully obstructing the airflow. This gives rise to a build-up in pressure upstream of the blocked cross-section (throat), leading to a ‘bubble-travelling’ mechanism. The photo of the first cycle of oscillation, taken from the top of the shell, shows that, due to the high flexibility of the shell, airflow is obstructed considerably, such that the flow is not only compressible, but also chocked at the throat, even in the first cycle of oscillations in which blockage is minimum, compared to subsequent cycles. More qualitative and quantitative characteristics of dynamic divergence were investigated by means of several measures such as PSDs, phase portraits, pseudo-phase space reconstructions, Poincaré maps, PDFs, wavelet transforms, the largest Lyapunov exponents and autocorrelations. All these techniques confirmed that the system behaviour is greatly dependent on flow velocity. Although the general trend suggests that the chaotic characteristics of the oscillations are attenuated by decreasing flow velocity, the motions reexhibit strong irregularity and unpredictability for specific ranges of the decreasing flow velocity.

The experimental observations and their subsequent analysis in this paper are for a specific shell with given length-to-radius ratio, *L/R* and thickness-to-radius ratio, *h/R*, and material properties. However, the dynamical behaviour of other shells with the same or different *L/R* and *h/R* ratios is broadly similar, yet with some interesting differences, discussion of which is beyond the scope of this paper.

2.9 References

1. E. Naudascher, D. Rockwell, Oscillator-model approach to the identification and assessment of flow-induced vibrations in a system, J. Hydraul. Res. 18 (1980) 59–82.

2. E. Naudascher, D. Rockwell, Flow-Induced Vibrations: An Engineering Guide, AA Balkema, Rotterdam, 1994.

3. E.H. Dowell, Aeroelasticity of Plates and Shells, Noordhoff International Publishing, Leyden, 1975.

4. E.H. Dowell, A Modern Course in Aeroelasticity, Fifth Revised and Enlarged Edition, Springer, Dordrecht, 2015.

5. M.P. Païdoussis, Fluid-Structure Interactions: Slender Structures and Axial Flow: Vol. 1, Second Edition, Academic Press, Oxford, 2014.

6. M.P. Païdoussis, J.-P. Denise, Flutter of thin cylindrical shells conveying fluid, J. Sound Vib. 20 (1972) 9–26.

7. M.P. Païdoussis, Fluid-Structure Interactions: Slender Structures and Axial Flow: Vol. 2, Second Edition, Academic Press, Oxford, 2014.

8. G.T.S. Done, A. Simpson, Dynamic instability of certain conservative and non-conservative systems., J Mech Eng Sci. 19 (1977) 251–263. \

9. M.P. Païdoussis, Some unresolved issues in fluid-structure interactions, J. Fluids Struct. 20 (2005) 871–890.

10. D.S. Weaver, T.E. Unny, On the dynamic stability of fluid-conveying pipes, J. Appl. Mech. 40 (1973) 48–52.

11. M.P. Païdoussis, S.P. Chan, A.K. Misra, Dynamics and stability of coaxial cylindrical shells containing flowing fluid, J. Sound Vib. 97 (1984) 201–235.

12. A. El Chebair, M.P. Païdoussis, A.K. Misra, Experimental study of annular-flow-induced instabilities of cylindrical shells, J. Fluids Struct. 3 (1989) 349–364.

13. M. Amabili, M.P. Païdoussis, Review of studies on geometrically nonlinear vibrations and dynamics of circular cylindrical shells and panels, with and without fluid-structure interaction, Appl. Mech. Rev. 56 (2003) 349–356.

14. M. Amabili, Nonlinear Vibrations and Stability of Shells and Plates, Cambridge University

Press, 2008.

15. F. Alijani, M. Amabili, Non-linear vibrations of shells: A literature review from 2003 to 2013, Int. J. Non. Linear. Mech. 58 (2014) 233–257.

16. M. Amabili, F. Pellicano, M.P. Païdoussis, Nonlinear stability of circular cylindrical shells in annular and unbounded axial flow, J. Appl. Mech. 68 (2001) 827–834.

17. M. Amabili, F. Pellicano, M.P. Païdoussis, Non-linear dynamics and stability of circular cylindrical shells containing flowing fluid. Part IV: Large-amplitude vibrations with flow, J. Sound Vib. 237 (2000) 641–666.

18. M. Amabili, R. Garziera, Vibrations of circular cylindrical shells with nonuniform constraints, elastic bed and added mass. Part II: Shells containing or immersed in axial flow., J. Fluids Struct. 16 (2002) 31–51.

19. M. Amabili, R. Garziera, Vibrations of circular cylindrical shells with nonuniform constraints, elastic bed and added mass. Part III: Steady viscous effects on shells conveying fluid., J. Fluids Struct. 16 (2002) 795–809.

20. M. Amabili, F. Pellicano, M.P. Païdoussis, Non-linear dynamics and stability of circular cylindrical shells containing flowing fluid. Part I: stability, J. Sound Vib. 225 (1999) 655–699.

21. M. Amabili, K. Karagiozis, M.P. Païdoussis, Effect of geometric imperfections on non-linear stability of circular cylindrical shells conveying fluid, Int. J. Non. Linear. Mech. 44 (2009) 276–289.

22. K.N. Karagiozis, M.P. Païdoussis, M. Amabili, A.K. Misra, Nonlinear stability of cylindrical shells subjected to axial flow: Theory and experiments, J. Sound Vib. 309 (2008) 637–676.

23. P. Balasubramanian, G. Ferrari, M. Amabili, Nonlinear vibrations of a fluid-filled, soft circular shell: experiments and system identification, Nonlinear Dyn. 102 (2020) 1409–1418.

24. S. Mallat, A Wavelet Tour of Signal Processing: The Sparse Way, Second Edition, Academic Press, Burlington, 2009.

25. F.C. Moon, Chaotic Vibrations, Wiley-Interscience, New York, 2004.

26. T. Smelova-Reynolds, E.H. Dowell, The role of higher modes in the chaotic motion of the buckled beam—I, Int. J. Non. Linear. Mech. 31 (1996) 931–939.

27. D. Xie, M. Xu, H. Dai, E.H. Dowell, Observation and evolution of chaos for a cantilever plate in supersonic flow, J. Fluids Struct. 50 (2014) 271–291.

28. F.C. Moon, Chaotic and Fractal Dynamics: Introduction for Applied Scientists and Engineers, John Wiley & Sons, New York, 2008.

29. M.P. Païdoussis, F.C. Moon, Nonlinear and chaotic fluidelastic vibrations of a flexible pipe conveying fluid, J. Fluids Struct. 2 (1988) 567–591.

30. A. Wolf, J.B. Swift, H.L. Swinney, J.A. Vastano, Determining Lyapunov exponents from a time series, Phys. D Nonlinear Phenom. 16 (1985) 285–317.

31. M. Amabili, P. Balasubramanian, G. Ferrari, Travelling wave and non-stationary response in nonlinear vibrations of water-filled circular cylindrical shells: Experiments and simulations, J. Sound Vib. 381 (2016) 220–245.

32. B. Malraison, P. Atten, P. Bergé, M. Dubois, Dimension of strange attractors: an experimental determination for the chaotic regime of two convective systems, J. Phys. Lett. 44 (1983) 897–902.

2.10 Appendix A: Material properties of the shell

The material properties and geometry of the silicone rubber shell used in the experiments are reported in Table 2-4, where R is the internal radius of the shell, h its thickness, and L its length. Thus, L/R = 6 and h/R = 0.05. E is the Young's modulus, and ν the Poisson's ratio.

Table 2-4. The material properties and geometry of the silicone rubber shell.

L (mm)	R (mm)	h (mm)	E (MPa)	ρ_s (kg/m^3)	ν
149.02	24.84	1.38	1.53	1.05×10^3	0.49

Silastic E-RTV is an elastomer (silicone rubber) material exhibiting viscoelastic characteristics such as time-dependent strain. A tensile test was performed on a long narrow strip of silastic (width=10.02 mm, thickness=1.38 mm, length=34.64 mm) with the strain rate of $1.4 \times 10^{-2}\ \mathrm{s}^{-1}$, cast from the same batch of the test shell, to obtain the stress-strain diagram, Figure 2-19. The Young's modulus is identified as the tangent to the origin and is 1.53 MPa, as given in Table 2-4.

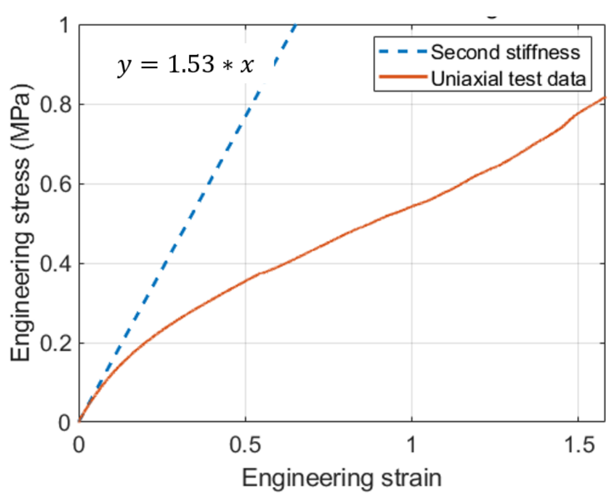

Figure 2-19. Silastic E-RTV stress-strain diagram.

The mass density was measured by weighing a cube of silastic (from the same batch as the cast shell) in air and in water at room temperature. It is noted that silastic is denser than water and does not float. A digital scale with a resolution of 1/100 grams was employed. The weight in air, W_s, was measured simply by weighing the cube. To measure the weight in water, a beaker containing some water was firstly put on the scale and the scale was set to zero. Then, the silastic cube was submerged in water using a very thin thread and the value indicated by the scale was recorded, which is equal to the buoyancy force, F_b, acting on the suspended cube,

$$F_b = \rho_w g V_s, \tag{A.1}$$

where ρ_w is the mass density of water, g is the gravitational constant and, V_s is the volume of water displaced by the immersed cube, which is equal to the volume of the completely immersed silastic cube. Replacing ρ_w by the ratio F_b / gV_s, obtained from Eq. (A.1), the specific gravity of silastic with respect to water, SG, is calculated:

$$SG = \frac{\rho_s}{\rho_w} = \frac{\rho_s}{F_b / gV_s} = \frac{\rho_s g V_s}{F_b} = \frac{W_s}{F_b}. \tag{A.2}$$

Assuming the mass density of the water to be 1.000 g/cm^3 at 20° C, and knowing the buoyancy force in water, F_b, one can obtain the mass density, ρ_s. The results of the mass density measurement are presented in Table 2-5.

Table 2-5. The measurements of weight and buoyant force used to calculate density of silastic E-RTV.

W_s (g)	F_b (g)	ρ_s (g/cm^3)
12.79	12.15	1.05

2.11 Appendix B: Flow compressibility study

The following calculations have been done for the first cycle of oscillations at V= 24.3 m/s to determine whether the flow is compressible at the shell throat or not. Flow obstruction in the first cycle of oscillations is minimum compared to that in subsequent cycles. The flow is assumed to be isentropic (constant stagnation pressure) because the Reynolds number is quite large ($Re = 7.71 \times 10^4$) and viscous effects are negligible.

Firstly, the internal area of the shell at the lower clamp (upstream of the throat), A_u in Figure 2-3, equals

$$A_u = \frac{\pi D^2}{4} = \frac{\pi \times 48.5^2}{4} = 1847.4 \text{ mm}^2. \tag{B.1}$$

By binarizing the photo of the first cycle of oscillations, Figure 2-20, the ratio of upstream (undeformed) internal area, A_u, over the throat area at the buckled cross-section, A_t in Figure 2-3, is determined to be equal to 9.1. Thus, the throat area is

$$\frac{A_u}{A_t} = 9.1 \rightarrow A_t = 203.0 \text{ mm}^2. \tag{B.2}$$

Air temperature, T, is assumed to be constant and equal to 293.15 K. Specific gas constant for dry air, R, is assumed equal to 287 J/kg K. The density of air, ρ_u, is obtained from the measurement of the static pressure upstream of the throat, which is equal to $P_u = 104.4$ kPa; thus,

$$\rho_u = \frac{P_u}{RT} = \frac{104.4 \times 10^3}{287 \times 293.15} = 1.2 \frac{\text{kg}}{\text{m}^3}. \tag{B.3}$$

The Mach number upstream of the throat (lower clamp) is obtained from the measured mass flow rate, $\dot{m}$, equal to 0.053 kg/s:

$$M_u = \frac{\dot{m} / \rho A}{\sqrt{\gamma RT}} = \frac{0.053 / [1.2 \times (1847.4 \times 10^{-6})]}{\sqrt{1.4 \times 287 \times 293}} = 0.070 \xrightarrow{\text{Isentropicc flow table}} \frac{A_u}{A^*} = 8.3, \tag{B.4}$$

thus, one can calculate the chocked throat area, A^*, equal to

$$\frac{A_u}{A^*} = 8.3 \xrightarrow{A_u = 1847.4 \text{ mm}^2} A^* = 222.6 \text{ mm}^2, \tag{B.5}$$

where A^* is the sonic area; the flow will become sonic when the throat is closed to that area. With further decrease in the flow area, the throat will remain sonic while the mass flow rate will decrease and eventually become zero when the throat is closed completely. The inflow Mach number will decrease in this case (eventually to zero) and the pressure will increase (eventually to the stagnation value). Now, by having A^*, the Mach number at throat, M_t, is

$$\frac{A_t}{A^*} = \frac{203.0}{222.6} = 0.9 \xrightarrow{\text{Choked throat}} M_t = 1, \tag{B.6}$$

which indicates that when the shell collapses inward in the first cycle of oscillations, the flow is not only compressible, but also choked at the throat.

What happens downstream of the throat when the throat is choked depends on the difference between the upstream (inlet) stagnation pressure and the downstream (outlet) pressure (back pressure). The flow may become locally supersonic with a weak normal shock.

What happens when the shell starts to reopen after the fully-closed stage, depends on the flow characteristic time which is the time needed for a disturbance to propagate through the entire length of the flow. If the reopening process is slow enough, then a steady flow with choked throat will be established soon enough and then everything will go in reverse manner (as compared to the closing stage). If the opening is very fast, then the initial flow will more resemble a shock-tube flow with a weak shock propagating to the right and an expansion wave to the left. The former is the case here, because the following calculations show that the flow can be considered as pseudo-steady (i.e., as a sequence of steady states). The flow characteristic time is:

$$t = \frac{L}{c} = \frac{L}{\sqrt{\gamma RT}} = \frac{149.02}{343.1} = 0.43 \text{ s,} \tag{B.7}$$

while it takes about 2 ms for the shell to become completely closed from the reopened stage (closing time). Thus, the flow characteristic time is about 5 times less than the closing time; hence, the flow will have enough time to adjust to the changing geometry and it is possible to employ pseudo-steady relations as an approximation.

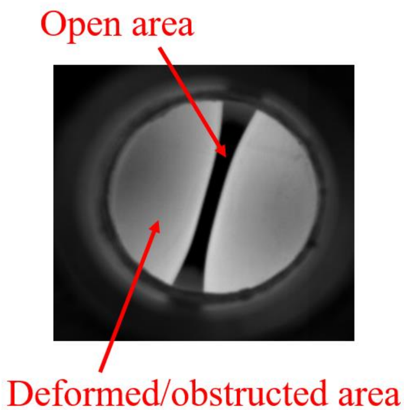

Figure 2-20. Photograph from the top of the shell showing the maximum deformation in the first cycle of oscillations at V=24.3 m/s (t = 38.5 ms in Figure 2-4).

2.12 Link between Chapter 2 and 3

The experimental observations and their subsequent analysis in Chapter 2 are for a specific shell with given length-to-radius ratio, L/R=6, and thickness-to-radius ratio, h/R=0.05, and material properties. The question naturally arises whether the observations described in Chapter 2 are unique to that specific shell, or if they are more general, applying to longer or thicker shells, for example. Answering this question is the main objective of Chapter 3. It is shown that the dynamical behaviour of other shells with the same or different L/R and h/R ratios is broadly similar, yet with some interesting differences, discussion of which is presented in this chapter.

Besides, the results presented in Chapter 2 have been obtained for the configuration with a rigid (plexiglas) outer tube and two small holes (D_h= 3 mm), one upstream and the other downstream of the tested shell to equalize the pressure in the annulus to the mean internal pressure. However, it was thought interesting to investigate the influence of confinement, as a result of the presence of the plexiglas tube, on the dynamics of the system, by comparing the oscillations with and without confinement. This is examined in Chapter 3.

3 Parametric study on dynamic divergence

Experimental parametric study on dynamic divergence instability and chaos of circular cylindrical shells conveying airflow

Iman Gholami, Marco Amabili, Michael P. Païdoussis*

Department of Mechanical Engineering, McGill University, 817 Sherbrooke Street West, Montréal Québec, Canada, H3A 0C3

* Corresponding author.Michael.paidoussis@mcgill.ca (M. P. Païdoussis)

3.1 Abstract

Experiments have shown that soft circular cylindrical shells supported at both ends and conveying airflow lose stability by so-called *dynamic divergence*. The present study investigates experimentally the effect of geometric parameters of the silicone rubber shell, namely length-to-radius (L/R) and thickness-to-radius (h/R) ratios, on the dynamic divergence instability. Bifurcation diagrams of the rms velocity of the shell vibration versus flow velocity are obtained for different shells, showing a strongly subcritical nonlinear behaviour. Then, the onset of instability and post-critical behaviour of the shells are compared: (i) thinner and longer shells lose stability at lower flow velocities, (ii) thinner shells have higher rms vibration velocity, and (iii) by decreasing L/R, the subcritical behaviour is weakened for thin shells, while it is strengthened for thick shells. The existence of chaos and the influence of geometric parameters on the chaotic behaviour of the system is deeply examined by means of several measures.

3.2 Introduction

Flow-induced vibrations can be classified in several ways [1]. A very systematic classification is presented by Naudascher and Rockwell [2,3], according to which, flow-induced vibrations are categorized into three groups, based on the source of excitation: (i) extraneously-induced excitation (EIE), (ii) instability-induced excitation (IIE), and (iii) movement-induced excitation (MIE), also known as self-excited oscillations, the latter of which applies to the system considered in this study. Self-excited oscillations are oscillatory motions due to the movement of the structure, meaning that there is no external excitation to the system; in other words, there is no oscillatory excitation in the absence of motion. The flutter of aircraft wings [4,5] and of a cantilevered pipe subjected to internal or external axial flow [6,7,8] , are examples of self-excited vibrations, to name just a few.

In 1969, in a set of experiments with cantilevered and clamped-clamped elastomer shells conveying airflow, the shells developed vigorous flutter in the second or third circumferential mode number (n=2 or 3) at rather low flow velocities [9,10]. This was unexpected at that time and stimulated further interest in research on this subject.

The occurrence of flutter for the clamped-clamped shells (i.e., shells with both ends clamped) subjected to internal airflow was perplexing, as this is an inherently conservative system, and therefore ought to be immune to oscillatory instability. In the linear analytical model of Païdoussis and Denise [10], the system loses stability by static divergence, as expected; but at a slightly higher flow velocity, the Païdoussis-type [11] coupled-mode flutter appears. Similar results for simply-supported circular cylindrical shells are predicted by linear theory [12]: loss of stability by static divergence first, and then flutter at higher flow velocities. At the time, because of the closeness of the critical flow velocities for the two phenomena, it was reasoned that the divergence entrained the observed flutter directly, so that the experimental divergence could not be observed on its own.

Clamped-clamped coaxial circular cylindrical shells containing internal and/or annular fluid flow were studied theoretically in [13], by means of linear theory. Shells conveying internal flow were shown to lose stability at higher flow velocities compared to those with annular flow. The effect of compressibility of the flow was also examined, showing little influence on the stability of the system. Experiments with clamped-clamped and cantilevered shells subjected to annular flow were conducted in [14], showing loss of stability by flutter or static divergence for cantilevered and clamped-clamped shells, respectively.

It was considerably later (in 2005) that, based on experiments with clamped-clamped Polyethylene Terephthalate (PET) and aluminium shells conveying water, it was concluded that the observed ‘flutter’ was in fact a manifestation of *dynamic divergence* [15,16]– the mechanism of which will be explained below. Dynamic divergence and some other paradoxical phenomena in fluid-structure interaction are briefly discussed in [17].

Amabili et al. [18] investigated theoretically the nonlinear dynamics and stability of simply-supported circular cylindrical shells conveying inviscid incompressible fluid. Donnell’s nonlinear shallow-shell theory and linearized potential flow theory were utilized in the model. The numerical results indicated that the system loses stability by a strongly subcritical divergence. The nonlinear model was enhanced in [19] by taking into account geometric imperfections in order to study the subcritical static divergence of the shells. The results demonstrated excellent agreement with experimental results for thin aluminium shells conveying water. Karagiozis et al. [20] presented a model for clamped-clamped shells conveying internal or annular flow. Experiments with plastic or aluminium shells conveying water were also conducted for comparison with the numerical results of the model; both showed loss of stability by static divergence via a subcritical pitchfork bifurcation. The same nonlinear model as in [20] was utilized to study the effect of length-to-radius and thickness-to-radius ratios on the stability of clamped-clamped circular cylindrical shells conveying incompressible fluid [21]. Thinner and longer shells were shown to have lower natural frequencies and lose stability at lower flow velocities, compared to thicker and shorter ones, as expected. However, thicker shells could have larger post-divergence amplitudes of deformation.

Interestingly, the results for a Polyethylene Terephthalate (PET) shell with a length-to-radius ratio (*L/R*) equal to 3, indicated a supercritical bifurcation that changed to subcritical at higher flow velocities.

The nonlinear stiffness and nonlinear damping characteristics of a fluid-filled, internally-pressurized, soft PET circular cylindrical shell, were obtained experimentally in [22], by performing forced, large-amplitude (geometrically nonlinear) vibration tests. A reduced-order model was then constructed using a piecewise linear stiffness and viscous damping, showing satisfactory agreement between experimental and numerical results. The interested reader is referred to the theoretical work of Amabili and associates [23,24,25,26]. Comprehensive reviews of nonlinear vibrations of circular cylindrical shells are presented in [27,28,29].

To sum up, experiments with clamped-clamped circular cylindrical shells conveying water or subjected to annular airflow, are in agreement with theoretical predictions, i.e., loss of stability by static divergence. However, there is a paradox between the nonlinear theory and the experimental observations for clamped-clamped circular cylindrical shells conveying airflow; they have been shown to lose stability by dynamic divergence in the experiments, whereas the nonlinear theory predicts loss of stability by static divergence.

In an earlier paper [30], the dynamics of a soft (elastomer) shell with clamped ends subjected to internal airflow was studied, for a shell with L/R=6 and h/R=0.05, where L is the length, R the radius, and h the wall thickness of the shell. It was found that for sufficiently high flow velocities, the shell became subject to dynamic divergence. The shell becomes deformed (buckled) in the n=2, m=1 mode, where n is the circumferential and m the axial wave number, with amplitude large enough for the build-up of pressure behind the severely constricted flow area, roughly half-way along the shell, to force the shell to reopen, and thus collapse in the azimuthally opposite direction. This process is repeated continuously; hence the resulting oscillatory motion is referred to as a dynamic divergence. It was shown that severe flow obstruction due to the high flexibility of the shell, makes the flow locally compressible, and choked at the throat. [This is different from what was observed, for example in [19], for very thin aluminium shells, where the divergence amplitude was small compared to the shell radius, resulting in a static divergence.]

Two important features of the observed phenomenon were the following. First, with the passage of time and while the flow velocity remained constant, the n=2, m=1 form of the oscillation evolved into more complex and distorted forms. Second, when the flow velocity was reduced, the amplitude of the oscillation decreased and eventually ceased at a flow velocity named V_{rest}, considerably lower than that for the onset of the oscillation, V_{cr}, indicating a highly subcritical behaviour. Furthermore, the reduction in amplitude with decreasing flow velocity was very irregular, rather than smooth. Although displaying a dominant frequency, the oscillation also contained a chaotic component, sometimes large and sometimes small, as analyzed in [30].

The question naturally arises whether the observations described above are unique to the *L/R*=6 and *h/R*=0.05 shell studied before, or if they are more general, applying to longer or thicker pliable shells, for example. Answering this question is the main objective of this paper.

In the present paper, the apparatus and testing procedure are described in Section 3.3. The photographs of oscillations, as well as relevant discussion about the mechanism of dynamic divergence are presented in Section 3.4. Section 3.5 investigates the dynamical behaviour of the system with varying flow velocity, for a typical shell. Section 3.6 presents a parametric study on the effect of varying the length and thickness of the shell on the dynamic divergence. The chaotic behaviour of the shells with different lengths and thicknesses is explored in Section 3.7; some detailed data analysis including Power Spectral Densities (PSDs), Poincaré maps, phase portrait plots, and Probability Density Functions (PDFs) are presented in this section. The effect of confinement of the shells on the dynamic divergence instability is discussed in Section 3.8.

3.3 Apparatus and testing procedure

Figure 3-1 shows a schematic of the experimental set-up and the test-section. Compressed air is generated by a bank of interconnected compressors to about 95 psi (655 kPa), stored in the tank, and then fed into the wooden chamber. The wooden chamber has three screens and a honeycomb inside, in order to break up large turbulent eddies and obtain a uniform flow, prior to passing through the shell. The flow rate is adjusted using a diaphragm valve and a needle valve. Three pressure and one temperature sensors, as well as a flowmeter are installed on the line to generate the corresponding measurements, thus determining the flow velocity.

A Photron FASTCAM MiniWX100 high-speed camera is used to take the photos to be presented in Section 3.4 with 2000 fps. Two Polytec OFV-505 vibrometer lasers are utilized to measure the shell velocity at two target points on the shell; the 'lower' and the 'upper' measurement points are located at $\frac{1}{5}L$ and $\frac{1}{3}L$ from the bottom of the shell, respectively, where L is the length of the shell. The signal from the upper measurement point is used to obtain all the experimental results, except for the displacement-triggered Poincaré maps, for which two simultaneous measurements are needed (refer to Section 3.7.1). The signal from the vibrometer lasers are digitized by means of a data acquisition system (DAQ), with a sampling rate of 5000 samples per second. Then, the digitized signal is stored in a computer.

As seen in Figure 3-1(b), there are two 3 mm holes in the upper and lower clamps to make sure that the pressure in the annulus equals the average internal pressure, thus ensuring that a static divergence is not induced by the difference between internal and external pressure. These two holes are relatively small to minimize any airflow in the annulus. The gap between the shell and plexiglas tube is 38.5 mm. The results presented in Sections 3.5, 3.63.7 and 3.7 are based on experiments with this configuration. For a more detailed description of the experimental set-up refer to [30].

In all tests the following procedure was utilized.

1. The tank was allowed to fill up the set-up with compressed air by gradually opening the ball valve, while the airflow control valves were fully closed. Then, airflow was turned on and incremented in small steps by opening the airflow control valves. The desired flow rate was achieved by tweaking the diaphragm valve and, when necessary, the needle valve. At each flow, the quiescent air in the annulus was disturbed by deflating a balloon mounted on the plexiglas tube, Figure 3-1(b). As a result, the shell became unstable at a lower flow velocity than that occurring spontaneously; without these disturbances, the shell remained stable up to the maximum flow velocity attainable by the experimental set-up. Besides, the shell oscillations are less violent at lower flow velocities, thus allowing data recording without destroying the shell; the oscillations at high V are generally so violent that they can (and sometimes did) destroy the shell. This way, at least, data is obtained at low flow velocities before the probable shell rupture. This 'disturbance-induced critical flow velocity' is referred to as the 'critical flow velocity', V_{cr}.

2. After the onset of instability, the flow velocity was decreased quickly to the point just before the shell stopped oscillating. This flow velocity is referred to as the 'restabilization flow velocity', V_{rest}. The reason why this was done is discussed in detail in Section 3.5.

3. After waiting for ~20 s to make sure that the flow is steady, the shell velocity was recorded for 10 s, during which the flow velocity was kept constant.

4. The flow velocity was incremented to a slightly higher value without stopping the shell from oscillating. After a period of about 20 s with the flow velocity constant, the shell velocity was again recorded for 10 s at the next flow velocity.

5. This procedure was repeated for increasing flow velocities up to the critical flow velocity, V_{cr}.

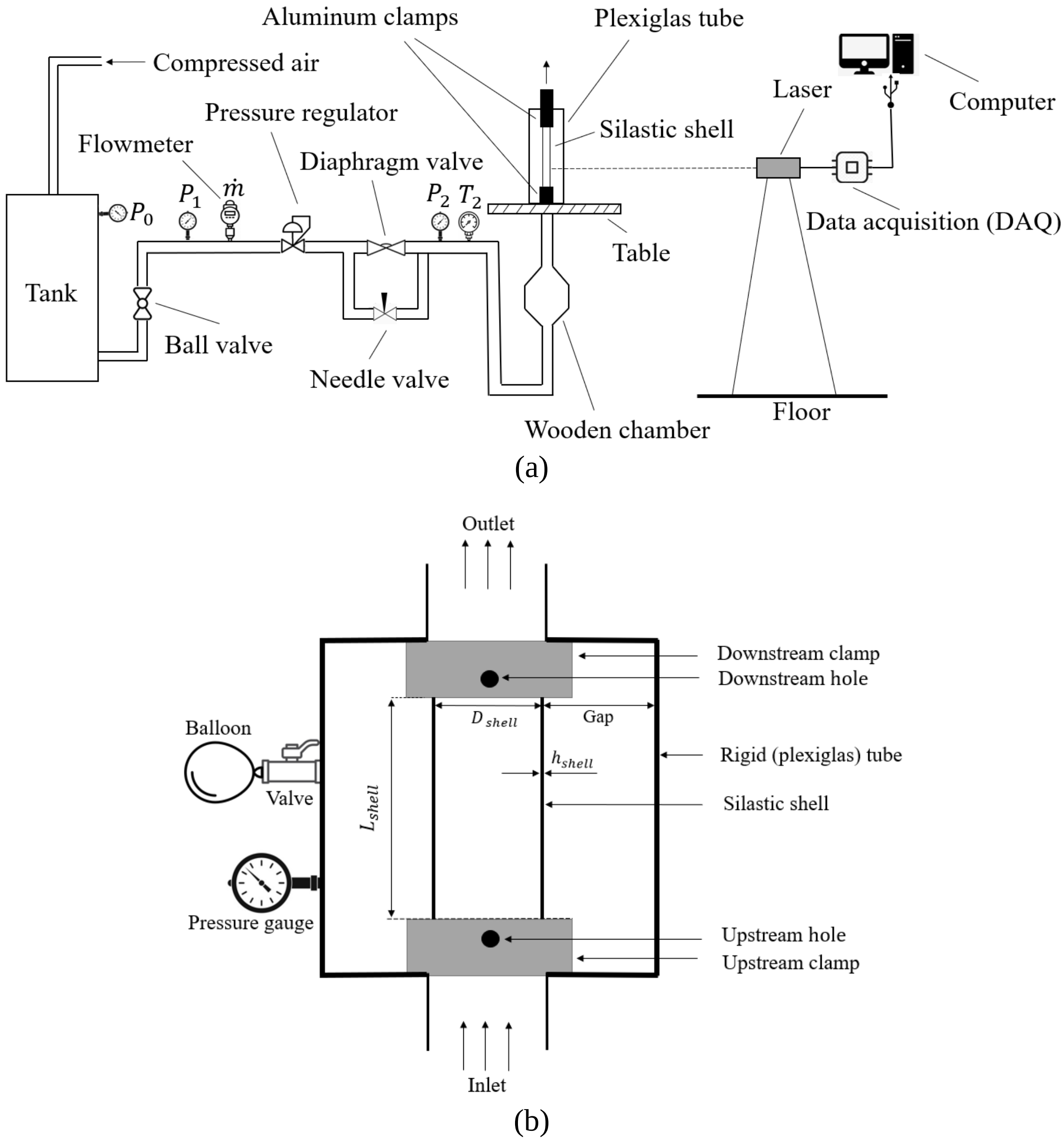

Figure 3-1. Schematic of the (a) experimental set-up [30]; (b) test-section with the tested shell. Pressure and temperature gauges are indicated by P_0, P_1, P_2 and T_2.

The experiments were conducted with circular cylindrical elastomer shells made of silicone rubber (silastic E-RTV). The material properties and geometry of the shells are listed in Table 3-1; R is the internal radius of the shell, h its thickness, and L its length. E is the Young's modulus, ν the Poisson ratio, and ρ_s the density of the shells.

Table 3-1. The material properties and geometry of the silicone rubber shells.

E (MPa)	ρ_s (kg/m^3)	ν	R (mm)	L/R	h/R
1.53	1.05×10^3	0.49	24.84	2, 4.5, 5.5, 6	0.05, 0.09

Young's modulus, E, of the shell was determined experimentally by means of a tensile test. The material density, ρ_s, was obtained by measuring the buoyancy force exerted on a cube of silastic (of known weight) when submerged in water. For a detailed description of how E and ρ_s were determined, refer to [30].

3.4 Mechanism of the dynamic divergence instability

The photographs in Figures 3-2 and 3-3 are taken with the high-speed camera from above and the front of the shell, respectively, at the critical flow velocity, V_{cr}. At the onset of instability, a divergence with longitudinal wave number m=1 and circumferential wave number n=2 or 3, depending on the length of the shell, was observed. This static instability restricts the flow passage, resulting in an increase of pressure upstream, which causes the shell to reopen. Once the flow is re-established, the shell collapses once more, and this sequence of opening and closing is what constitutes a dynamic divergence. Based on the photographs, the oscillations evolve in the following three phases through time.

In Phase 1, the oscillations consist of regular, well-ordered, low-amplitude, low-frequency cycles about the buckled position with n=2 (for L/R=6) or n=3 (for L/R=4.5 and 2). Consecutive cycles have the same phase, meaning that nodes of the oscillation are not displaced. In this phase, the shell does not collapse completely and the walls do not contact each other, except in the last cycle, which fully closes the shell and drives the oscillations into Phase 2. Phase 1 usually lasts for less than 5 cycles, i.e., about 60 and 80 ms for the L/R=6 and 4.5 shells, respectively. Note that the photographs corresponding to phase 1 in Figures 3-2 and 3-3 are not for the last cycle of oscillation in this phase.

In Phase 2, the circumferential wave number changes to n=3 and the oscillations become larger, yet regular and well-ordered. Although the shell fully obstructs the airflow in each cycle in phase 2, the walls touch each other gently, as in the last cycle of Phase 1. The impact between the walls drives the shell into an anti-phase mode in the next cycle, meaning that the nodes of the oscillation are displaced (rotated) by π/n radians in each cycle, compared to the previous one. Note that the shell with L/R=2 does not undergo Phase 2 oscillations; the system goes directly from Phase 1 to Phase 3.

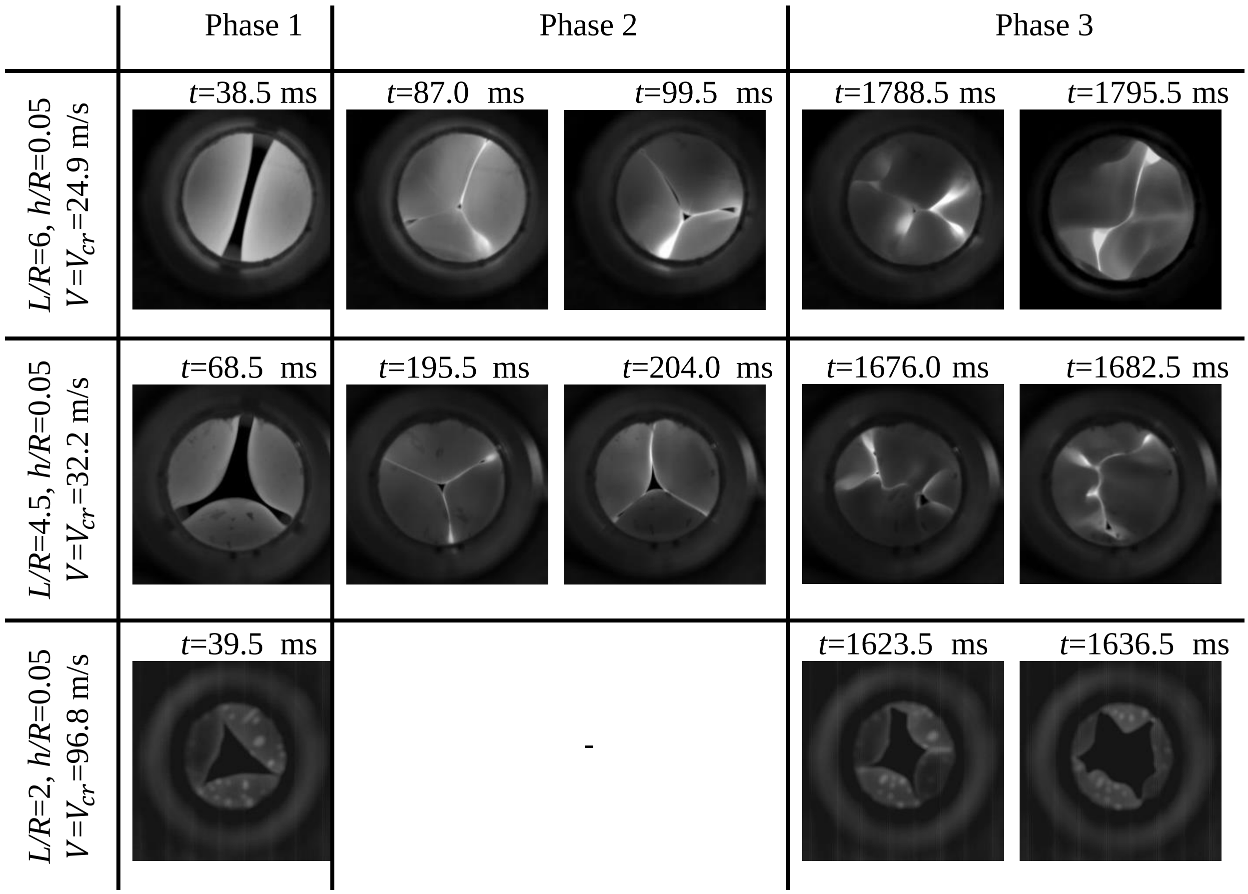

Figure 3-2. Cross-sectional patterns of motion, viewed from above the shells with different lengths, at the corresponding critical flow velocity, V_{cr}. Time t = 0 indicates the start of the oscillations.

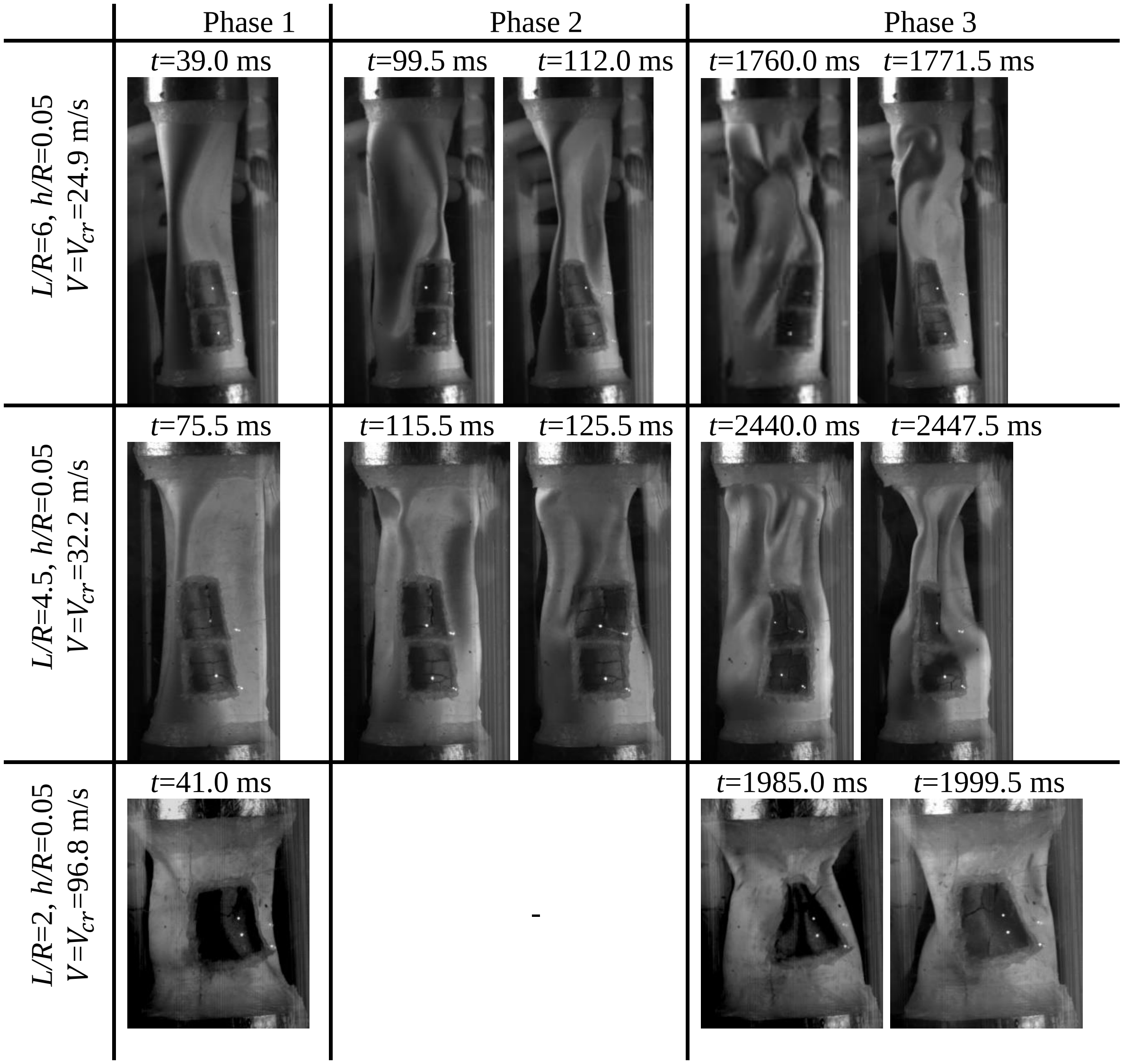

Figure 3-3. Axial patterns of motion, viewed from the front of the shells with different lengths, at the corresponding critical flow velocity, V_{cr}. In phase 2 and 3, consecutive cycles are shown, having anti-phase mode shape.

Phase 3 of the oscillations consists of chaotic-looking cycles with irregular and distorted cross-sectional shapes; many wrinkles and twisting of the shell are observed. Severe impact between opposing walls occurs and the airflow is fully obstructed for a portion of a cycle, depending on the length of the shell; shorter shells are closed for a shorter part of each cycle compared to longer shells. For the L/R=6 and 4.5 shells, the circumferential wave number is approximately n=2, but not well-defined. The L/R=2 shell, however, switches intermittently between n=3 and 4, or higher; the wave numbers are not well-defined. In this phase, as in Phase 2, the oscillations are anti-phase, except for the L/R=2 shell, for which this is not necessarily the case.

We call Phases 1 and 2 the primary phases; they vanish very quickly, lasting only 100 to 300 ms (20 to 50 cycles) from the start of oscillations, depending on the flow velocity and the length of shell; shorter shells (lower *L/R*) have a longer duration of primary phases at the same flow velocity; for example, the primary phases for the *L/R*=4.5 shell last three times longer than for the *L/R*=6 shell, both at *V*~27 m/s. Primary phases last longer at lower flow velocities. In the primary phases, the shell is closed for a shorter duration in each cycle compared to Phase 3.

In Phase 3, the shell closes completely for nearly half of the duration (period) of each cycle (except for very short shells, *L/R*≤ 2), during which the airflow is fully obstructed. This full closure forms a 'bubble' at the bottom of the shell. The flow pressure upstream of the collapsed throat of the shell increases, thus pushing the bubble upward. When this bubble has travelled through the lower half of the shell and is in the upper half, because of the forces leading to divergence and inertia, the reopened lower half of the shell buckles in an antiphase shape in the middle of the shell; a new cycle starts to form while the previous one is still evolving. The shell reaches its maximum collapse in the anti-phase mode, when the previous bubble has travelled through the length of the shell. Then, a new bubble reappears at the bottom of the shell in the new cycle of oscillation. This sequence of buckled antiphase shapes is repeated dynamically, giving rise to dynamic divergence. Although dynamic divergence is very similar to flutter, it should not be misinterpreted as flutter, which typically has a specific oscillation frequency at its onset.

The comparison of irregularity (chaos), amplitude, frequency, etc., of the oscillations for shells with different lengths or thicknesses, is difficult to discuss based on the photographs taken with the high-speed camera. Instead, the signal obtained from the lasers should be analyzed to determine the effect of length and thickness of the shell on the nature of the motion, such as the chaotic behaviour of the system, as discussed in Section 3.6.

3.5 The dynamics with varying flow velocity

In this section, the *L/R*=6 and *h/R*=0.09 shell is chosen to discuss the dynamical behaviour with varying flow velocity. Note that for the results presented in Sections 3.5, 3.6 and 3.7, the oscillations from 0 to 1 s have been discarded; hence, Phase 3 is dominant. Figure 3-4 shows the time history and the power spectral density of the oscillations for this shell at V=V_{cr}=28.5 m/s. As expected, the upper measurement point (at $\frac{1}{3}L$) has greater velocity due to the larger amplitude of motion. The frequency content of the motion consists of some commensurable peaks which are superharmonics of the fundamental frequency.

The bifurcation diagram of the rms of shell velocity is seen in Figure 3-5, showing how the rms of motion varies with varying flow velocity; refer to Section 3.3. The shell becomes unstable at the critical flow velocity, V_{cr}, and remains unstable between V_{cr} and V_{rest}. Below V_{rest}, the oscillations cease and the shell regains stability, i.e., the rms of motion goes to zero. As seen in Figure 3-5, the restabilization flow velocity, V_{rest}, is much smaller than the critical flow velocity, V_{cr}, displaying a very strong subcritical bifurcation, implying a softening nonlinear behaviour.

Figure 3-5 indicates that, by increasing the flow velocity beyond the restabilization value, V_{rest}, the rms velocity of the shell generally increases. However, at a specific V (∼22.5 m/s), the amplitude decreases with increasing V. Also, a sudden increase (jump) is seen at V∼25 m/s.

It should be mentioned that the chaotic component of the oscillation does not depend on the velocity amplitude. To investigate chaos and the complexity of the dynamics at different flow velocities, other measures, such as the largest Lyapunov exponent, should be employed, as in Section 3.7.

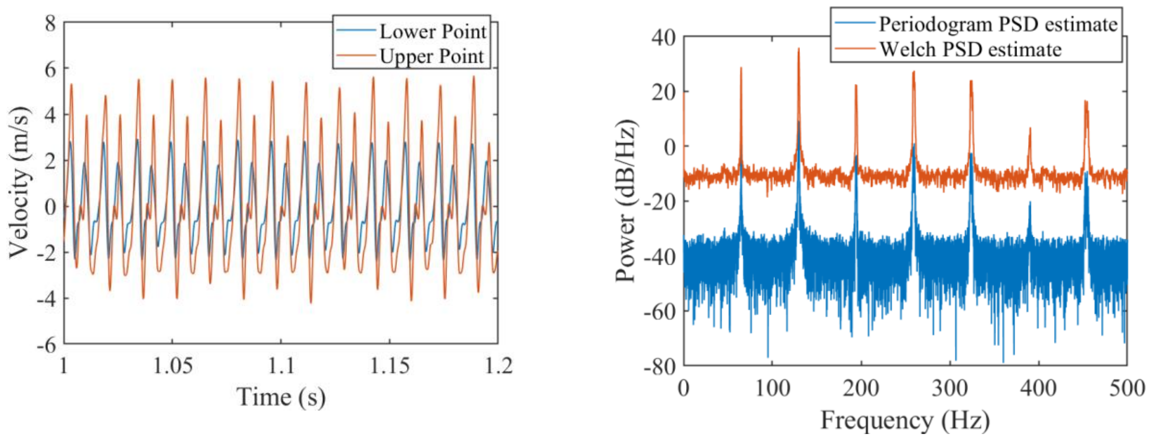

(a) (b)

Figure 3-4. (a) Time history of the velocity signal; (b) power spectral density (PSD), for the *L/R*=6 and *h/R*=0.09 shell at *V*=V_{cr}=28.5 m/s. The upper measurement point is at $\frac{1}{3}L$, while the lower one is at $\frac{1}{5}L$.

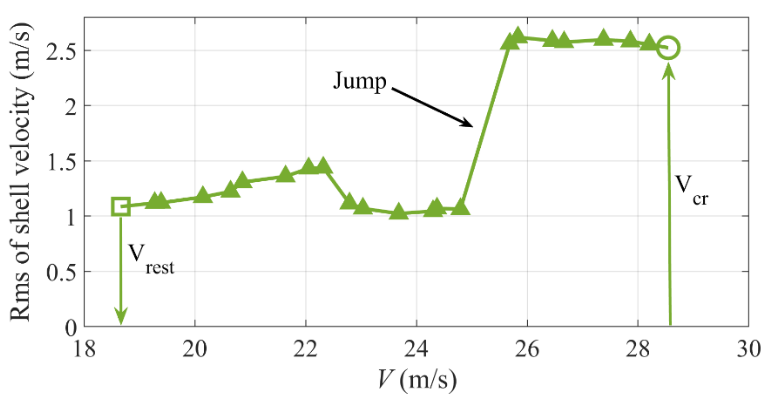

Figure 3-5. Bifurcation diagram of the rms velocity of the *L/R*=6 and *h/R*=0.09 shell. The critical and restabilization flow velocities are denoted by V_{cr} and V_{rest}, respectively.

3.6 Parametric study of the dynamic divergence

The focus of this paper is on the effect of geometric parameters of the shell, namely the length and thickness ratios (*L/R* and *h/R*, respectively), on the dynamic divergence instability. Thus, shells with different lengths and thicknesses, as in Table 3-2, have been tested. Their material properties and geometry are as in Table 1. In this section, a detailed description of the dynamics is given, as the flow velocity is increased, from the restabilization flow velocity, V_{rest}, up to the critical one, V_{cr}.

In Sections 3.6.13.6.2 and 3.6.2, the effect of *L/R* and *h/R* are discussed on the bifurcation of the rms velocity and the frequency content of the oscillations. Needless to mention that varying either the length or the thickness of the shell, not only affects the rms velocity of the oscillations, but also alters the critical and restabilization flow velocities.

Table 3-2. The geometry of the silicone rubber shells. *R* is the internal radius of the shell (the same for all shells, equal to 24.84 mm), *h* its thickness, and *L* its length

Shell #	L/R	h/R
1	6	0.05
2	5.5	0.05
3	4.5	0.05
4	2	0.05
5	6	0.09
6	4.5	0.09

Note that data at the critical flow velocity for shell 6 is not available due to shell rupture during the experiment. For shell 4, the critical and restabilization flow velocities are equal (the data is available only at this flow velocity due to the limitation of the maximum flow velocity attainable in the experimental set-up).

Figure 3-6 shows that thicker (higher *h/R*) and shorter (lower *L/R*) shells have higher critical and restabilization flow velocities compared to the thinner and longer ones. As mentioned earlier, V_{cr} and V_{rest} are equal for shell 4.

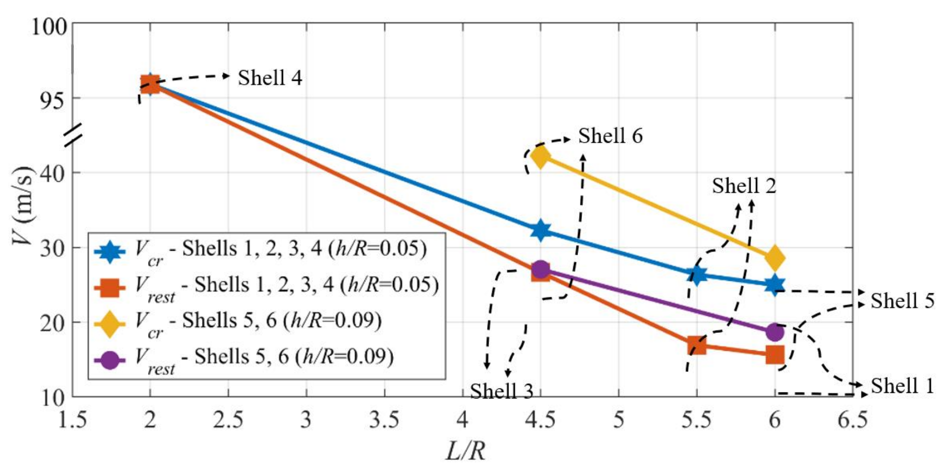

Figure 3-6. The critical and restabilization flow velocities of the shells, V_{cr} and V_{rest}, respectively.

As seen in Figure 3-6, V_{rest} is considerably smaller than V_{cr}, displaying a strong softening nonlinear behaviour. Figure 3-7 introduces a nondimensional parameter, $[V_{cr} - V_{rest}]$ / V_{cr}, as an indicator of the strength of the subcritical behaviour. It is seen that for thin shells (*h/R*=0.05), the subcritical behaviour is weakened for smaller *L/R*, while it remains approximately constant for thicker shells (*h/R*=0.09) of different lengths. For shell 4, the difference between V_{cr} and V_{rest} approaches zero, meaning that it does not show a subcritical behaviour (not shown in Figure 3-7).

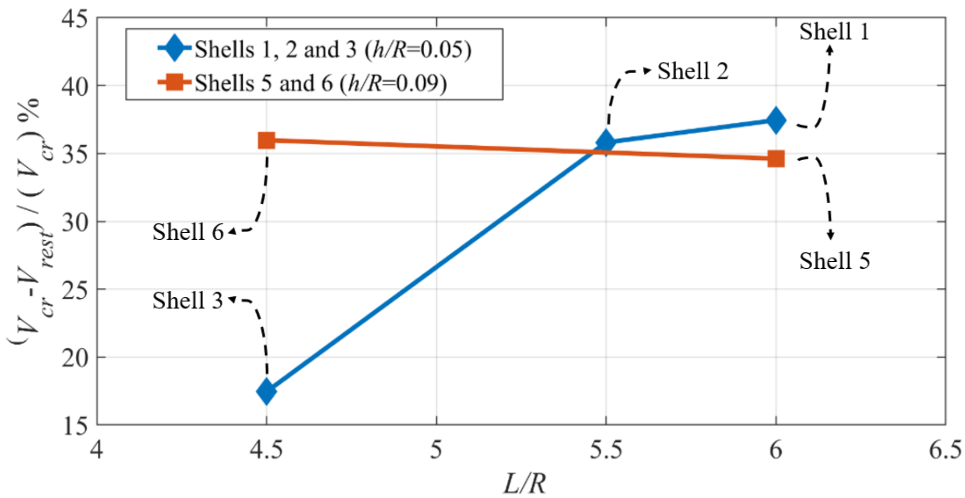

Figure 3-7. Nondimensionalized difference between the critical and restabilization flow velocities, indicating the strength of the subcritical behaviour of the shells.

3.6.1 The effect of varying the length of the shell

According to Figure 3-8, the rms velocity of all shells, except shell 4, generally increases with increasing flow velocity. For shell 4, the rms velocity has nearly the same value at V_{rest} and V_{cr}. Interestingly, a sudden increase (jump) is seen in the rms velocity of shells 1, 2 and 5 in Figures 3-8 and 3-10. For short shells, there might be such a jump at flow velocities higher than the available experimental data.

Figure 3-8 shows that it is difficult to make a general decision on whether shorter/longer shells have higher/lower rms velocities. Figure 3-8(a) demonstrates that by decreasing the length ratio (*L/R*) from 6 (shell 1) to 5.5 (shell 2), the rms velocity increases. However, further decrease of *L/R* from 5.5 to 4.5 (shell 3), and then from 4.5 to 2 (shell 4), reduces the rms velocity; shells 2 and 4 have the lowest and the highest rms velocities, respectively.

According to Figure 3-8(b) (thick shells), shell 6 (*L/R*=4.5) has lower rms velocity than shell 5 (*L/R*=6), for *V*~27-29 m/s. Beyond *V*~32 m/s, however, shell 6 has higher rms velocity than shell 5.

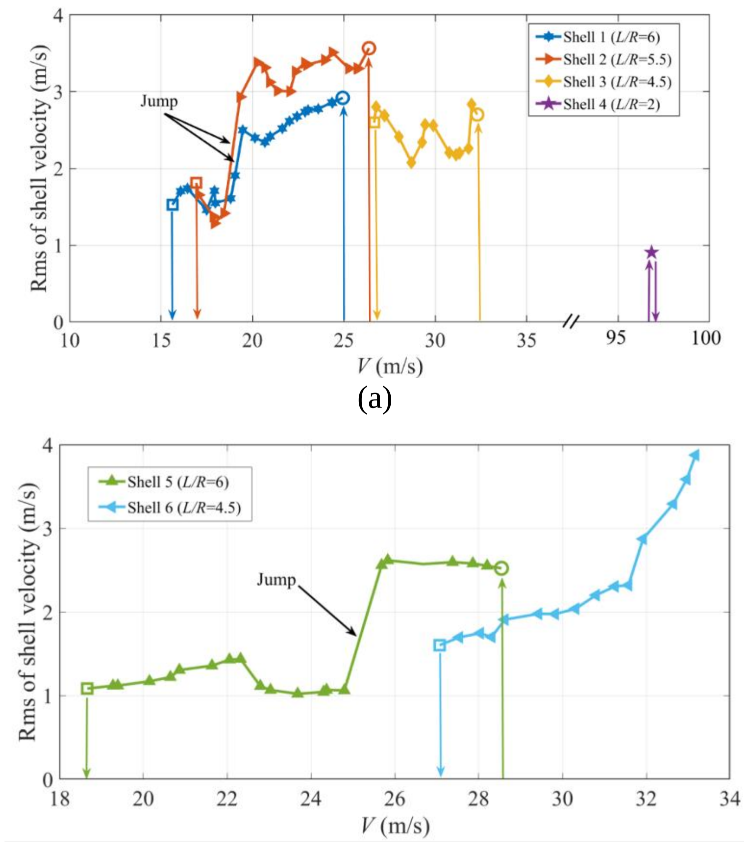

(a)

(b)

Figure 3-8. Bifurcation diagram of the rms velocity of shells with (a) *h/R*=0.05 (thin shells); (b) *h/R*=0.09 (thick shells). Hollow squares and hollow circles indicate the restabilization and critical flow velocities, respectively.

The Fourier transform might not be the best tool to analyze nonstationary signals, because the frequency content of such signals changes over time; the Fourier transform is only localized in frequency, but not in time. Wavelets, on the other hand, are a powerful tool localized in both time and frequency; hence, Morse wavelets have been employed in this study to extract the frequency content of the oscillations over time at different flow velocities. For a detailed discussion of the concept and usage of wavelets refer to [31].

Figure 3-9 shows the magnitude of the continuous wavelet transform (CWT) of the shell velocity signal in the frequency-time domain. Figure 3-9 has the same range of flow velocities as the bifurcation diagrams of the corresponding shells, Figure 3-8(b), meaning that the first vertical strip corresponds to V_{rest}, and the last strip corresponds to V_{cr}. At most flow velocities, more than one frequency range (band) exists. These frequency bands are often not distinct from one another presenting broad frequency ranges which might be associated with chaos in the system; chaotic oscillations often exhibit a broad-band frequency content, rather than a number of narrow and well-defined frequency peaks expected for periodic motions. The prediction of chaos in the system at different flow velocities is discussed in detail in Section 3.7.

Figure 3-9 demonstrates that the frequency of oscillations of the thick shells, either long or short, increases with increasing flow velocity from V_{rest} towards V_{cr}; all frequency bands, including the one containing high-energy content (in dark blue), have higher values at higher V. However, it is difficult to compare the frequency of oscillations of the two shells, which have different length ratios, based on Figure 3-9, because, as mentioned above, the frequency bands are wide and not distinct from one another at most flow velocities. Besides, the two wavelet scalograms do not have the same magnitude scale, making the discussion of the length effect on the frequency of oscillation difficult.

For both shells 5 and 6, in Figure 3-9, higher magnitudes are displayed for increasing flow velocity, indicating that the signal strength (energy) is higher at higher flow velocities. This is in agreement with the trend of the bifurcation diagrams shown with red dashed lines; the rms velocity of both shells increases with increasing flow velocity. The abrupt increase of the signal strength of shell 5 at V=25.6 m/s, Figure 3-9(a), confirms the existence of the jump in its bifurcation diagram, Figure 3-8(b), at exactly the same flow velocity. The same accordance between the jump in the rms velocity of shells 1 and 2 and their corresponding wavelet scalograms has been observed.

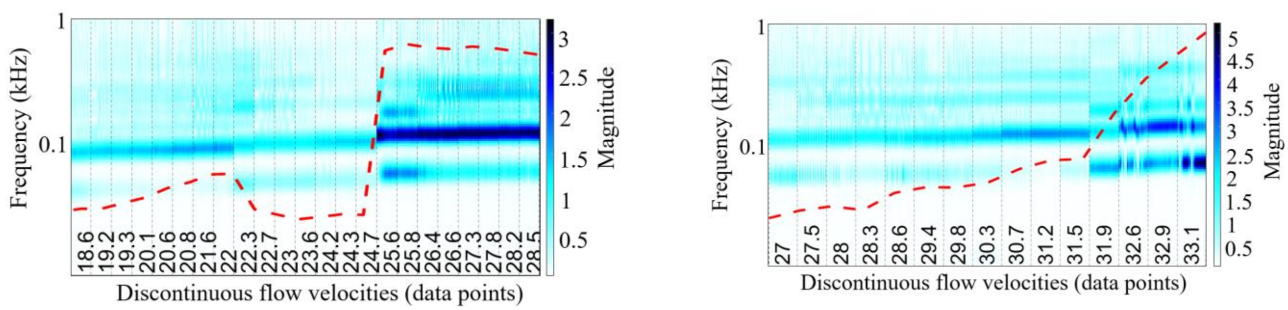

(a) (b)

Figure 3-9. Morse wavelet scalogram at discontinuous flow velocities indicated in m/s, at the bottom of the plots; 10 s of oscillations at each flow velocity have been recorded and analyzed. (a) Shell 5 (*L/R*=6, *h/R*=0.09); (b) shell 6 (*L/R*=4.5, *h/R*=0.09). Dashed red lines indicate the trend of rms velocity in the corresponding bifurcation (not to scale).

3.6.2 The effect of varying the thickness of the shell

Figure 3-10 shows that, no matter whether the shell is long or short, thinner shells (lower *h/R*) generally have higher rms velocity.

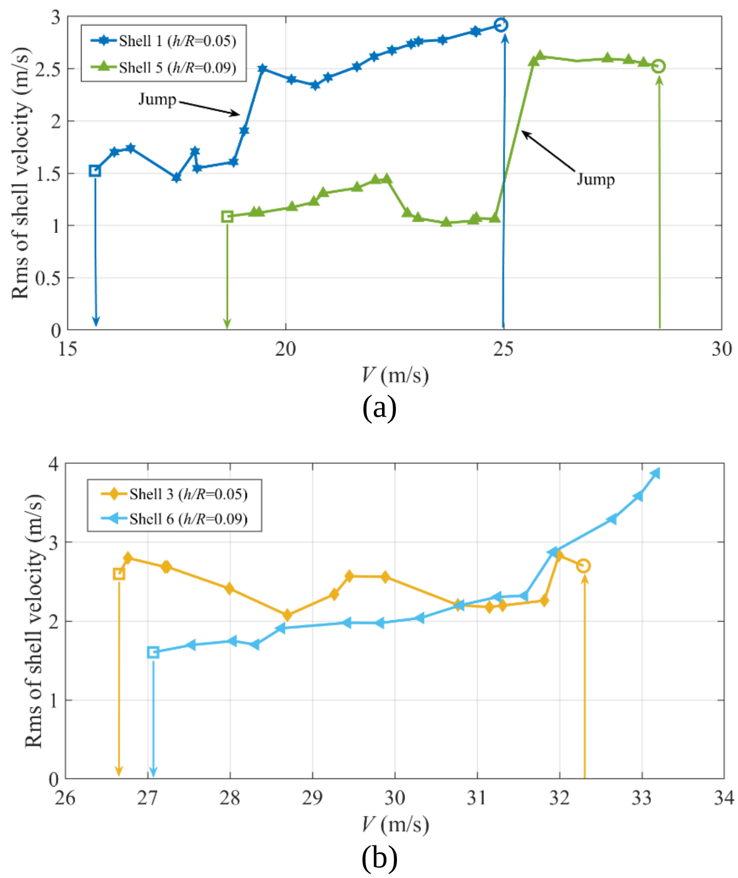

Figure 3-10. Bifurcation diagram of the rms velocity of shells with (a) *L/R*=6 (long shells); (b) *L/R*=4.5 (short shells). Hollow squares and hollow circles indicate the restabilization and critical flow velocities, respectively.

According to Figure 3-11, short shells (*L/R*=4.5), either thin or thick, have frequency bands with higher values at higher flow velocities. The dominant frequency range in dark blue which is associated with the signal strength (energy), exists at lower frequencies for the thin shell, Figure 3-11(a), compared to the thick shell, Figure 3-11(b), at most flow velocities. For both shells, the trend of the signal strength versus flow velocity in Figure 3-11, is in complete agreement with the trend of the corresponding bifurcation diagrams shown with red dashed lines (the same as bifurcation diagrams in Figure 3-10(b)).

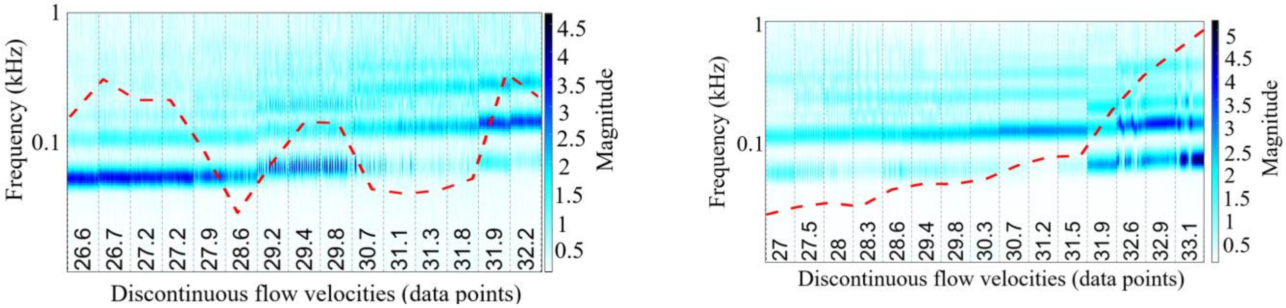

(a) (b)

Figure 3-11. Morse wavelet scalogram at discontinuous flow velocities indicated in m/s, at the bottom of the plots; 10 s of oscillations at each flow velocity have been recorded and analyzed. (a) Shell 3 (*L/R*=4.5, *h/R*=0.05); (b) Shell 6 (*L/R*=4.5, *h/R*=0.09). Dashed red lines indicate the trend of rms velocity in the corresponding bifurcation (not to scale).

3.7 The chaotic component of the oscillation

According to the photographs taken with the high-speed camera, Figures 3-2 and 3-3, there appears to be a chaotic component in the oscillations. Besides, the wavelet scalograms, Figures 3-9 and 3-10, exhibit wide frequency bands indistinct from one another, which could be an indicator of chaos in the system. Chaotic motions are unpredictable, nonperiodic, random-like motions which are very sensitive to initial conditions, and correlation of present with past is lost rapidly with time. The results presented in this section prove that a weak or strong chaotic component exists in the motion, depending on the parameters of the system such as the flow velocity, length and thickness of the shells. Weak chaotic motions, yet with a strong periodic component, are referred to as 'limited' or 'narrow-band' chaos in the literature [32]. Narrow-band chaotic oscillations display similar characteristics to periodic (regular) motions. On the other hand, a system is said to have 'large-scale' or 'broad-band' chaos, when a strong chaotic component exists in the motion. In this case, the system behaviour is totally different from a periodic motion.

It is always recommended not to count on only one indicator of chaos in dynamics experiments, but to use several techniques before pronouncing a system as chaotic. In the present study, the putative existence of chaos in the system is confirmed by means of various quantitative or qualitative measures. First, we employed the Wolf algorithm to determine the largest Lyapunov exponent, λ_1, from the time series, which not only confirms the existence of a chaotic component by a positive λ_1, but also gives a quantitative measure of its relative strength at different values of *V*; refer to [33]. To confirm the results of the largest Lyapunov exponent, the oscillations of shells with different length or thickness ratios, but at nearly the same flow velocity, are analyzed and compared in pairs, as shown in Table 3-3, using tools such as Power Spectral Densities (PSDs), Poincaré maps, phase portrait plots, Probability Density Functions (PDFs) and autocorrelations.

Table 3-3. Selected points (flow velocities, *V*), identified in the figure indicated, to be analyzed in terms of strength of the chaotic component, and corresponding flow velocities, *V*. Each pair of points is to be compared in the corresponding section.

Section	Point	Shell	V (m/s)
3.7.1	5_A	5	28.2
(Figure 3-12(b))	6_A	6	28.0
3.7.2	3_A	3	31.8
(Figure 2-10(b))	6_B	6	31.9
3.7.3	2_A	2	18.4
(Figure 3-18)	2_B	2	20.2

3.7.1 Short versus long shell

According to Figure 3-12(a), the largest Lyapunov exponent generally takes greater values at higher flow velocities, with some exceptions; more precisely, the following trends have been observed for the thin shells (shells 1, 2 and 3) while increasing the flow velocity from V_{rest} towards V_{cr}.

1. The largest Lyapunov exponent generally increases as the flow velocity is increased from V_{rest} up to V~17.5, 18.4 and 28.7 m/s for shells 1, 2 and 3, respectively.
2. Beyond the aforementioned flow velocities, λ_1 sharply drops, indicating that motions become more predictable and less sensitive to uncertainties in initial conditions. The decreasing trend of λ_1 with the flow velocity continues up to V~19.4, 20.7 and 29.5 m/s for shells 1, 2 and 3, respectively.
3. Beyond the aforementioned flow velocities, the oscillations restart to show increasing irregularity, and λ_1 increases abruptly up to V~23.6, 26.7 and 31.8 m/s for shells 1, 2 and 3, respectively.
4. Finally, for still higher flow velocities towards V_{cr}, λ_1 decreases slightly for shells 1 and 2, but greatly for shell 3.

As mentioned earlier, for shell 4, there is only one experimental data point available, at a single flow velocity, V=V_{rest}=V_{cr}=96.8 m/s, which is associated with a relatively high λ_1 (Figure 3-12(a)).

According to Figure 3-12(b), for thick shells (shells 5 and 6), the largest Lyapunov exponent is generally higher at the lower half of the flow velocity range, showing two peaks, yet with an irregular trend with several ups and downs when the flow velocity is increased from V_{rest} towards V_{cr}.

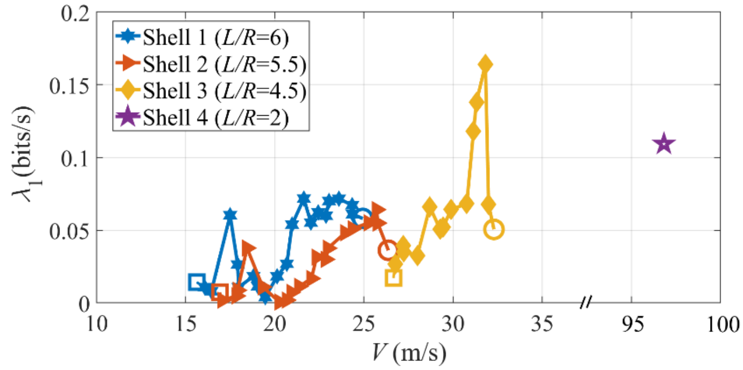

(a)

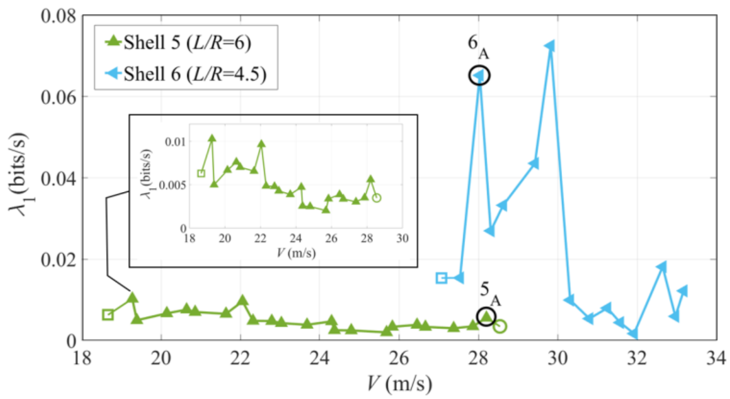

(b)

Figure 3-12. The largest Lyapunov exponents, λ_1, at different flow velocities for shells with (a) *h/R*=0.05 (thin shells); (b) *h/R*=0.09 (thick shells). A zoomed-in view of the largest Lyapunov exponent for shell 5 is shown as an insert (in a box) in (b). Hollow squares and hollow circles indicate the restabilization and critical flow velocities, respectively.

The largest Lyapunov exponent (λ_1) for thin shells, Figure 3-12(a), demonstrates that by decreasing the length ratio (*L/R*) from 6 to 5.5, the oscillations become more regular and less erratic. However, for a smaller length ratio *L/R*=4.5, and also *L/R*=2, λ_1 often takes higher values, indicating a stronger chaotic behaviour compared to the longer shells. Similarly, Figure 3-12(b) shows that the thick shell with lower *L/R* (shell 6) has higher λ_1 over most of the flow velocity range, exhibiting more irregular and erratic oscillations.

To sum up, one can conclude that, with some exceptions, shorter shells generally display more complex dynamics. To confirm the largest Lyapunov exponent results regarding the effect of length on chaotic behaviour, the oscillations of shells 5 and 6 (both having the same thickness ratio, *h/R*=0.09), at *V*~28.0 m/s (points 5_A and 6_A in Table 3-3), are analyzed in Figures 3-13 and 3-14. [The term “point” in Table 3-3 should not be confused with the measurement point on the shell; for all shells, the signal is obtained from a point on the shell at $\frac{1}{3}L$ from the upstream (lower) clamp, the “higher measurement point”].

Figure 3-13(a) shows the velocity signal of the oscillations corresponding to points 5_A and 6_A for 1-1.2 s. As mentioned in Section 3.3, 10 s of oscillations at each flow velocity step has been recorded to be analyzed.

According to Figure 3-13(b), the PSD of point 5_A displays a finite number of well-pronounced commensurable peaks which are superharmonics of the fundamental frequency. This is often associated with oscillations with a dominant periodic component, as expected from the low value of the Lyapunov exponent in Figure 3-12(b). Point 6_A, on the other hand, has a broad-band spectrum with cone-like peaks instead of sharp spikes. Note that the frequency range of the PSDs plotted is quite wide (0-500 Hz); hence, each cone-like peak includes a considerable range of frequencies, not one specific value. This implies a strong chaotic behaviour since chaotic signals display a wide frequency bandwidth with a nearly continuous distribution of frequencies.

Figure 3-13(c) shows the Poincaré maps associated with points 5_A and 6_A. Different methods exist to obtain Poincaré maps, as explained in [34]. However, when the system does not have a natural clock such as the external periodic excitation, displacement-triggered (or generally "position-triggered") Poincaré maps are often used. In this case, maps are obtained by sampling the data when another variable of the system reaches a peak value. Here, when the velocity of the lower measurement point crosses from negative to positive, meaning that the displacement has a local maximum value, time is stored. Then, the velocity and displacement of the upper measurement point at the sampled instances are plotted. The Poincaré map of point 5_A consists of two clean basins, signifying a period-2 motion with a dominant periodic component. The basin boundaries are smooth continuous lines, indicating that small uncertainties in the input parameters do not influence the response of the system when away from the basin boundaries. The Poincaré map of point 6_A, however, shows a fractal-looking collection of points, with nonsmooth basin boundaries, implying that the behaviour of the system is unpredictable. This suggests a chaotic component in the oscillations.

According to Figure 3-13(d), the phase portrait of point 5_A shows clean orbits which overlap, indicating a dominant periodic component. On the other hand, the phase portrait plot associated with point 6_A tends to fill a certain subspace of the phase plane. This behaviour suggests the existence of a dominant chaotic component in the oscillations.

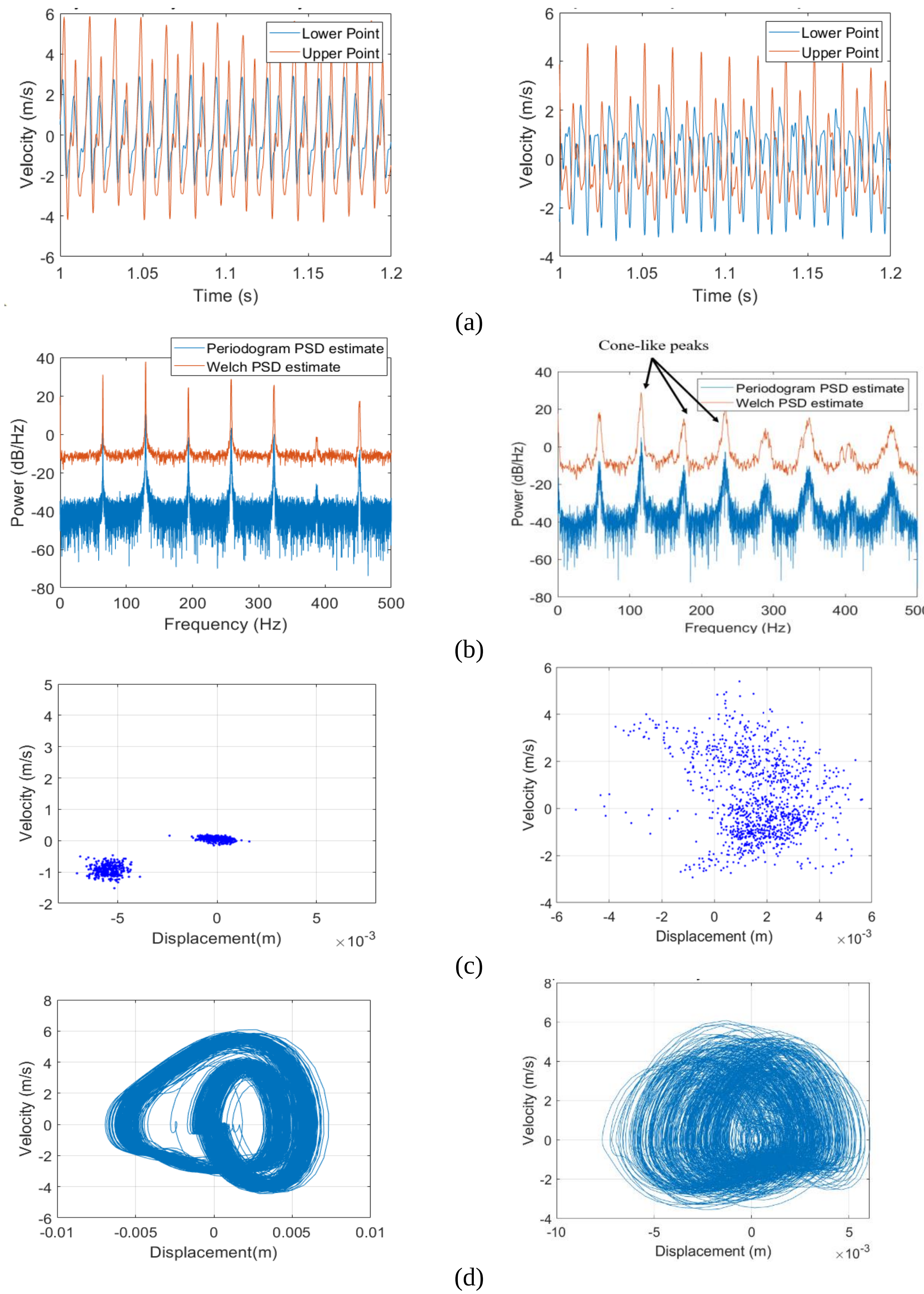

Figure 3-13. Study the effect of length (comparison between points 5_A and 6_A in Figure 3-12). Plots on the left side correspond to 5_A (longer thick shell), and on the right side to 6_A (shorter thick shell). (a) Time histories; (b) PSDs; (c) Poincare maps; (d) phase portraits.

Pseudo-phase space (also called delay-reconstructed phase space) is often employed when only one system variable is available. Pseudo-phase space demonstrates the same behaviour in the phase space as the typical phase space constructed with more than one system variable. In the present study, the pseudo-phases are constructed not only to reveal the behaviour of orbits in phase space, but also to determine the largest Lyapunov exponent of chaotic time series. To construct a pseudo-phase space, two parameters, namely the embedding dimension, *m*, and delay, *d*, are needed. Here, the embedding dimension is chosen by the method of 'educated guesses' to ensure that the orbit is topologically reasonable in *m* dimensions and unnecessary self-intersections do not occur. The delay parameter should be selected so that the pseudo-orbit is expanded as much as possible, while maintaining a deterministic orbit structure [35]. The consistency of results is then assessed by choosing nearby values for the delay. The selection of *m* and *d* is discussed in detail in [33]. The results show a weak dependence on the choice of delay. According to Figure 3-14(a), the pseudo-phase space associated with point 5_A forms a closed orbit which is an indication of a dominant periodic component, whereas the pseudo-phase space of point 6_A shows fractal orbits looking like a scattered cloud of points, suggesting sensitive dependence on initial conditions.

As mentioned before, a small change in the initial conditions of a chaotic system will alter its response, making it impossible to predict the time history. Here, the probability density function, PDF, comes into play as a statistical measure of the dynamics of the system. The PDF of oscillations with a dominant periodic component shows two dominant peaks at the extremes of the displacement; the motion is slow there, and the probability of finding the oscillating system there is high. As the chaotic component of the oscillation intensifies, its PDF tends to deviate from this double-masted shape and exhibits more of a normal (Gaussian) distribution. According to Figure 3-14(b), the PDF associated with point 5_A suggests a weak chaotic component in the oscillations, while that of point 6_A shows a strong chaotic behaviour since the space in between the two peaks is filled.

The autocorrelation, by definition, is the correlation of a signal with a delayed copy of itself as a function of delay. The autocorrelation of periodic oscillations is periodic with time, implying statistical similarity between delayed versions of oscillations. Chaotic signals, however, lose memory very rapidly and have an autocorrelation decaying with time. Although all the previous results show that points 5_A and 6_A indicate weak and strong chaotic behaviour, respectively, there is not a clear difference between the autocorrelation of the two points in Figure 3-14(c).

To summarize, all the results presented in Figures 3-13 and 3-14 (except Figure 3-14(c)) confirm the predictions reached on the basis of the largest Lyapunov exponent in Figure 3-12, that longer shells undergo oscillations with a weaker chaotic component.

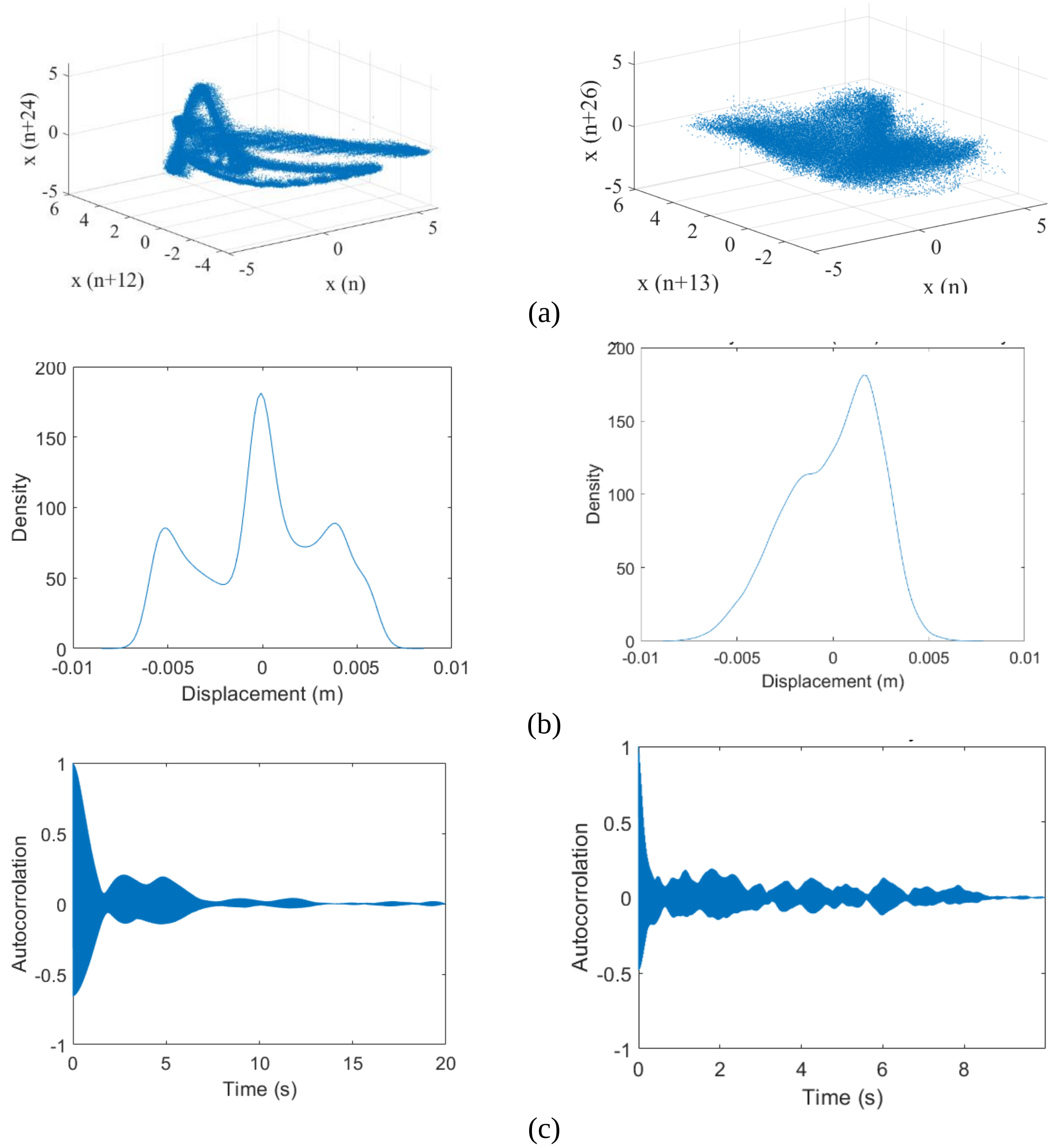

Figure 3-14. Study of the effect of length (comparison between points 5_A and 6_A in Figure 3-12). Plots on the left side correspond to 5_A (longer thick shell), and on the right side to 6_A (shorter thick shell). (a) Pseudo-phase spaces; (f) PDFs; (g) autocorrelations.

3.7.2 Thin versus thick shell

Figure 2-10 shows that thinner shells, no matter whether long or short, have a higher largest Lyapunov exponent, λ_1, than thicker shells over most of the flow velocity range; hence, displaying stronger chaotic behaviour. To confirm the largest Lyapunov exponent results regarding the effect of thickness of the shell on the chaotic behaviour, the oscillations of shells 3 and 6 (both with the same length ratio, L/R=4.5) at V~31.8 m/s (points 3_A and 6_B in Table 3-3), are analyzed in Figures 3-16 and 3-17.

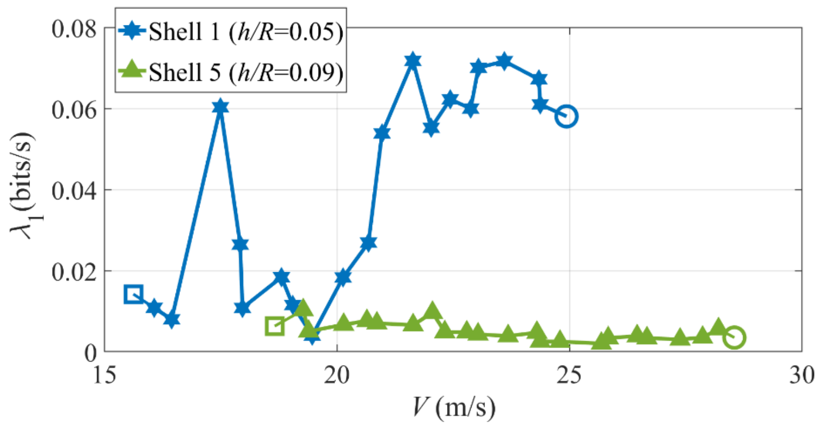

(a)

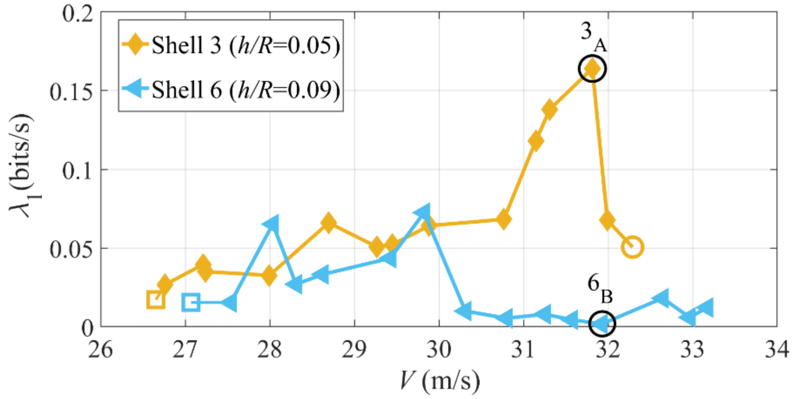

(b)

Figure 3-15. The largest Lyapunov exponents, λ_1, at different flow velocities for shells with (a) *L/R*=6 (long shells); (b) *L/R*=4.5 (short shells). Hollow squares and hollow circles indicate the restabilization and critical flow velocities, respectively.

Figure 3-16(a) shows the time traces associated with points 3_A and 6_B. The time history of oscillations at point 3_A shows complex patterns which do not seem similar in different cycles. On the other hand, the time trace of point 6_B displays a clean repetitive pattern which looks like a superposition of sinusoids. The PSD of point 3_A consists of continuous cone-like spikes, while that of point 6_B demonstrates conspicuous sharp peaks, Figure 3-16(b). According to Figure 3-16(c), the Poincaré map of point 3_A exhibits a fractal-looking cloud of scattered points. The Poincaré map of point 6_B, however, shows two clean basins (period-2 oscillations) with smooth boundaries. The phase portrait of oscillations at point 3_A consists of orbits which tend to fill the phase plane, whereas that of point 6_B demonstrates clean overlapping orbits which coalesce, Figure 3-16(d).

All these measures indicate that the oscillations associated with point 3_A have a dominant chaotic component (broad-band chaos), while point 6_B consists of much more regular (less erratic) oscillations with a very weak chaotic component (narrow-band chaos).

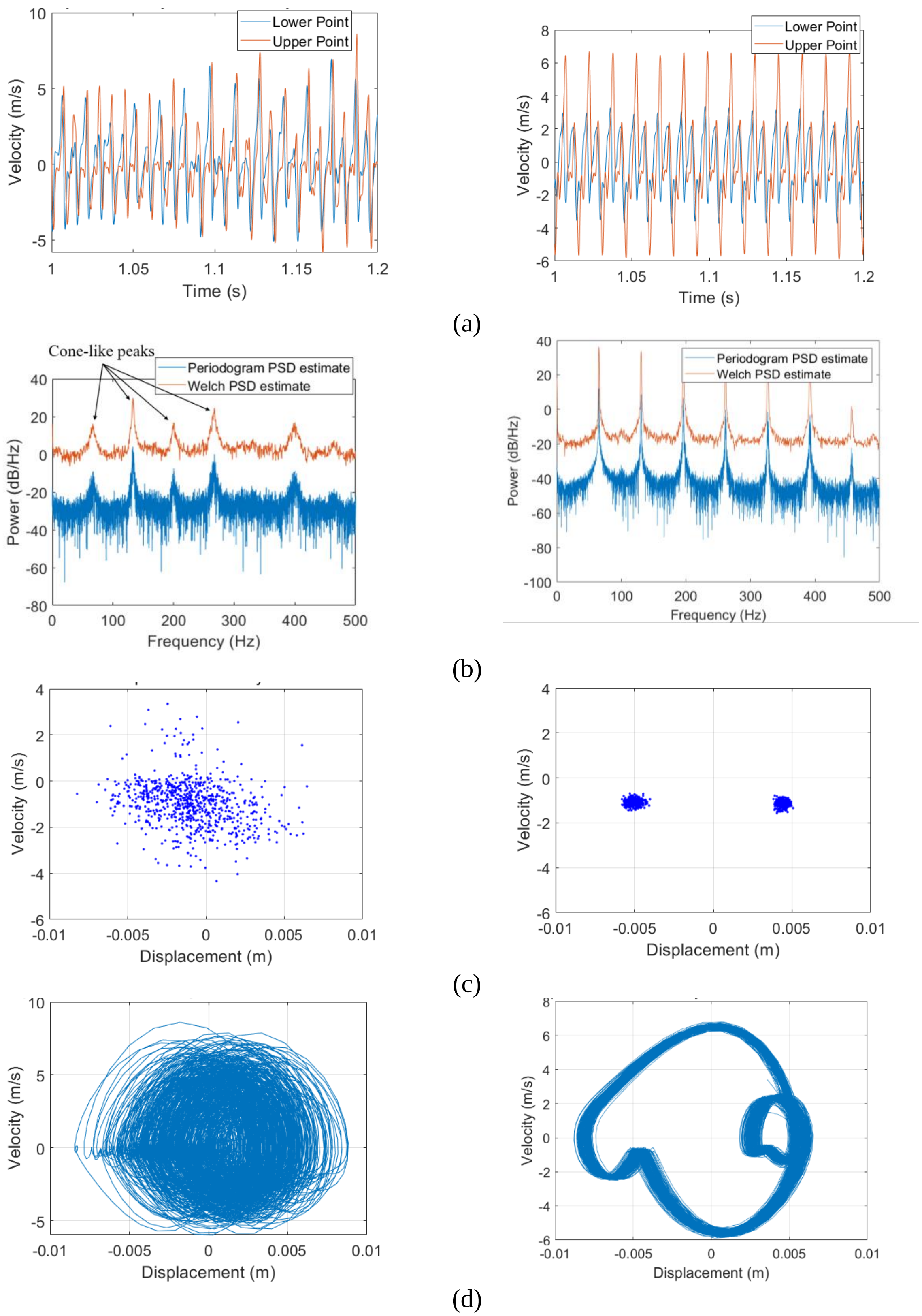

Figure 3-16. Thickness study (comparison between points 3_A and 6_B in Figure 2-10). Plots on the left side correspond to 3_A (thinner short shell), and on the right side to 6_B (thicker short shell). (a) Time histories; (b) PSDs; (c) Poincare maps; (d) phase portraits.

According to Figure 3-17, the oscillations at point 3_A correspond to a scattered pseudo-phase space. On the other hand, the pseudo-phase space of point 6_B has similar orbits in the phase space as those of periodic motion (closed curves). The PDF of oscillations at point 3_A exhibits a Gaussian distribution (a bell-shaped curve), while that of point 6_B shows two peaks at the extremes of the displacement, with a slight departure from the double-masted shape. Lastly, the autocorrelation of oscillations at point 3_A dies out rapidly with time, whereas point 6_B demonstrates a statistical similarity between delayed versions of oscillations. In conclusion, the oscillations associated with point 6_B display a weak chaotic behaviour, yet with a strong periodic component. The results for point 3_A, however, show a dominant chaotic behaviour. More details about the above-mentioned measures can be found in Section 3.7.1.

To sum up, the detailed results of Figures 3-16 and 3-17 confirm the prediction of the largest Lyapunov exponent in Figure 2-10, that the oscillations of thicker shells are generally less chaotic than those of thinner ones.

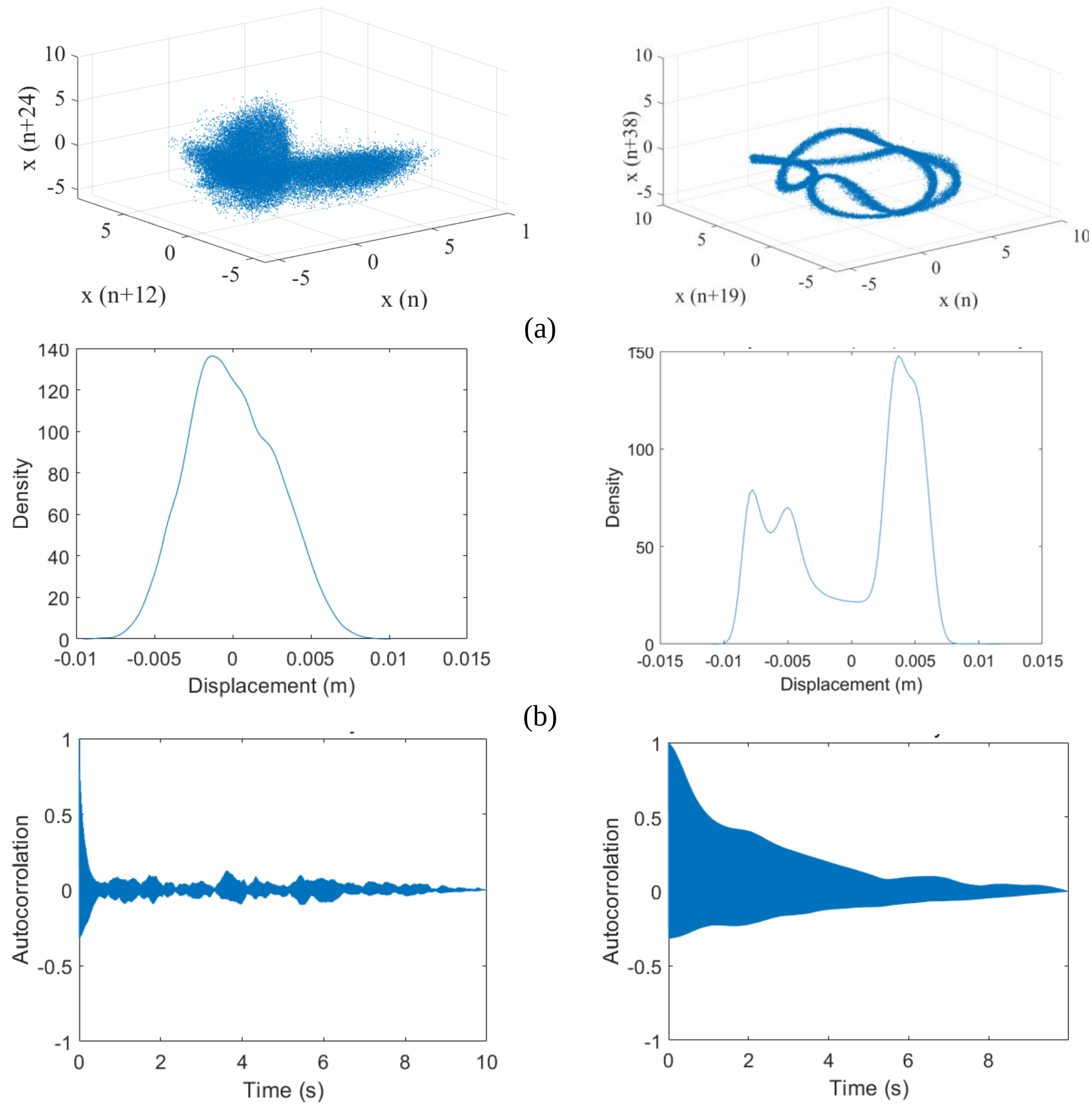

Figure 3-17. Thickness study (comparison between points 3_A and 6_B in Figure 2-10). Plots on the left side correspond to 3_A (thinner short shell), and on the right side to 6_B (thicker short shell). (a) Pseudo-phase spaces; (b) PDFs; (c) autocorrelations.

3.7.3 The effect of jump in rms velocity on chaotic behaviour

This section presents further study on the effect of the jumps observed in the bifurcation diagrams of long shells (shells 1, 2 and 5), Figure 3-8, yielding some exciting results. Table 3-4 lists the approximate flow velocities at which the jump in the rms velocity of the long shells occurs, V_{jump}.

According to Figure 3-18, the jump in the rms velocity weakens the chaotic behaviour; in fact, the data point just beyond the jump has the minimum λ_1(therefore, the least irregularity) for the entire flow velocity range, for all the three long shells. For flow velocities beyond the jump, the chaotic component restarts to intensify.

Table 3-4. Long shells showing a jump in their bifurcation diagrams (Figure 3-8) and the corresponding flow velocities at which the jump occurs, V_{jump}.

Shell	V_{jump} (m/s)
1	19.0
2	19.3
5	25.2

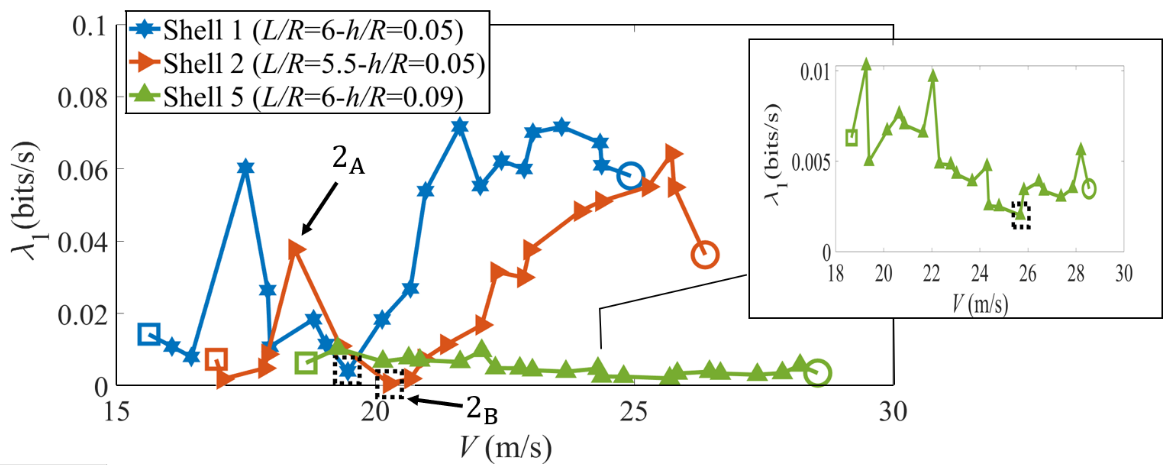

Figure 3-18. The largest Lyapunov exponents, λ_1, at different flow velocities for long shells (shells 1, 2 and 5). A zoomed-in view of the largest Lyapunov exponent for shell 5 is shown in the box on the right. Hollow squares and hollow circles indicate the restabilization and critical flow velocities, respectively. The dotted boxes show the data point just beyond the jump in the rms velocity of the corresponding shell.

To confirm the largest Lyapunov exponent results regarding the effect of the jump on chaotic content of the oscillations, the oscillations of shell 2 (*L/R*=5.5, *h/R*=0.05) at *V*=18.4 (just before the jump) and 20.2 m/s (just beyond the jump), respectively points 2_A and 2_B in Table 3-3, are analyzed in Figures 3-19 and 3-20. The sudden increase of the signal strength (wavelet magnitude) of shell 2 at *V*=19.3 m/s, Figure 3-19, confirms the existence of the jump in its bifurcation diagram, Figure 3-8(a), which occurs exactly at the same flow velocity. Similar accordance between the jump in the bifurcation of other long shells (shells 1 and 5) and their wavelet scalograms has been observed. According to Figure 3-20(a), the oscillations at point 2_A correspond to a scattered Poincaré map with nonsmooth fractal basin boundaries. On the other hand, the Poincaré map of point 2_B demonstrates four clean basins with smooth boundaries (period-4 oscillations). The PDF of oscillations at point 2_A exhibits a severe departure from the perfect double-masted shape, while that of point 2_B shows two peaks at the extremes of the displacement, Figure 3-20(b). Finally, Figure 3-20(c) demonstrates that the autocorrelation of oscillations at point 2_A vanishes rapidly with time, whereas point 2_B maintains a statistical similarity between delayed versions of oscillations.

In conclusion, the oscillations associated with point 2_B display a weak chaotic behaviour, yet with a strong periodic component, while point 2_A shows a dominant chaotic component in the oscillations. This is in agreement with the largest Lyapunov exponent estimation, Figure 3-18, having its minimum value (the weakest chaotic behaviour) just beyond the jump, over the entire range of flow velocities.

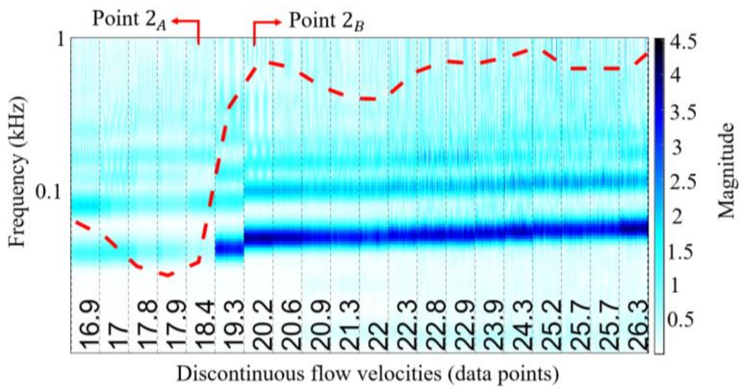

Figure 3-19. Morse wavelet scalogram for shell 2 (*L/R*=5.5, *h/R*=0.05) at discontinuous flow velocities indicated in m/s, at the bottom of the plots; 10 s of oscillations at each flow velocity have been recorded and analyzed. Dashed red lines indicate the trend of rms velocity of corresponding bifurcation (not to scale).

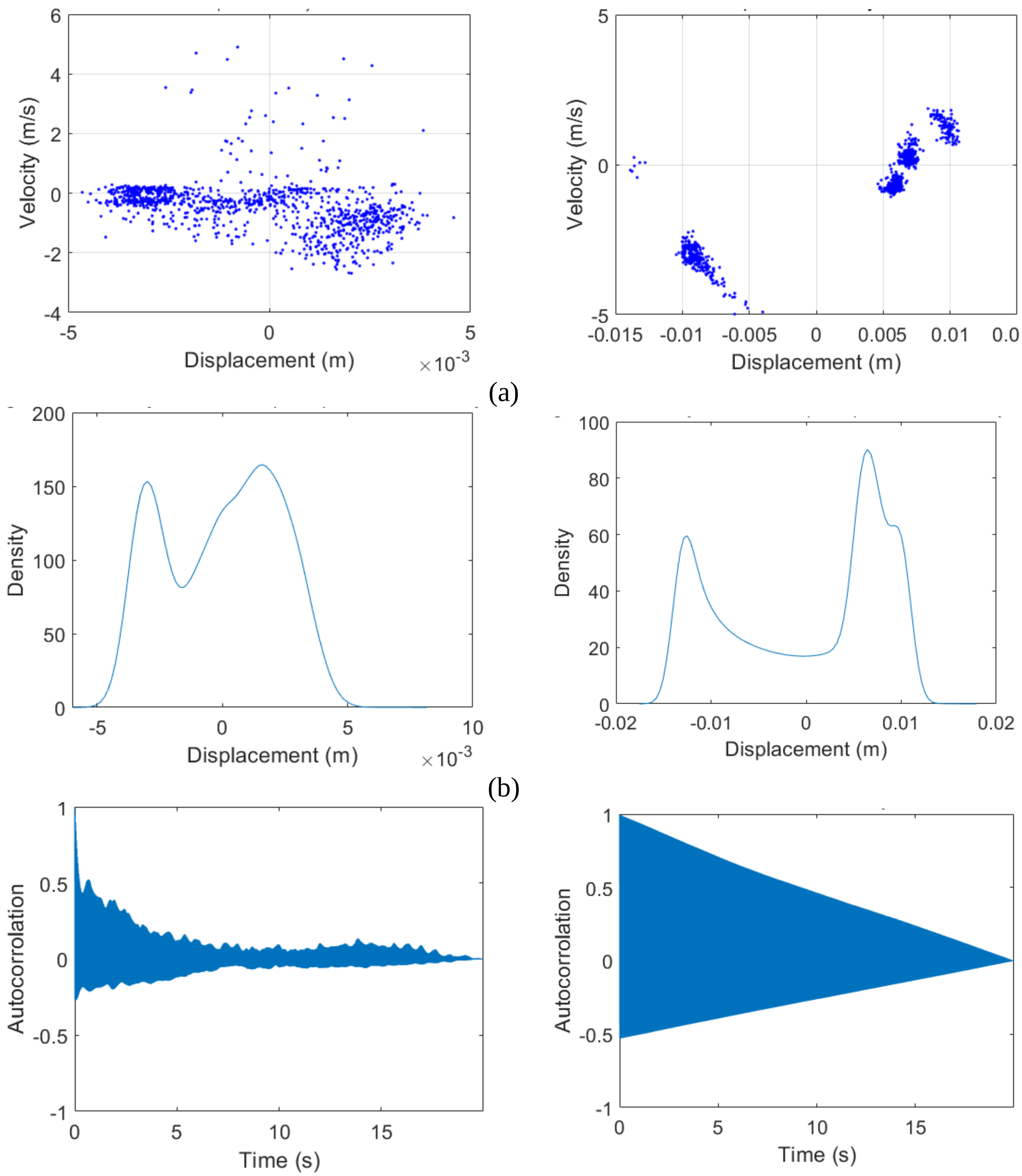

(c)

Figure 3-20. Jump study for shell 2 (comparison between points 2_A and 2_B in Figure 3-12). Plots on the left side correspond to 2_A (below the jump), and on the right side to 2_B (beyond the jump). (a) Poincare maps; (b) PDFs; (c) autocorrelations.

3.8 Study on confinement effect

The results presented in Sections 3.5, 3.6 and 3.7 have been obtained with the experimental set-up as in Figure 3-1(b), with a rigid (plexiglas) outer tube and two small holes (D_h= 3 mm), one upstream and the other downstream of the tested shell to equalize the pressure in the annulus to the mean internal pressure. However, it was thought interesting to investigate the influence of confinement, as a result of the presence of the plexiglas tube, on the dynamics of the system, by comparing the oscillations of shell 3 (L/R=4.5, h/R=0.05), with and without confinement. To do this, the apparatus was modified and the rigid (plexiglas) tube was removed, and the small holes at the upper and lower clamps were blocked.

Figure 3-21 shows the bifurcation diagrams for the two configurations (with or without the rigid outer tube), according to which the rms velocity of the oscillations are higher for the unconfined configuration.

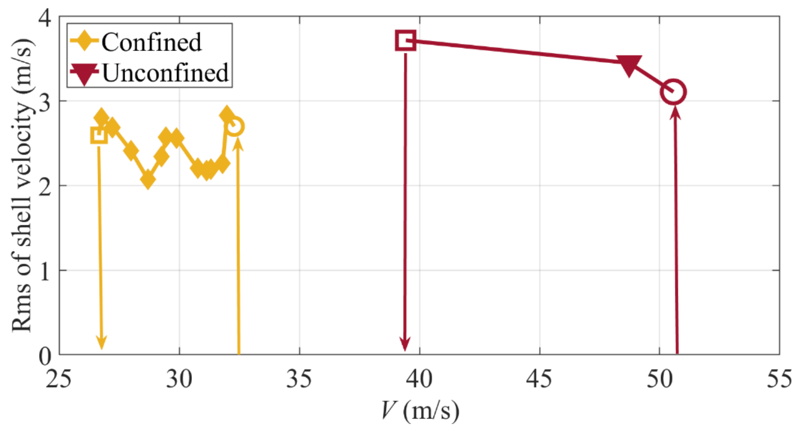

Figure 3-21. Bifurcation diagram of the rms velocity of shell 3 (L/R=4.5, h/R=0.05), with (confined) or without (unconfined) the rigid outer tube. Hollow squares and hollow circles indicate the restabilization and critical flow velocities, respectively.

The largest Lyapunov exponent diagram, Figure 3-22, demonstrates that the two configurations have nearly the same λ_1 at V_{cr}, while the unconfined configuration shows a slightly weaker chaotic component at V_{rest}. For both configurations, when the flow velocity is increased from V_{rest} to close to V_{cr}, the chaotic component is strengthened, but then λ_1 drops at V_{cr}, indicating an increase of the regularity of motion.

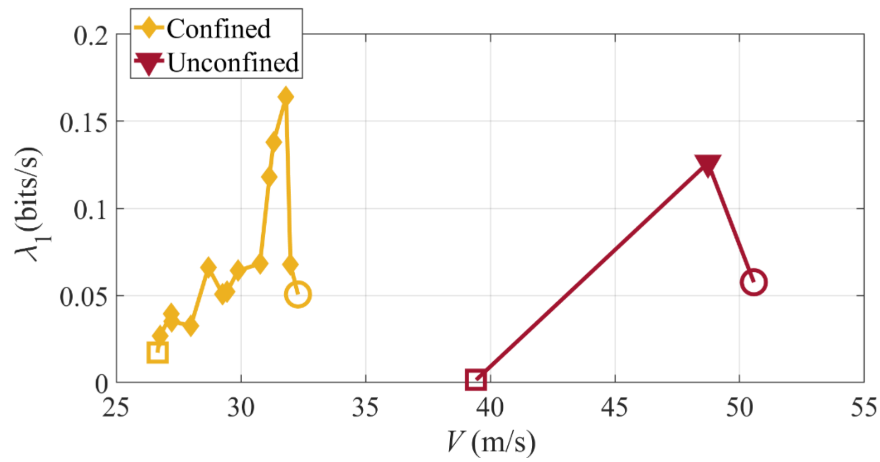

Figure 3-22. The largest Lyapunov exponents, λ_1, versus flow velocity for shell 3 (*L/R*=4.5, *h/R*=0.05), with (confined) or without (unconfined) the rigid outer tube. Hollow squares and hollow circles indicate the restabilization and critical flow velocities, respectively.

According to Table 3-5, both V_{cr} and V_{rest} are higher for the unconfined configuration compared to the confined one. Besides, the unconfined shell exhibits a slightly stronger subcritical behaviour, having a higher value of the nondimensional difference between V_{cr} and V_{rest}.

Table 3-5. The restabilization and critical flow velocities, V_{rest} and V_{cr}, respectively, as well as their nondimensional difference (an indicator of subcritical behaviour), for shell 3 (*L/R*=4.5, *h/R*=0.05), with (confined) or without (unconfined) the rigid outer tube.

Configuration	V_{rest} (m/s)	V_{cr} (m/s)	$(V_{cr} - V_{rest})/V_{cr}$ (%)
Confined	26.6	32.2	17.4
Unconfined	39.4	50.5	22.0

3.9 Conclusions

The present paper presents an in-depth analysis of the dynamic divergence phenomenon for soft shells conveying fluid. Although it was observed for the first time long ago, there have not been sufficient experimental studies yet, because of the fact that dynamic divergence manifests itself as a very violent, relatively high-frequency (of the order of 100 Hz) oscillations, easily capable of destroying the shell. That having been said, soft (low Young's modulus) shells should be utilized to be able to observe dynamic divergence. Thinner and stiffer aluminium shells, are subject to divergence of much smaller amplitude compared to the shell radius; therefore, static divergence is observed because the flow is not constrained enough by the buckled shell for a dynamic divergence to occur.

The experimental results on dynamic divergence by Gholami et al. [30] were for a specific shell with a given *L/R* and *h/R*. However, the question arose on how the dynamical behaviour of shells with different *L/R* and *h/R* ratios would be. This has been addressed in this paper. According to photographs taken with a high-speed camera, at the onset of instability, a divergence with circumferential wave number n=2 or 3 (depending on the L/R ratio) and one longitudinal half-wave (m=1), occurs. This static instability restricts the flow passage considerably such that the throat becomes choked. This results in an increase of pressure upstream of the throat which reopens the shell and triggers a dynamic instability (dynamic divergence). The oscillations evolve in three phases through time. In the first two phases, the oscillations are gentle and shell walls do not impact on each other violently. After about 100-300 ms, depending on the flow velocity and L/R ratio, the oscillations progress to the third phase in which the oscillations are chaotic-looking, with violent impact of shell walls. In this phase, the dynamic divergence occurs through a 'bubble travelling' mechanism; because of the full closure at the throat, a bubble with high-pressure forms at the bottom of the shell which travels upwards and pushes the throat downstream. When the bubble has travelled completely through the shell, the shell buckles in an anti-phase circumferential mode shape and a new bubble forms at the bottom of the shell, et seq.

Bifurcation diagrams of the rms velocity of shells with different L/R and h/R ratios, were obtained with varying flow velocity. The results show that thinner and longer shells undergo instability at lower flow velocities, as expected. Also, thinner shells are subject to higher rms velocities than thicker ones. Increasing L/R ratio (longer shells) enhances the subcritical behaviour for thick shells, while it does opposite for thin shells.

The effect of L/R and h/R ratios on the chaotic component of the oscillations was also examined. It was found that thinner and shorter shells, in comparison with thicker and longer ones, exhibit more irregularity (chaos) in the motion, having higher values of the largest Lyapunov exponent (λ_1), scattered Poincaré maps and pseudo-phase spaces, broad power spectra, etc. The only exception is the L/R=5.5 shell which has lower values of λ_1 than the L/R=6 shell.

Finally, the effect of confinement (the coaxial rigid outer tube) on the onset and post-critical behaviour of the system was explored; the unconfined configuration has been shown to have (i) considerably higher critical and restabilization flow velocities, (ii) higher rms velocity of motion, and (iii) slightly stronger subcritical behaviour.

3.10 References

1. Blevins, R.D.: Flow-Induced Vibrations. Van Nostrand Reinhold, New York (1990).
2. Naudascher, E., Rockwell, D.: Oscillator-model approach to the identification and assessment of flow-induced vibrations in a system. J. Hydraul. Res. 18, 59–82 (1980).
3. Naudascher, E., Rockwell, D.: Flow-Induced Vibrations: An Engineering Guide. AA Balkema, Rotterdam (1994).
4. Dowell, E.H.: Aeroelasticity of Plates and Shells. Noordhoff International Publishing, Leyden (1975).
5. Dowell, E.H.: A Modern Course in Aeroelasticity, Fifth Revised and Enlarged Edition.

Springer, Dordrecht (2015).

6. Païdoussis, M.P.: Fluid-Structure Interactions: Slender Structures and Axial Flow: Vol. 1, Second Edition. Academic Press, Oxford (2014).

7. Païdoussis, M.P.: Fluid-Structure Interactions: Slender Structures and Axial Flow: Vol. 2, Second Edition. Academic Press, Oxford (2016).

8. Païdoussis, M.P., Abdelbaki, A.R., Butt, M.F.J., Tavallaeinejad, M., Moditis, K., Misra, A.K., Nahon, M., Ratigan, J.L.: Dynamics of a cantilevered pipe subjected to internal and reverse external axial flow: A review. J. Fluids Struct. 106, 103349 (2021).

9. Païdoussis, M.P., Denise, J.-P.: Flutter of cylindrical shells conveying fluid. J. Sound Vib. 16, 459–461 (1971).

10. Païdoussis, M.P., Denise, J.-P.: Flutter of thin cylindrical shells conveying fluid. J. Sound Vib. 20, 9–26 (1972).

11. Done, G.T.S., Simpson, A.: Dynamic instability of certain conservative and non-conservative systems. J Mech Eng Sci. 19, 251–263 (1977).

12. Weaver, D.S., Unny, T.E.: On the dynamic stability of fluid-conveying pipes. J. Appl. Mech. 40, 48–52 (1973).

13. Païdoussis, M.P., Chan, S.P., Misra, A.K.: Dynamics and stability of coaxial cylindrical shells containing flowing fluid. J. Sound Vib. 97, 201–235 (1984).

14. El Chebair, A., Païdoussis, M.P., Misra, A.K.: Experimental study of annular-flow-induced instabilities of cylindrical shells. J. Fluids Struct. 3, 349–364 (1989).

15. Karagiozis, K.N., Païdoussis, M.P., Misra, A.K., Grinevich, E.: An experimental study of the nonlinear dynamics of cylindrical shells with clamped ends subjected to axial flow. J. Fluids Struct. 20, 801–816 (2005).

16. Karagiozis, K.N., Amabili, M., Païdoussis, M.P., Misra, A.K.: Nonlinear vibrations of fluid-filled clamped circular cylindrical shells. J. Fluids Struct. 21, 579–595 (2005).

17. Païdoussis, M.P.: Some unresolved issues in fluid-structure interactions. J. Fluids Struct. 20, 871–890 (2005).

18. Amabili, M., Pellicano, F., Païdoussis, M.P.: Non-linear dynamics and stability of circular cylindrical shells containing flowing fluid. Part I: Stability. J. Sound Vib. 225, 655–699 (1999).

19. Amabili, M., Karagiozis, K., Païdoussis, M.P.: Effect of geometric imperfections on non-linear stability of circular cylindrical shells conveying fluid. Int. J. Non. Linear. Mech. 44, 276–289 (2009).

20. Karagiozis, K.N., Païdoussis, M.P., Amabili, M., Misra, A.K.: Nonlinear stability of cylindrical shells subjected to axial flow: Theory and experiments. J. Sound Vib. 309, 637–676 (2008).

21. Karagiozis, K.N., Païdoussis, M.P., Amabili, M.: Effect of geometry on the stability of cylindrical clamped shells subjected to internal fluid flow. Comput. Struct. 85, 645–659 (2007).

22. Balasubramanian, P., Ferrari, G., Amabili, M.: Nonlinear vibrations of a fluid-filled, soft circular shell: experiments and system identification. Nonlinear Dyn. 102, 1409–1418 (2020).

23. Amabili, M., Pellicano, F., Païdoussis, M.P.: Nonlinear stability of circular cylindrical shells in annular and unbounded axial flow. J. Appl. Mech. 68, 827–834 (2001).

24. Amabili, M., Pellicano, F., Païdoussis, M.P.: Non-linear dynamics and stability of circular cylindrical shells containing flowing fluid. Part IV: Large-amplitude vibrations with flow. J. Sound Vib. 237, 641–666 (2000).

25. Amabili, M., Garziera, R.: Vibrations of circular cylindrical shells with nonuniform constraints, elastic bed and added mass. Part II: Shells containing or immersed in axial flow. J. Fluids Struct. 16, 31–51 (2002).

26. Amabili, M., Garziera, R.: Vibrations of circular cylindrical shells with nonuniform constraints, elastic bed and added mass. Part III: Steady viscous effects on shells conveying fluid. J. Fluids Struct. 16, 795–809 (2002).

27. Amabili, M.: Nonlinear Vibrations and Stability of Shells and Plates. Cambridge University Press (2008).

28. Amabili, M., Païdoussis, M.P.: Review of studies on geometrically nonlinear vibrations and dynamics of circular cylindrical shells and panels, with and without fluid-structure interaction. Appl. Mech. Rev. 56, 349–356 (2003).

29. Alijani, F., Amabili, M.: Non-linear vibrations of shells: A literature review from 2003 to 2013. Int. J. Non. Linear. Mech. 58, 233–257 (2014).

30. Gholami, I., Amabili, M., Païdoussis, M.P.: Dynamic divergence of circular cylindrical shells conveying airflow. Mech. Syst. Signal Process. Accepted (September 2021).

31. Mallat, S.: A Wavelet Tour of Signal Processing: The Sparse Way. Academic Press, Burlington (2009).

32. Moon, F.C.: Chaotic and Fractal Dynamics: Introduction for Applied Scientists and Engineers. John Wiley & Sons, New York (2008).

33. Wolf, A., Swift, J.B., Swinney, H.L., Vastano, J.A.: Determining Lyapunov exponents from

a time series. Phys. D Nonlinear Phenom. 16, 285–317 (1985).

34. Moon, F.C.: Chaotic Vibrations. Wiley-Interscience, New York (2004).

35. Malraison, B., Atten, P., Bergé, P., Dubois, M.: Dimension of strange attractors: an experimental determination for the chaotic regime of two convective systems. J. Phys. Lett. 44, 897–902 (1983).

4 Conclusions and suggested future work

4.1 Summary of findings

The present study presents an in-depth analysis of the dynamic divergence phenomenon for soft shells conveying fluid. Although it was observed for the first time long ago, there have not been sufficient experimental studies yet, because of the fact that dynamic divergence manifests itself as a very violent, relatively high-frequency (of the order of 100 Hz) oscillations, easily capable of destroying the shell. That having been said, soft (low Young's modulus) shells should be utilized to be able to observe dynamic divergence. Thinner and stiffer aluminium shells, are subject to divergence of much smaller amplitude compared to the shell radius; therefore, static divergence is observed because the flow is not constrained enough by the buckled shell for a dynamic divergence to occur.

According to photographs taken with a high-speed camera, at the onset of instability, a divergence with circumferential wave number n=2 or 3 (depending on the *L/R* ratio) and one longitudinal half-wave (m=1), occurs. This static instability restricts the flow passage considerably such that the throat becomes choked. This results in an increase of pressure upstream of the throat which reopens the shell and triggers a dynamic instability (dynamic divergence).

The oscillations evolve into more complex and distorted forms in three phases through time. In the first two phases, the oscillations are gentle and shell walls do not impact on each other violently. After about 100-300 ms s (20 to 50 cycles), depending on the flow velocity and *L/R* ratio, the oscillations progress to the third phase in which the oscillations are chaotic-looking, with violent impact of shell walls. In this phase, the dynamic divergence occurs through a 'bubble travelling' mechanism; because of the full closure at the throat, a high-pressure bubble forms at the bottom of the shell, which travels upwards and pushes the throat downstream. When the bubble has travelled completely through the shell, the shell buckles in an anti-phase circumferential mode shape and a new bubble forms at the bottom of the shell, et seq.

Bifurcation diagrams of the rms velocity of shells with different *L/R* and *h/R* ratios, were obtained with varying flow velocity. When the flow velocity was reduced, the amplitude of the oscillation decreased with a very irregular, rather than smooth trend, and eventually ceased at a flow velocity named V_{rest}, considerably lower than that for the onset of the oscillation, V_{cr}, indicating a highly subcritical behaviour. The results show that thinner and longer shells undergo instability at lower flow velocities, as expected. Also, thinner shells are subject to higher rms velocities than thicker ones. Increasing the *L/R* ratio (longer shells) enhances the subcritical behaviour for thick shells, while it does the opposite for thin shells.

Although displaying a dominant frequency, the oscillations also contained a chaotic component, sometimes large and sometimes small. The effect of *L/R* and *h/R* ratios on the chaotic component of the oscillations was also examined. It was found that thinner and shorter shells, in comparison with thicker and longer ones, exhibit more irregularity (chaos) in the motion, having higher values of the largest Lyapunov exponent (λ_1), scattered Poincaré maps and pseudo-phase spaces, broad power spectra, etc. The only exception is the *L/R*=5.5 shell which has lower values of λ_1 than the *L/R*=6 shell. In addition, thin shells show a more pronounced chaotic behaviour at the upper half of the flow velocity range, while thick shells do opposite.

The stability of a shell (*L/R*=6 and *h/R*=0.05) pressurized from outside, as a result of a small open hole (D_h=3 mm) at the bottom clamp, was also investigated. Interestingly, it was observed that oscillations ended in static buckling after about 5 s (~ 400 cycles) of oscillatory motion. The reason is that, in this case, there is an increase of the pressure in the annulus, which forces the shell to stop oscillating and to become subject to buckling by external pressure (combined to internal flow, which reduces the effective shell stiffness).

In the end, the effect of confinement (the coaxial plexiglas outer tube) on the onset and post-critical behaviour of the system was examined; removing this outer rigid tube was shown to (i) increase considerably the critical and restabilization flow velocities, (ii) increase the rms velocity of motion, and (iii) slightly strengthen the subcritical behaviour.

4.2 Future work

Although dynamic divergence was observed for the first time long ago, the work presented in this thesis is believed to be the first research exploring characteristics of the phenomenon such as its mechanism and chaotic behaviour. This research can be expanded in different directions. Most importantly, a refined model capable of predicting the dynamic instability (dynamic divergence) following the initial buckling should be developed; in this regard, utilization of an appropriate outflow model in nonlinear theoretical modelling is essential to predict the correct response of a soft shell clamped at both ends and conveying airflow.

As shown in this study, the airflow can be fully blocked in each cycle of oscillations; hence, it is compressible. Thus, the incompressibility assumption in the theoretical studies of the stability of such soft shells is not valid and new theoretical models should take into account the compressibility of the flow and its effect on the fluid-related forces to predict the correct post-buckling dynamics. This may shed light on the question why the oscillatory response following the initial buckling is not predicted by the existing theoretical models for clamped-clamped shells.

The instabilities discussed in this thesis were induced by disturbing the air in the annulus (disturbance-induced instability), so that the shells became unstable at lower flow velocities compared to those arising spontaneously (self-excited instability); due to the limitations in the supply of compressed air, the onset of self-excited instability could not be reached. It would be of interest to utilize a shell with smaller thickness and/or diameter, in order to (i) reach the self-excited instability, and (ii) see if new instabilities exist at flow velocities well beyond the first instability. In addition, new experiments could be conducted using coaxial shells with simultaneous internal and annular airflow with the same or opposite directions.